SYNTHESIS AND CHARACTERIZATION OF
Ni-Mn-X (X: In, Sb) FSMA THIN FILMS

A THESIS

Submitted in partial fulfilment of the
requirements for the award of the degree
of

DOCTOR OF PHILOSOPHY

in

PHYSICS

by

HARISH SHARMA AKKERA

DEPARTMENT OF PHYSICS
INDIAN INSTITUTE OF TECHNOLOGY ROORKEE
ROORKEE-247667 (INDIA)
AUGUST, 2015

INDIAN INSTITUTE OF TECHNOLOGY ROORKEE
ROORKEE

CANDIDATE'S DECLARATION

I hereby certify that the work which is being presented in the thesis entitled **"SYNTHESIS AND CHARACTERIZATION OF Ni-Mn-X (X: In, Sb) FSMA THIN FILMS"** in partial fulfilment of the requirements for the award of the Degree of Doctor of Philosophy and submitted in the Department of Physics of the Indian Institute of Technology Roorkee, Roorkee is an authentic record of my own work carried out during a period from July, 2011 to August, 2015 under the supervision of Dr. Davinder Kaur, Professor, Department of Physics & Centre of Nanotechnology and Dr. Inderdeep Singh, Associate Professor, Mechanical and Industrial Engineering Department, Indian Institute of Technology Roorkee, Roorkee.

The matter presented in this thesis has not been submitted by me for the award of any other degree of this or any other Institute.

5/3/2016

(Harish Sharma Akkera)

This is to certify that the above statement made by the candidate is correct to the best of our knowledge.

8.3.16

Date: March 8th, 2016   (Davinder Kaur)   (Inderdeep Singh)

Supervisor   Supervisor

The Ph.D. Viva-Voice Examination of **Mr. Harish Sharma Akkera**, Research Scholar, has been held on 08.03.2016   .

Signature of Supervisor   Chairman, SRC   Signature of External Examiner

Head of the Department/Chairman ODC

ABSTRACT

In recent years, Ni-Mn-X (X: In, Sb) based ferromagnetic shape memory alloys (FSMAs) showing a reversible first-order martensitic phase transformation between high symmetry austenitic phase to low symmetry martensitic phase accompanied with a macroscopic shape change, have attracted increasing scientific attention as multifunctional materials due to their large magnetic-field-induced strains (MFIS) by the rearrangement of twin variants in the martensite and as potential candidates for high sensitivity magnetic actuators and sensors. These alloys exhibit various magnetic field-driven properties such as magnetic shape memory effect, martensitic phase transformation, exchange bias effect and magnetocaloric effect etc. So far, numerous groups have studied these magnetic field-driven properties in bulk FSMAs. For emerging micro devices such as magnetically driven microelectromechanical systems (MEMS) and even microscopic machines, high quality FSMA thin films grown on semiconductor substrates are required. It is desirable to establish the process for producing high quality thin films of these materials for their integration into emerging technologies.

The main objective of the present work was to synthesize nanostructured ferromagnetic shape memory alloy thin films of Ni-Mn-X (X: In, Sb) on Si (100) substrate using DC magnetron sputtering technique to investigate the structural, phase transformation, magnetic and mechanical properties of these films. In addition Ni-Mn-Sb/CrN heterostructures were fabricated and the effect of varying thickness of CrN layer on various properties of heterstructure was studied. A chapter - wise summary of the thesis is given below:

Chapter 1 gives an overview of ferromagnetic shape memory alloys and material background. This chapter includes literature survey on physical properties of Ni-Mn-X (X: In, Sb) ferromagnetic shape memory alloys and their thin films. The fourth element addition, exchange bias and magnetocaloric effect properties of FSMAs have been discussed.

Chapter 2 presents the details of experimental techniques, which we have used for the synthesis and characterization of these films. The synthesis of thin films in present thesis has been carried out by DC magnetron sputtering technique. Various sputtering parameters were optimized in order to obtained good quality FSMA films. X-ray diffraction technique has been used for phase identification and crystallite size analysis. The surface morphology and microstructure of thin films were studied using Atomic Force Microscopy (AFM) and Field Emission Scanning Electron Microscopy (FESEM). The film thickness was measured using cross-sectional FESEM. The temperature and field dependent magnetization (M-T and M-H) measurements of thin films were studied using Cryofree Vibrating Sample Magnetometer

(VSM) and SQUID. The electrical properties of these films were measured using four probe resistivity set up in the temperature range from 30 K to 400 K. The nanoindentation was used to study the mechanical properties such as hardness (H), elastic modulus (E), plasticity index (H/E) and resistance to plastic deformation (H^3/E^2) of thin films.

Chapter 3 describes the growth and characterization of nanostructured Ni-Mn-In ferromagnetic shape memory alloy thin films. In this chapter the influence of film thickness on structural, magnetic, electrical and mechanical properties of nanostructured Ni-Mn-In thin films was studied. The film thickness was varied from ~ 90 nm to 655 nm. XRD analyses revealed that the films exhibit austenitic phase with L2$_1$ structure at room temperature. The grain size and crystallization extent increased with corresponding increase in film thickness. The temperature dependent magnetization and electrical measurements demonstrated the absence of phase transformation in the film with lower thickness ~ 90nm which could be due to small grain size of film. For thickness greater than 153 nm, the films show first order martensitic phase transition with thermal hysteresis width, which increases with further increase in film thickness. The field dependent magnetization curves also show the increase in saturation magnetization (S$_M$). The value of refrigeration capacity (RC) which is an important figure of merit has been found to be 155.04 mJ/cm^3. Maximum exchange bias of 0.0096 T and large magnetic entropy change ΔS_M =15.2 mJ/cm^3 K (field 2 T) at martensitic transition was obtained for film thickness of 655 nm which makes them useful for microelectromechanical systems (MEMS) applications. Further, nanoindentation studies revealed the higher values of hardness of 7.2 GPa and elastic modulus of 190 GPa for the film thickness of 153 nm. These findings indicate that the Ni-Mn-In thin film is potential candidate for various multifunctional properties.

Chapter 4 describes the growth and characterization of Ni-Mn-Sb-Al and Ni-Mn-In-Cr FSMA thin films. This chapter has been divided into two sections. The first section (**section 4.1**) describes the effect of aluminium (Al) content on the martensitic transformations and magnetocaloric effect (MCE) in Ni-Mn-Sb ferromagnetic shape memory alloy (FSMA) thin films. An increase in martensitic transformation temperature (T$_M$) with increasing Al content was observed from magnetic (M-T) and electrical (R-T) measurements. From the study of isothermal magnetization (M-H) curves, a large magnetic entropy change (ΔS_M) of 23 mJ/cm^3 K was found in N$_{49.8}$Mn$_{32.97}$Al$_{4.43}$Sb$_{12.8}$. A remarkable enhancement of MCE has been attributed to the significant change in the magnetization of Ni-Mn-Sb films with increasing Al content. Furthermore, a high refrigerant capacity (RC) was observed in Ni-Mn-Sb-Al thin films as compared to pure Ni-Mn-Sb. The substitution of Al for Mn in Ni-Mn-Sb thin films with field

induced MCE are potential candidates for micro length scale magnetic refrigeration applications where low magnetic fields are desirable. **Section 4.2** describes the influence of Cr addition on the structural, magnetic, and mechanical properties as well as magnetocaloric effect for magnetron sputtered Ni-Mn-In ferromagnetic shape memory alloy thin films. X-ray diffraction studies revealed that Ni-Mn-In-Cr thin films possessed purely austenitic cubic $L2_1$ structure at lower content of Cr, whereas higher Cr content, the films exhibited martensitic structure at room temperature. The temperature-dependent magnetization (M-T) and resistance (R-T) results confirmed the monotonous increase in martensitic transformation temperatures (T_M) with the addition of Cr content (0 - 4.5 at %). Further the addition of Cr content significantly enhanced the hardness (28.2±2.4 GPa) and resistance to plastic deformation H^3/E^2 (0.261) in $Ni_{50.4}Mn_{34.96}In_{13.56}Cr_{1.08}$ film as compared with pure Ni-Mn-In film, which could be due to reduction in grain size, and has been explained in terms of the grain boundary strengthening mechanism. Further, from the study of isothermal magnetization (M-H) curves, the magnetocaloric effect (MCE) around the martensitic transformation has been investigated. The magnetic entropy change ΔS_M of 7.0 mJ/cm^3 K was observed in $Ni_{51.1}Mn_{34.9}In_{9.5}Cr_{4.5}$ film at 302 K in an applied field of 2 T. Finally, the refrigerant capacity (RC) was also calculated for all the films in an applied field of 2 T.

Chapter 5 describes the deposition of $Ni_{50}Mn_{36.8}Sb_{13.2}$/CrN heterostructure thin films on Si (100) substrate to improve the exchange bias and mechanical properties of Ni-Mn-Sb ferromagnetic shape memory alloy thin films. The antiferromagnetic CrN thickness was varied from 15 nm-80 nm. The shift in hysteresis loop up to 51 Oe from the origin was observed at 10 K when pure Ni-Mn-Sb film was cooled under a magnetic field of 0.1 T. The observed exchange bias has been attributed to the coexistence of antiferromagnetic (AFM) and ferromagnetic (FM) exchange interactions in the martensitic phase of the film. On the other hand, a significant shifting of hysteresis loop was observed with AFM CrN layer in $Ni_{50}Mn_{36.8}Sb_{13.2}$/CrN heterostructure. The exchange coupled 140 nm $Ni_{50}Mn_{36.8}Sb_{13.2}$/35nm CrN heterostructure exhibited relatively large exchange coupling field of 138 Oe at 10 K compared to other films, which could be due to uncompensated and pinned AFM spins at FM-AFM interface and different AFM domain structure for different thicknesses of CrN layer. Further nanoindentation measurements revealed the higher values of hardness and elastic modulus of about 12.7±1.25 GPa and 179±0.12 GPa in $Ni_{50}Mn_{36.8}Sb_{13.2}$/CrN heterostructures making them promising candidate for various multifunctional MEMS devices.

Chapter 6 presents the summary and conclusion of the entire work presented in the thesis and also proposes the future directions in which these studies can be extended.

ACKNOWLEDGEMENTS

My experience at Roorkee would not be such fun without all the friends I have met here. Thanks to my friends Srujit Kola, Venu, Venkatesh Reddy, Ashok, Uttam Kakade sir, Thilak, Bala Krishna, Venkateswarlu Devuri, Santosh Reddy, Ravinder, Santosh Dubba, Harish VSKV, and Vidu for counting the days with me and making it seem like help was just a phone call away. I enjoyed every single moment spent with them. I would like make a special mention of Nitin Simha Vihari, Gudipadu Venkatesh, and Sunil, who are always the partners in adventurous road trips.

I would also like to remember Rammurthy, Madhukar and Suresh babu for being the friends of both good times and bad times. All of you have been a true source of support and friendship.

Finally, my family is unrivalled in the support and love they have given me over the years, and I truly appreciate having you all. I am ever indebted to my Parents, my sisters and my brothers, who have stood by me throughout my life, offering help, guidance and inspiration without implicit questions or motives. I am truly indebted to you all forever.

At last, I would like thank the Almighty for the good fortune bestowed in me to experience the best of what life could possibly offer. Thank you.

(HARISH SHARMA AKKERA)

List of Publications

A. Papers in Refereed journals

1. Martensitic phase transformation of magnetron sputtered nanostructured Ni-Mn-In ferromagnetic shape memory alloy thin films.
   Harish Sharma Akkera, Inderdeep Singh and Davinder Kaur
   Journal of Alloys and Compounds, 642 (2015) 53–62.

2. Martensitic phase transformations and magnetocaloric effect in Al co-sputtered Ni–Mn–Sb alloy thin films.
   Harish Sharma Akkera, Nitin Choudhary and Davinder Kaur
   Materials Science and Engineering B, 198 (2015) 113–119.

3. Exchange bias effect in NiMnSb/CrN heterostructures deposited by magnetron sputtering.
   Harish Sharma Akkera, Rahul Barman, Navjot Kaur, Nitin Choudhary, and Davinder Kaur
   *Journal of Applied Physics,*113 (2013) 17D723.

B. Papers under communication:

1. Effect of Cr addition on the structural, magnetic and mechanical properties of magnetron sputtered Ni-Mn-In ferromagnetic shape memory alloy thin films.
   Harish Sharma Akkera and Davinder Kaur
   Surface and Coatings Technology (Communicated)

2. Room temperature magnetocaloric effect in Ni-Mn-In-Cr ferromagnetic shape memory alloy thin films.
   Harish Sharma Akkera and Davinder Kaur
   Vacuum (Under review)

2 Papers presented in national/international conferences:

1. Martensitic phase transformation and magnetocaloric effect in magnetron sputtered $Ni_{50}Mn_{37}Sb_{13}$ heusler alloy thin film.

   Harish Sharma Akkera, Inderdeep Singh and Davinder Kaur

   23rd International Conference on Processing and Fabrication of Advanced Materials (PFAM-XXIII), held at IIT Roorkee, Roorkee, India, during 5-7 December, 2014.

2. Magnetocaloric effect near room temperature in magnetron sputtered Ni-Mn-Sb-Al ferromagnetic shape memory alloys thin films.

   Rahul Barman, **Harish Sharma Akkera** and Davinder Kaur

   National Conference on A cluster of topical meetings on Current Trends in Condensed Matter Physics (CTCMP-2015), held at Nieser Bhubaneswar, Odisha, India, during 19-22 Febrauary, 2015

CONTENTS

Chapter 1

Introduction

CHAPTER 1

INTRODUCTION

1.1 Over view of ferromagnetic shape memory alloys

Ferromagnetic shape memory alloys (FSMAs) are a new class of smart materials that exhibit unique ferromagnetic properties coupled with the shape memory effect. Recently FSMAs have attracted considerable attention due to the fact that the martensitic phase transformation results in a microstructure of twin bands that may be redistributed by the application of an external magnetic field. In a presence of magnetic field, a complete phase transformation from austenitic to martensitic can be induced. The large magnetic field induced strains were found in FSMAs are caused by the microstructural reorientation of martensitic variants. Ferromagnetic shape memory alloys show higher magnetic field induced strains at near room temperature and faster frequency response than any other piezoelectric, magnetostrictive, or conventional shape memory alloys (SMAs) [1]. For micro-electro-mechanical systems (MEMS), such as sensors and actuators, the temperature driven SMAs can produce larger displacements or forces through thermo-elastic martensitic transformation. On the other hand, these SMAs have a very slow response frequency because their actuation is induced by a thermal field. FSMAs display a both ferromagnetic properties and shape memory effect simultaneously in an applied magnetic field [2-3], combining the advantages of both large magnetic field induced strain and short response frequency, and thus they are promising candidates for practical applications. From the application point of view, the magnetic-field-induced martensitic phase transformation is more attractive than the rearrangement of martensitic variants for a magnetically driven actuator because a higher output stress can be expected. In FSMAs, the phase transformation temperatures strongly depend on the stoichiometric composition or structural defects, which are connected with the electronic structure and the unit cell volume. The interaction coupling between the magnetism and structure in FSMA leads to peculiar magneto-mechanical as well as magneto-thermal behavior that render them as important functional materials [4].

1.1.1 Martensitic transformation

The transformation hysteresis is the characteristic future of martensitic transformation (TM). The Temperature dependence of different physical parameters which are magnetization, strain, electrical resistance etc., has been shown in **figure 1.1**.
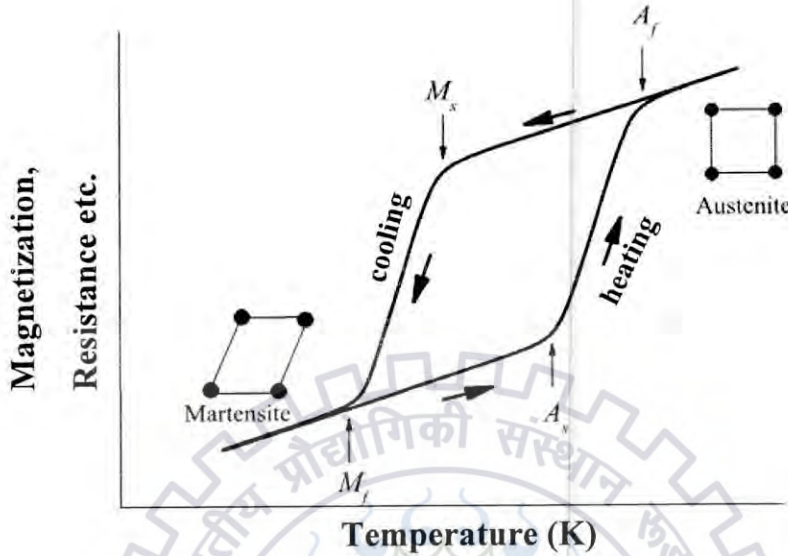
Figure 1.1. Temperature-dependent physical properties (Magnetization, Resistance etc.) graph. The vertical arrows indicates the phase transformation temperatures: austenitic start and finish temperatures, A_s and A_f, martensitic start and finish temperatures, M_s and M_f.

The martensitic start and finish temperatures, M_s and M_f on cooling and the austenitic start and finish temperatures, A_s and A_f on heating are also shown in **figure 1.1**. The square lattice represents the high symmetric austenite phase and low symmetric martensite as an orthorhombic lattice resulting from the distortion of austenite. The development of martensite growths between M_s and M_f, and in the reverse martensitic transformation, austenite formation growth between A_s and A_f. The hysteresis width is given by the difference between A_f and M_s.

1.1.2 Magnetic shape memory effect

The Shape memory alloys (SMAs) are able to memorize and recover its original shape, after it has been deformed by heating over its transformation temperature. This unique effect of returning to an original geometry after a large inelastic deformation is known as the shape memory effect (SME). These SMAs have an ability to reverse a large stress induced deformation in martensitic phase on heating above their transformation temperature. Some shape memory alloys may exhibit an external change in shape as a response to an externally applied magnetic field. This type of behavior is known as magnetic field induced strain (MFIS) and materials exhibiting this

unique behavior are known as MSMAs. Upon cooling, the parent phase transforms into a lower symmetric martensitic phase, and the low-temperature martensite contains multiple variants, each magnetized along a preferred crystallographic orientation, termed the magnetic easy axis. The magnetization of the variant can be oriented in either the positive or negative easy axis direction. With this notion of preferred magnetization directions, it is apparent that a certain martensite variant will be energetically favored over others upon the application of an external magnetic field. If the direction of magnetization in the martensite variant is parallel to the direction of applied magnetic field, the energy required for motion of the martensite twin interface is very small. On the other hand, if the direction of magnetization in the martensite variant is perpendicular to the direction of applied magnetic field, the energy required for martensite twin interface motion is very large. Therefore, the martensite variant whose direction of magnetization is parallel to the direction of the externally applied magnetic field will be energetically favored and the volume fraction of that variant will increase at the expense of the others. In other words, the application of an external magnetic field initiates the motion of twin interfaces such that martensite twins with favorably oriented easy axis of magnetization grow at the expense of the other martensite twins leading to an external shape change. This concept is known as magnetic field induced reorientation of martensite variants. In order to observe reversible martensite variant reorientation, the simultaneous application of an external magnetic field and stress is required. Likewise, the magnetic field induced reorientation of martensite variants is only possible in materials with a low energy requirement for twin boundary motion and high magnetocrystalline anisotropy energy. A schematic representing the process of martensite variant reorientation by magnetic field is shown in **figure 1.2.** In a presence of magnetic field, an individual variant is created, and the length of the material increases from l to L. If the field direction is reversed, the material recovers its original shape with the twinned structure. In a magnetic anisotropic alloys the magnetic moment with the lattice cell is aligned along certain crystallographic axes. Thus especially in the low symmetry martensitic phase the different variants have a magnetic moment that is oriented a specific-axes in the lattice. Without an external magnetic field, the different variants are oriented to the crystal lattice. If an external magnetic field is applied, the martensitic variants and thus the crystal lattice start to align along the field direction. This gives rise to a magnetic field induced strain (MFIS) effect as depicted in **figure 1.3.** The main prerequisite for this effect is a sufficient magnetocrystalline anisotropy that couples the magnetic moment to a specific-axis of the crystal lattice. The magnetocrystalline anisotropy generates a direction dependent magnetization

(5)

behaviour of the crystal lattice where the material can be magnetized easily in certain crystallographic directions (easy axis) while other directions are hard to magnetize (hard axis). If the maximum magnetic field induced stress σ_{mag} applied to the martensitic variant in higher than the stress σ_{tw} (twin boundary movement) required for moving the twin boundary between two adjacent variants, a reorientation of the variants appears. This is expressed by [5],

$$\sigma_{mag} = K_U/\varepsilon_0 \geq \sigma_{tw}$$

This gives rise to a full reorientation of all martensitic variants having their easy c- axis aligned to the external magnetic field [6]. If the c-axis is the short axis in the tetragonal crystal this effect decreases the outer dimensions of a sample giving rise to the actuation effect. In order to achieve this MFIS easy movable twin boundaries are one prerequisite for FSMAs. Materials exhibiting the MFIS have to combine a sufficiently high magnetocrystalline anisotropy K_U with easily movable twin boundaries.

Austenite

High temperature phase

cooling

heating

Low temperature phase

Martensite twinned structure

Martensite detwinned structure

Magnetic field

l

$L>l$
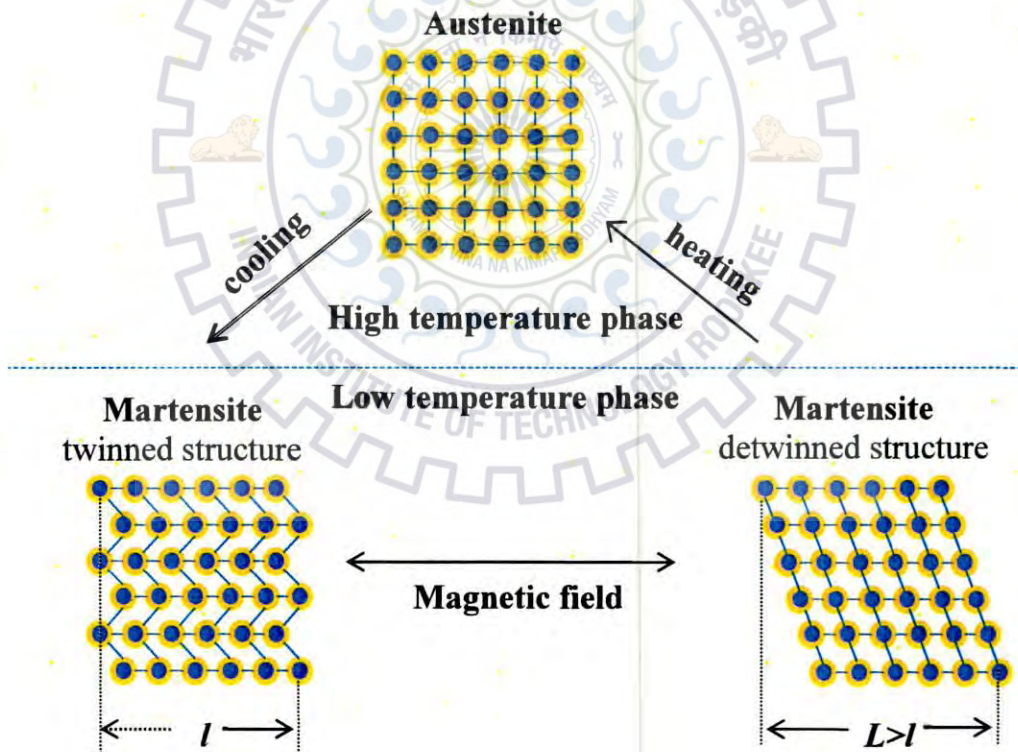
Figure 1.2. Schematic diagram demonstrates the magnetic shape-memory effect.

(6)
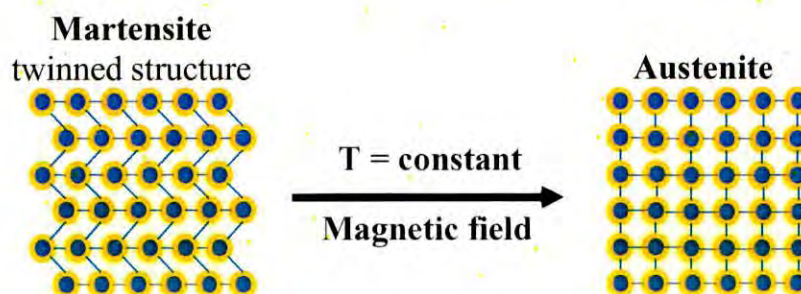
Figure 1.3. Schematic diagram representation of magnetic-field-induced reverse martensitic transformation.

1.2 Ni-Mn based ferromagnetic shape memory alloys

The considerable interest is growing for developing the Ga-free FSMAs, in a technological point of view, from the high cost of pure Ga, and its low melting point, which can create the difficulties during elaboration of the alloys. Sutou *et al*. **[7]** investigated the performance of Ni–Mn–X (X: In, Sn, Sb) alloys as potential candidates for ferromagnetic shape memory effect. The phase diagram of $Ni_{50}Mn_{50-y}X_y$ (X = In, Sb) alloys is represented in **figure 1.4**. Numerous authors have investigated the physical properties of Ni-Mn-X (X: In, Sb) FSMA system. For example, the alloys $Ni_{50}Mn_{50-y}In_y$ (y = 5-25) have been investigated in detail by Krenke *et al*. **[8]**. It has been found that the crystal structure of austenitic phase is cubic while the structure of martensitic phase depends on e/a of the alloy. Oikawa *et al*. **[9]** investigated the magnetic and martensitic transformation behaviors in $Ni_{46}Mn_{41}In_{13}$ alloy and it was found that a unique magnetic-field induced "reverse" transformation in a high magnetic field. Chatterjee *et al*. **[10]** investigated the magnetic properties in $Ni_{2+x}Mn_{1-x}In$ alloys with experimentally and theoretically. Sharma *et al*. **[11]** reported a study of temperature and magnetic field induced strain across the martensitic and austenitic phase transformation in $Ni_{50}Mn_{34}In_{16}$ alloy. Tan *et al*. **[12]** revealed the magnetic properties and martensitic transformation of $Ni_2Mn_{1+x}In_{1-x}$ shape memory alloy by first-principles calculations. In their study, the uncommon magnetic properties occurring upon martensitic transformation are originated from the change of Mn-Mn interatomic distances. Manosa *et al*. **[13]** reported the effect of pressure on the martensitic transformation in magnetically superelastic Ni–Mn–In alloys. It is observed that the martensitic transformation temperatures are significantly affected by the pressure. With increasing pressure all the transformation temperatures are shifted to higher values in $Ni_{50}Mn_{34}In_{16}$ as a consequence of its small entropy change at the transformation. Pathak *et al*. **[14]** first time reported the exchange bias (EB) effect in the bulk

$Ni_{50}Mn_{50-x}In_x$ alloys in the range $14.5 \leq x \leq 15.2$. It is found that the magnetic hysteresis loops were shifted up to 120 Oe at 5 K in all the samples.
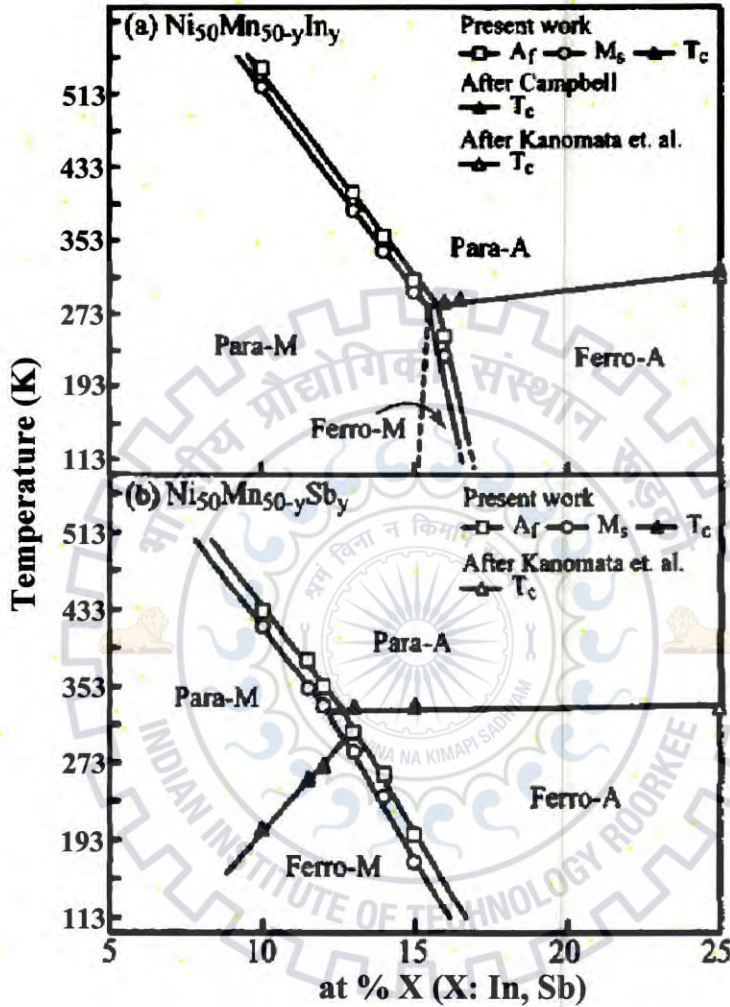
Figure 1.4. The phase diagram of the (a) $Ni_{50}Mn_{50-y}In_y$, (b) $Ni_{50}Mn_{50-y}Sb_y$ alloys [7], and A and M indicate the austenitic and martensitic phases respectively.

Wang *et al.* [15] observed the exchange bias in the martensitic state of bulk polycrystalline $Ni_{49.5}Mn_{34.5}In_{16}$ alloy. Both the exchange bias field (H_{EB}) and coercive field H_C are strongly dependent on temperature. The origin of the exchange bias is attributed to coupling of ferromagnetic and antiferromagnetic at the interfaces and also the training effect is very small in this system, which is of special interest for the applications. The mechanism of the training effect in the present alloy is attributed to the depinning of uncompensated antiferromagnetic spins. Pathak

et al. [16] studied the magnetocaloric properties accompanying with first order martensitic transformation and second order magnetic transformation at the Curie temperature for polycrystalline $Ni_{50}Mn_{50-x}In_x$ 15≤x≤16 alloys. Here, the magnetic entropy change (ΔS_M) and refrigerant capacity (RC) were found to depend on the In concentration and reach a maximum value of $\Delta S_M = -6.8$ J/kg K with a RC = 280 J/kg at 318 K for a magnetic field change of 5 T. Umetsu *et al.* [17] reported that the magnetic change that occurs in $Ni_{50}Mn_{34}In_{16}$ metamagnetic shape memory alloy can be due to the martensitic transformation induced by high magnetic fields up to 18 T. Kinetic arrest of the martensitic transformation was also observed and the martensitic transformation no longer proceeded at temperatures below 100 K. The transformation entropy change between the martensitic phase and austenitic phase calculated from the magnetization curves showed an unusual behavior, changing from positive to negative at about 80 K. Han *et al.* [18] evaluated the giant magnetocaloric effect accompanied with the martensitic transformation in the $Ni_{45.4}Mn_{41.5}In_{13.1}$ alloy. A large positive magnetic entropy change of 8 J/kg K was observed around the T_M in an applied magnetic field of 10 kOe. This magnetic entropy change comes from the first order structural transformation between a low temperature martensitic phases to high temperature austenitic phase. Bhobe *et al.* [19] have investigated the influence of magnetic field on a nonstoichiometric $Ni_{50}Mn_{35}In_{15}$ alloy that undergoes a magnetic and martensitic transformations at near room temperature and the maximum magnetic entropy change $\Delta S_M = 25$ J/kg K at 5 T field reached at room temperature.

Aksoy *et al.* [20] studied the structural as well as magnetic properties of $Ni_{50}Mn_{50-x}Sb_x$ (5.0 ≤ x ≤ 25.0) alloys. Khan *et al.* [21] investigated the exchange bias (EB) in bulk polycrystalline $Ni_{50}Mn_{25+x}Sb_{25-x}$ Heusler alloy system. The hysteresis loop shift up to 248 Oe was observed in an applied field of 5 T. Khan *et al.* [22] has been systematically investigated the magnetocaloric effect (MCE) in $Ni_{50}Mn_{37+x}Sb_{13-x}$ (x = 0, 0.5, 1) ferromagnetic alloy system and they found a maximum positive magnetic entropy change of $\Delta S_M = 19$ J/kg K at approximately 297 K for a magnetic field change of 5 T. Feng *et al.* [23] reported that the MCE in $Ni_{50-x}Mn_{38+x}Sb_{12}$ occurs due to second-order ferromagnetic to paramagnetic transformation.

1.3 Fourth element addition to N-Mn-X (X: In, Sb) FSMAs

Addition of fourth element is a conventional method to modify and improve the properties of a ferromagnetic shape memory alloy. The effect of a large amount of elements alloyed to Ni–Mn–Ga has been investigated in the recent years [24–27]. In most of the cases, the fourth element

additions have been chosen with the purpose to modify the e/a ratio and the characteristic transformation temperatures accordingly. The influence on the lattice parameters have also been studied, since it is a key factor to govern the magnetic and electronic interactions. Numerous authors investigated the properties of addition of fourth element in Ni-Mn-X (X: In, Sb) FSMAs. In these alloys, the martensitic structure is very closely related to the martensitic transformation temperature (T_M) [28]. It is widely accepted that the valence electron concentration (e/a) and unit cell volume are the two important factors which control the physical properties and martensitic transformation temperatures (T_M) of these FSMAs.

Feng et $al.$ [29] investigated the effect of Cu substitution for Ni on magnetic and magnetocaloric properties in $Ni_{49-x}Cu_xMn_{39}Sb_{12}$ (x = 0, 1, 2) alloys. With increasing Cu content from x = 0 to 2, a decreasing dependence T_M on the valence electrons per atom (e/a) concentration is observed. They found the maximum value of $-\Delta S_M$ in the nominal $Ni_{48}Cu_1Mn_{39}Sb_{12}$ alloy is 9.38 J/kg K at 291 K for a magnetic field change from 0 to 5 T, with the refrigerant capacity of 25.9 J/kg were. Han et $al.$ [30] studied the martensitic transformation temperatures, magnetoresistance and magnetocaloric effect in $Ni_{50-x}Co_xMn_{39}Sb_{11}$ (x = 0–11) FSMAs. The martensitic transformation temperatures and magnetic transformation temperatures are strongly depend on the Co concentration. The large MCE and magnetoresistance at near room temperature have been observed in these alloys. Guan et $al.$ [31] observed the large magnetocaloric effect at low magnetic field in Co doped $Ni_{50-x}Co_xMn_{35}In_{15}$ ribbons. Pramanick et $al.$ [32] reported the magnetic and transport properties of Ga doped $Ni_2Mn_{1.32}In_{0.68-x}Ga_x$ (x = 0, 0.04, 0.08, 0.16, 0.20, and 0.28). These alloys exhibited the ferromagnetic nature below the room temperature and the martensitic transformation temperatures are depending on the Ga concentration. Liu et $al.$ [33] explored the martensitic crystal structure and martensitic transformation in Ga doped $Ni_{50}Mn_{34}In_{16-x}Ga_x$ (x = 0, 2, 4, 6, 8, 10, 12, 14, 16) alloys. The effect of B addition on martensitic phase transformation, exchange bias (EB) and magnetocaloric properties in annealed $Ni_{48}Mn_{39}In_{13-x}B_x$ ribbons was investigated by Zhao et $al.$ [34]. It was found that the martensitic phase transformation, EB and magnetocaloric properties were strongly affected by the B concentration. Ray et $al.$ [35] investigated the effect of Al doping in $Ni_{50}Mn_{37}Al_xSb_{13-x}$ (x = 0, 1, 3 and 5) alloys. The substitution of Al for Sb increases the T_M and T_C^A. The increase of T_M is observed due to development of hybridization between 3d states of Ni and Mn atoms. Further, they found a higher exchange bias field (H_{EB}) of 470 Oe for x = 0 and it can decrease with the Al content. The magnetic entropy change (ΔS_M) of 10 J/kg-K is observed for x = 1 alloy under a field change (ΔH) of 50 kOe and it

was reduced by further doping of Al. Takeuchi *et al.* [36] investigated the enhancement of magnetocaloric properties in Ga doped $Ni_{50}Mn_{34.5}In_{15.5}$ alloy. Here, Ga-doping does not affect the austenitic phase transformation but shifts the martensitic phase transformation towards room temperature, producing an enhancement of the magnetic entropy change (ΔS_M) in that temperature region. Large ΔS_M values in the Ga-doped samples are attained for an applied field of 30 kOe as opposed to the field of 50 kOe commonly found for the un-doped cases. Pathak *et al.* [37] explored the magnetic properties in Si doped polycrystalline $Ni_{50}Mn_{35}In_{15-x}Si_x$ magnetic shape memory alloys. An induced strain of more than 0.4% was found for x = 0 at a field of H = 5 T that was observed to be related with a field induced reverse martensitic transformation. In addition, with an increase of Si content, the strains were increased up to 1 % for x = 2 at H = 5 T. Both the positive and negative strain variations were found in the vicinity of martensitic transformation temperatures. The structural, magnetic and mechanical properties of Fe doped $Ni_{50}Mn_{34}In_{16-y}Fe_y$ (y = 0, 2, 3, 4, 5, 8) alloys have been studied by Feng *et al.* [38]. It is found that the martensitic phase transformation temperatures are increased with an increase of Fe concentration. The compressive strength and maximum compressive strain reach up to 1200 MPa and 15.8% for amounts higher than 8 at.% Fe. Khan *et al.* [39] reported the enhancement of ferromagnetism in Cr doped $Ni_{50}Mn_{37-x}Cr_xSb_{13}$ alloys. They found that the martensitic transformation temperature shifted towards lower temperature with increasing of Cr content, while saturation magnetization increases at 5 K. Sanchez-Alarcos *et al.* [40] studied the structural and magnetic properties in Cr substitution for Mn in Ni–Mn–In alloys. It is observed that the Cr-rich second phase is exhibited for very low Cr content. Further, the martensitic transformation temperature can be varied with the change in e/a concentration of the matrix phase.

1.4 Ni-Mn-X (X: In, Sb) FSMA thin films

Magnetically activated shape memory materials have a great potential for applications such as in linear actuators, sensors, magnetic cooling systems and valves. As per above discussion, numerous authors have investigated the bulk FSMAs. However, for micro and nano-system applications, free-standing films and submicron films attached to the substrates are of particular interest. For emerging microdevices such as magnetically driven Micro Electro Mechanical Systems (MEMS), high quality of FSMA thin films grown on semiconductor substrates are required. Currently, thin film technology is being developed intensively.

1.4.1 Ni-Mn-Sb thin films

Thin films of the ferromagnetic shape memory alloys are of particular interest for magnetic devices. Few attempts have been made to deposit the high quality of Ni-Mn-Sb FSMA thin films. For example, Caballero *et al.* [41] successfully deposited the Ni-Mn-Sb thin films using RF magnetron sputtering. Borca *et al.* [42] deposited the epitaxial Ni-Mn-Sb thin films on MgO (100) substrate using a DC facing target sputtering system. Roy *et al.* [43] have studied the magnetic properties of epitaxial NiMnSb films grown on GaAs (1 1 1) substrate by molecular beam epitaxy. Turban *et al.* [44] investigated the magnetic properties of NiMnSb/MgO/NiMnSb heterostructures grown by MBE for preparation of magnetic tunnel junctions (MTJs) with half-metallic electrodes. Giapintzakis *et al.* [45] have grown NiMnSb thin films on Si and InAs substrates using pulse laser deposition at moderate temperatures.

1.4.2 Ni-Mn-In thin films

Recently, Sokolov *et al.* [46] reported the growth and characterization of $Ni_{50}Mn_{35}In_{15}$ thin films grown on $SrTiO_3$ (STO) and MgO single crystal substrates using laser assisted molecular epitaxy method. Grunin *et al.* [47] investigated the magnetic and structural properties of Ni-Mn-In thin films grown on Si (100) substrate using pulse laser deposition. Niemann *et al.* [48] studied the suitable growth conditions to obtain an epitaxial Ni-Mn-In-Co alloy thin films with a metamagnetic transformation in vicinity of room temperature.

In the present thesis we have fabricated the Ni-Mn-In and Ni-Mn-Sb alloy thin films on Si (100) substrate using dc magnetron sputtering technique and systematically explored the structural, magnetic, electrical, mechanical, exchange bias and magnetocaloric properties of these films.

1.5 Exchange bias effect

In Exchange bias (EB) phenomenon, the hysteresis loop is shifted along the magnetic field axis, it consists of two magnetic materials with different magnetic order. The most common EB system is a multilayer consisting of a ferromagnet (FM) in contact with an antiferromagnet (AFM). The term EB is established because the hysteresis loop is shifted with a bias field, in addition to the applied field, which is created from the exchange interaction between the two different materials [49-50].
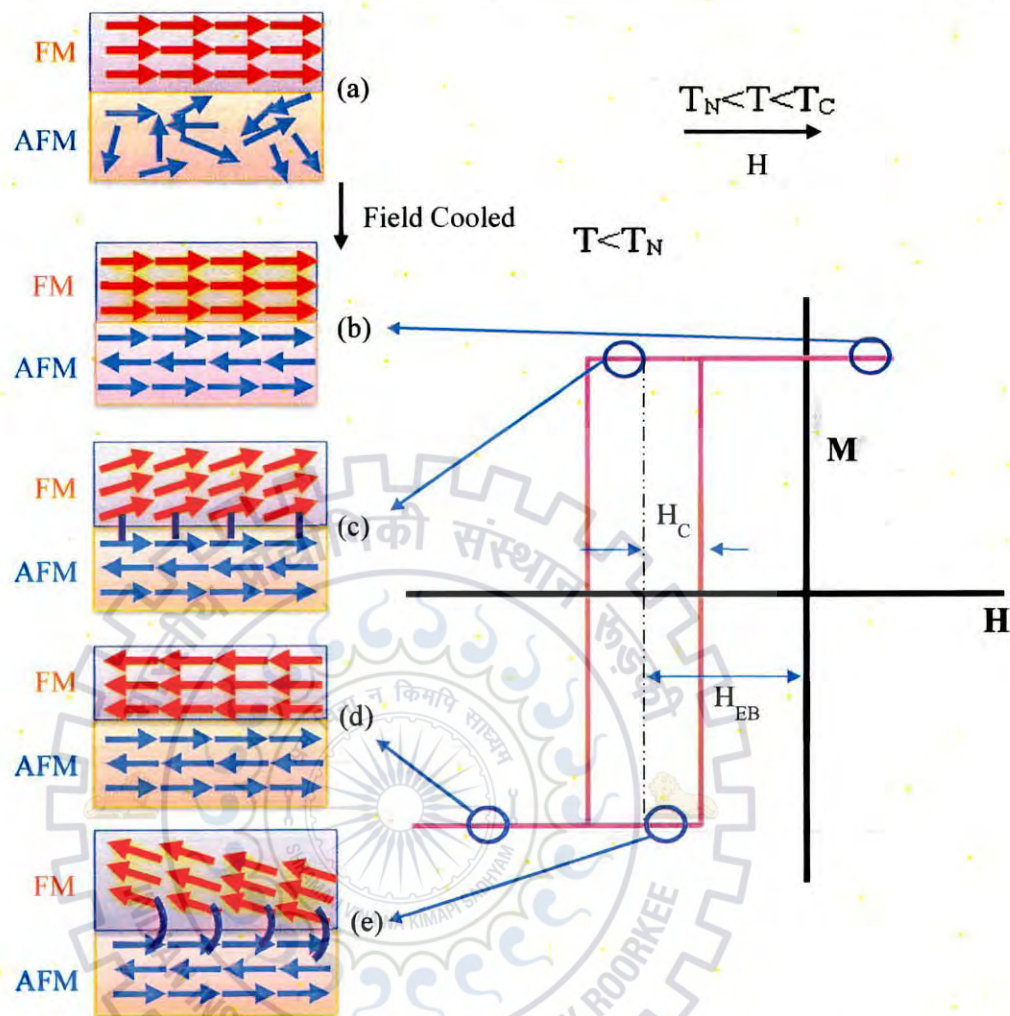
Figure 1.5. Schematic diagram represents the phenomenological model of EB.

Figure. 1.5 describes phenomenologically the appearance of EB in the ferromagnetic (FM)/ antiferromagnetic (AFM) bilayer system **[51]**. It is supposed that the critical temperatures of the FM and of the AFM must be fulfil the condition: $T_C > T_N$, where T_C is the Curie temperature of the FM layer and T_N is the Néel temperature of the AFM layer. At a particular temperature T ($T_N < T < T_C$), the direction of magnetic moments in the AFM layer is random, while the ones of the FM layer are along the external field direction (**Figure 1.5 (a)**). As the sample is cooling down below T_N in the presence of a magnetic field, the moments in the AFM layer become ordered, and the spins near the interface to the FM layer will align in the positive direction, as the FM layer, due to the exchange interaction at the interface between the FM and the AFM the first monolayer of the

(13)

AFM will align parallel (or antiparallel) to the FM spins. The other spins in the AFM layer will follow the AFM order as shown in **figure 1. 5 (b)**. When the magnetic field is reversed, the spins in the FM layer start to rotate, while the AFM spins remain unchanged due to the larger anisotropy. In this case, the interaction between the AFM and FM moments at the interface energetically favors one of the two directions of the FM layer magnetization. This leads to a larger field to reverse the FM layer in the direction against the interfacial AFM spins (**Figure 1.5 (c)**). When the external field changes back, the FM spins can be switched by a smaller field with the help of the interaction from the AFM layer (**Figure 1.5 (e)**). After a complete measurement, the loop is shifted to the negative field direction. This shift of hysteresis loop from the center is known as exchange bias field H_{EB}, and it is negative with respect to the orientation of the FM spins after field cooling (negative exchange bias). Additionally, an enhanced coercivity (H_C) of the hysteresis loop of the FM/AFM bilayer above that of the isolated FM is also observed in experiments, which is however not explained by this simple phenomenological model. There are various reports on exchange bias effect in bulk FSMAs [52-53] but there is no report on exchange bias behavior of FM/AFM bilayer thin films based ferromagnetic shape memory alloys which are required since most of the device applications based on exchange bias are in thin film form. Therefore, in the present thesis we have reported the observed exchange bias effect in Ni-Mn-In and Ni-Mn-Sb/CrN heterostructure FSMA thin films.

1.6 Magnetocaloric effect

Magnetic refrigeration is a relatively novel technique which employs magnetically ordered materials and is based on the magnetocaloric effect (MCE) phenomenon. This phenomenon is described as the thermal response (heating or cooling) of a magnetic substance when a magnetic field is applied or removed. In 1881, Warburg first discovered the MCE in pure iron [54]. In his study, he explored that the iron get suddenly heated up in presence of magnetic field, and on removal of the magnetic field, the iron sample cooled down. The important constituent of any magnetic refrigeration devices is the magnetocaloric material that undergoes a temperature change when subjected to a magnetic field. It is worth noting that all magnetic materials exhibit the MCE. In order to know the physics guiding the MCE, it is important to gain an insight into the behavior of magnetic materials under the influence of a magnetic field. In a magnetic materials, the magnetic moments can order in a variety of ways as shown in **figure 1.6**. The easiest order of magnetic

moments is known as ferromagnetic order, in which the interactions between the moments act to align them.

(a)   **(b)**
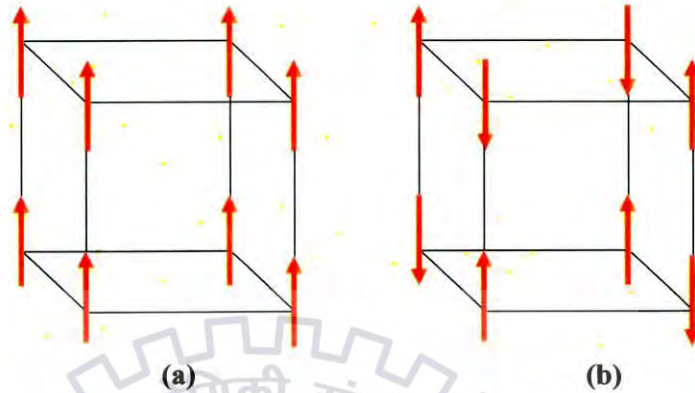
Figure 1.6. Arrows represents the magnetic moments of atoms in a cubic lattice. (a) ferromagnetic order where all the spins align in the same direction. (b) antiferromagnetic order where the spins align opposite to each other.

When a magnetic material placed in a magnetic field, the unpaired spins are aligned parallel to the direction of the magnetic field as shown in **figure 1.7**. The entropy of the system decreases with this spin ordering, subsequently disorder decreases. To compensate for the aligned spins, the atoms of the crystal start to vibrate in making an effort to randomize the spins and reduce the system entropy as a result the material's temperature increases. In this process, to remove of magnetic field an opposite effect occurs. In the low temperatures or extremely larger fields, all of the magnetic moments can be aligned parallel to the magnetic field and a rise in field will not yield any further increase in the magnetization. The disordered state of the magnetic materials are consider to be paramagnetic. In the disordered state, the magnetic materials are considered to be paramagnetic. The magnetization (M) of the material greatly changes at the transformation temperature, whereas the other temperature changes are smaller. The MCE is quantified through a definition of the entropy at constant pressure in a system as a function of temperature and magnetic field, $S(T, H)$. The entropy of a magnetic material consists of the magnetic entropy S_M, the lattice entropy, S_L and the electronic entropy, S_E as given by **equation (1.2)**:

$$S(T, H) = S_M(T, H) + S_L(L) + S_E(T) \dots\dots\dots\dots\dots\dots(1.2)$$

where S_M is a function of both H and T, whereas S_L and S_E are both functions of T only. Thus, only the magnetic entropy, S_M, can be controlled by changing the strength of magnetic field.

(15)
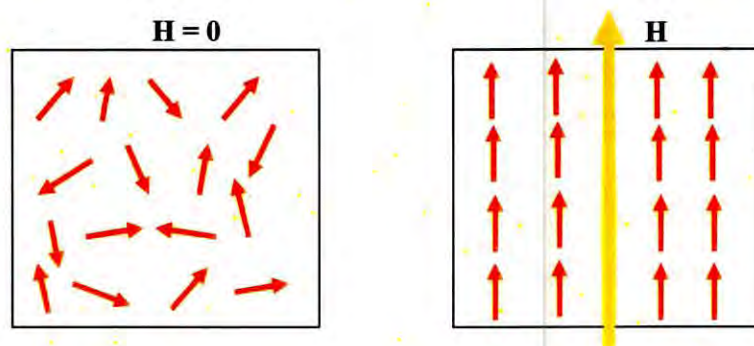
Figure 1.7. Effect of applied magnetic field (H) on the sample.

There are a number of promising classes of materials with large MCEs and tunable Curie temperatures. All of them show great potential for room-temperature applications [55]. The properties that define a good performance of a magnetocaloric material may vary with the refrigeration system and desired temperature interval. The two parameters that provide a good basis for comparison are the adiabatic temperature change and the isothermal magnetic entropy change which has been explained above. A general classification of magnetocaloric materials divide them into two types according to the nature of the magnetic phase transformation used to exploit the MCE. Since the MCE is highest around magnetic phase transformations, the behavior of the materials around these transformations are crucial to the performance of the refrigerant. They can be divided into first order magnetic transformation (FOMT) materials and second order magnetic transformation (SOMT) materials. This division into two classes is convenient since certain characteristics in general follow each class. FOMT materials are currently thought to be the most promising candidates, since they show the highest measured values of the MCE. FOMT materials reach these high values of the MCE, since they have a very abrupt change in magnetization as function of temperature. The derivative of the magnetization is proportional to the magnetic entropy change and the very abrupt phase transformations therefore typically gives a high MCE in a narrow temperature range. On the other hand, SOMT materials in general have broader transformations with lower values of the MCE. Since in technological applications, several other material properties are of importance, the choice between FOMT and SOMT materials is therefore not as straightforward as it might seem. FOMT's have in general slower kinetics than SOMT's, since they are normally connected with structural changes. This leads to different hysteresis phenomena which are unwanted in technological applications. Furthermore most of the known

(16)

FOMT material systems contain either very expensive elements (e.g. Gd), toxic elements (e.g. As) or have very complicated and costly synthesis routes (e.g. La-Fe-Si-H). A variety of SOMT materials with expensive constituents or difficult synthesis routes have also been suggested. Due to several advantages in applications there is a continued interest in the class of mixed-valence manganites crystallizing in the perovskite structure despite the inferior MCE compared to many of the FOMT materials. Manganites are cheap, non-toxic, resistant to corrosion, easy to manufacture, have a decent MCE and have easily tunable transformation temperatures. In the above classification, they lie in between FOMT and SOMT materials depending on the compositions. Compositions from the class of mixed-valence manganites will be further investigated in this thesis. Several extensive reviews on magnetocaloric materials exists [56-59].

There are numerous reports on magnetocaloric effect in bulk FSMAs [29-30, 59-60]. To the best of our knowledge there are no reports on magnetocaloric effect in magnetron sputtered Ni-Mn based ferromagnetic shape memory alloy thin films which are required for most of the micro length scale magnetic refrigeration technology. Therefore, in the present thesis we have reported the observed magnetocaloric effect in Ni-Mn-In-Cr and Ni-Mn-Sb-Al FSMA thin films.

1.7 References

[1] Wuttig M., Liu L. H., Tsuchiya K., James R. D., "Occurrence of ferromagnetic shape memory alloys (invited)", *J. Appl. Phys.*, **87**, 4707 (2000).

[2] Mullner P., Chernenko V. A. and Kostorz G., "Large cyclic magnetic-field-induced deformation in orthorhombic (14M) Ni–Mn–Ga martensite", *J. Appl. Phys.*, **95**, 1531 (2004).

[3] Morito M., Oikawa K., Fujita A., Fukamichi K., Kainuma R., Ishida K., "Enhancement of magnetic-field-induced strain in Ni–Fe–Ga–Co Heusler alloy", *Scripta Mater.*, **53**, 1237 (2005).

[4] Planes A., Manosa L., Saxena A. (Eds.), Magnetism and Structure in functional materials, Materials Science Series, **79**, Springer-Verlag, Berlin, 2005.

[5] Heczko O., "Magnetic shape memory effect and magnetization reversal", *J .Magn. Magn. Mater.*, **290-291**, 787 (2005)

[6] Ullakko K., Huang K., Kokorin V. V., O'Handley R. C, "Magnetically controlled shape memory effect in Ni_2MnGa intermetallic", *Scripta Mater.*,**36**, 1133 (1997).

[7] Sutou Y., Imano Y., Koeda N., Omori T., Kainuma R., Ishida K., Oikawa K., *Appl. Phys. Lett.*, **85**, 4358 (2004).

[8] Krenke T., Acet M., Wassermann E. F., "Ferromagnetism in the austenitic and martensitic states of Ni-Mn-In alloys", *Phys. Rev. B*, **73**, 174413 (2006).

[9] Oikawa K., Ito W., Imano Y., Sutou Y., Kainuma R., Ishida K., Okamoto S., Kitakami O., Kanomata T., "Effect of magnetic field on martensitic transition of $Ni_{46}Mn_{41}In_{13}$ Heusler alloy", *Appl. Phys. Lett.*, **88**, 122507 (2006).

[10] Chatterjee S., Singh V. R., Deb A. K., Giri S.,, De S. K, Dasgupta I., Majumdar S., "Magnetic properties of $Ni_{2+x}Mn_{1-x}In$ Heusler alloys: Theory and experiment", *J. Magn. Magn. Mater.*, **322**, 102 (2010).

[11] Sharma V. K., Chattopadhyay M .K., Chouhan A., Roy S. B., "Temperature and magnetic field induced strain in $Ni_{50}Mn_{34}In_{16}$ alloy", *J. Phys. D: Appl. Phys.*, **42**, 185005 (2009).

[12] Tan C. L., Huang Y. W., Tian X. H., Jiang J. X., Cai W., "Origin of magnetic properties and martensitic transformation of Ni-Mn-In magnetic shape memory alloys", *Appl. Phys. Lett.*, **100**, 132402 (2012).

[13] Mañosa L., Moya X., Planes A., Gutfleisch O., Lyubina J., Barrio M., Tamarit J. L., Aksoy S., Krenke T., Acet M., "Effects of hydrostatic pressure on the magnetism and martensitic transition of Ni–Mn–In magnetic superelastic alloys", *Appl. Phys. Lett.*, **92**, 012515 (2008).

[14] Pathak A. K., Khan M., Gautam B. R., Stadler S., Dubenko I., Ali N., "Exchange bias in bulk Ni–Mn–In-based Heusler alloys", *J. Magn. Magn. Mater.*, **321**, 963 (2009).

[15] Wang B. M., Liu Y., Wang L., Huang S. L., Zhao Y., Yang Y., Zhang H., "Exchange bias and its training effect in the martensitic state of bulk polycrystalline $Ni_{49.5}Mn_{34.5}In_{16}$, *J. Appl. Phys.*, **104**, 043916 (2008).

[16] Pathak A. K., Khan M., Dubenko I., Stadler S., Ali N., "Large magnetic entropy change in $Ni_{50}Mn_{50-x}In_x$ Heusler alloys", *Appl. Phys. Lett.*, **90**, 262504 (2007).

[17] Umetsu R.Y., Ito W., Ito K., Koyama K., Fujita A., Oikawa K., Kanomata T., Kainuma R., Ishida K., "Anomaly in entropy change between parent and martensite phases in the $Ni_{50}Mn_{34}In_{16}$ Heusler alloy", *Scr. Mater.*, **60**, 25 (2009).

[18] Han Z. D., Wang D. H., Zhang C. L., Tang S. L., Gu B. X., Du Y. W., "Large magnetic entropy changes in the $Ni_{45.4}Mn_{41.5}In_{13.1}$ ferromagnetic shape memory alloy", *Appl. Phys. Lett.*, **89**, 182507 (2006).

[19] Bhobe P. A., Priolkar K. R., Nigam A. K., "Room temperature magnetocaloric effect in Ni–Mn–In", *Appl. Phys. Lett.*, **91**, 242503 (2007).

[20] Aksoy S., Acet M., Wassermann E. F., Krenke T., Moya X., Mañosa L., Planes A., "Structural properties and magnetic interactions in martensitic Ni-Mn-Sb alloys", *Phil. Mag.*, **89**, 2093 (2009).

[21] Khan M., Dubenko I., Stadler S., Ali N., "Exchange bias behavior in Ni–Mn–Sb Heusler alloys", *Appl. Phys. Lett.*, **91**, 072510 (2007).

[22] Khan M., Ali N., Stadler S., "Inverse magnetocaloric effect in ferromagnetic $Ni_{50}Mn_{37+x}Sb_{13-x}$ Heusler alloys", *J. Appl. Phys.*, **101**, 053919 (2007).

[23] Feng W. J., Du J., Li B., Hul W. J., Zhang Z. D., Li X. H., Deng Y. F., "Large low-field inverse magnetocaloric effect in $Ni_{50-x}Mn_{38+x}Sb_{12}$ alloys", *J. Phys. D.: Appl. Phys.*, **42**, 125003 (2009).

[24] Cherechukin A. A., Khovailo V. V., Koposiv R. V., Krasnoperov E. P., Takagi T., Tani J., "Training of the Ni–Mn–Fe–Ga ferromagnetic shape-memory alloys due cycling in high magnetic field", *J. Magn. Magn. Mater.*, **258/259**, 523 (2003).

[25] Khovailo V. V., Chernenko V. A., Cherechukin A. A., Takagi T., Abe T., "An efficient control of Curie temperature T_C in Ni–Mn–Ga alloys", *J. Magn. Magn. Mater.*, **272–276**, 2067 (2004).

[26] Glavatskyy I., Glavatska N., Soderberg O., Hannula S. P., Hoff-mann J. U., "Transformation temperatures and magnetoplasticity of Ni–Mn–Ga alloyed with Si, In, Co or Fe", *Scr. Mater.*, **54**, 1891 (2006).

[27] Wang W. H., Ren X., Wu G. H., "Martensitic microstructure and its damping behavior in $Ni_{52}Mn_{16}Fe_8Ga_{24}$ single crystals", *Phys. Rev. B*, **73**, 092101 (2006).

[28] Richard M., Feuchtwanger J., Schlagel D., Lograsso T., Allen S. M., O'Handley R. C., "Crystal structure and transformation behavior of Ni–Mn–Ga martensites", *Scr. Mater.*, **54**, 1797 (2006).

[29] Fenga W. J., Zuo L., Li Y. B., Wang Y. D., Gao M., Fang G. L., "Abnormal e/a dependence of T_M and large inverse magnetocaloric effect in $Ni_{49-x}Cu_xMn_{39}Sb_{12}$ alloys", *Mater. Sci. Eng. B*, **176**, 621 (2011).

[30] Han Z. D., Wang D. H., Zhang C. L., Xuan H. C., Zhang J. R., Gu B. X., Du Y. W., "The phase transitions, magnetocaloric effect, and magnetoresistance in Co doped Ni–Mn–Sb ferromagnetic shape memory alloys", *J. Appl. Phys.*, **104**, 053906 (2008).

[31] Guan W., Liu Q. R., Gao B., Yang S., Wang Y., Xu M. W., Sun Z. B., Song X. P., "Large magnetocaloric effect at low magnetic field in $Ni_{50-x}Co_xMn_{35}In_{15}$ ribbons", *J. Appl. Phys.*, **109**, 07A903 (2011).

[32] Pramanick S., Chatterjee S., Venkateshwarlu D., Ganesan V., De S. K., Giri S., Majumdar S., "Revival of martensitic instability in Ga doped Ni-Mn-In alloys", *Intermetallics*, **42**, 56 (2013).

[33] Liu Z. H., Li G. T., Wu Z. G., Ma X. Q., Liu Y., Wu G. H., "Tailoring martensitic transformation and martensite structure of NiMnIn alloy by Ga doping In", *J. Alloys Compd.*, **535**, 120 (2012).

[34] Zhao X., Li B., Hsieh C. C., Chang W. C., Liu W., Zhang Z., "The Effect of B Doping on the Martensitic Transitions, Magnetocaloric and Magnetic Properties in $Ni_{48}Mn_{39}In_{13-x}B_x$ Ribbons", *IEEE Trans. Magn.*, **48**, 3742 (2012).

[35] Ray M. K., Bagani K., Singh R. K., Majumdar B., Banerjee S., "Effect of Al doping on structural and magnetic properties of $Ni_{50}Mn_{37}Al_xSb_{13-x}$ alloy", *Physica B*, **448**, 33 (2014).

[36]   Takeuchi A. Y., Guimarães C. E., Passamani E. C., Larica C., "Enhancement of magnetocaloric properties near room temperature in Ga-doped $Ni_{50}Mn_{34.5}In_{15.5}$ Heusler-type alloy", *J. Appl. Phys.*, **111**, 103902 (2012).

[37]   Pathaka A. K., Dubenkoa I., Stadler S., Ali N., "Temperature and field induced strain in polycrystalline $Ni_{50}Mn_{35}In_{15-x}Si_x$ magnetic shape memory Heusler alloys", *J. Alloys Compd.*, **509**, 1106 (2011).

[38]   Feng Y., Sui J. H., Gao Z. Y., Zhang J., Cai W., "Investigation on martensitic transformation behavior, microstructures and mechanical properties of Fe-doped Ni–Mn–In alloys", *Mater. Sci. Eng. A*, **507**, 174 (2009).

[39]   Khan M., Dubenko I., Stadler S., Jung J., Stoyko S. S., Mar A., Quetz A., Samanta T., Ali N., Chow K. H., "Enhancement of ferromagnetism by Cr doping in Ni-Mn-Cr-Sb Heusler alloys", *Appl. Phys. Lett.*, **102**, 112402 (2013).

[40]   Sanchez-Alarcos V., Recarte V., Perez-Landazaba J. I., Chapelon J. R., Rodriguez-Velamazan J. A., "Structural and magnetic properties of Cr-doped Ni–Mn–In metamagnetic shape memory alloys", *J. Phys. D.: Appl. Phys.*, **44**, 395001 (2011).

[41]   Caballero J. A., Park Y. D., Cabbibo A., Childress J. R., Petroff F., Morel R., "Deposition of high-quality NiMnSb magnetic thin films at moderate temperatures", *J. Appl. Phys.*, **81**, 2740 (1997).

[42]   Borcal C. N., Ristoiu D., Jeong H. K., Komesu T., Caruso A. N., Pierre J., Ranno L., Nozieres J. P., Dowben P. A., "Epitaxial growth and surface properties of half-metal NiMnSb films", *J. Phys.: Condens. Matter*, **19**, 315211 (2007).

[43]   Roy W. V., Borghs G., De Boeck J., "Epitaxial growth of NiMnSb on GaAs(1 1 1)A and B", *J. Magn. Magn. Mater.*, **242–245**, 489 (2002).

[44]   Turban P., Andrieu S., Snoeck E., Kierren B., Teodorescu C., "NiMnSb/MgO/NiMnSb heterostructures grown by MBE", *J. Magn. Magn. Mater.*, **240**, 427 (2002).

[45]   Giapintzakis J., Grigorescu C., Klini A., Manousaki A., Zorba V., Androulakis J., Viskadourakis Z., Fotakis C., "Pulsed-laser deposition of NiMnSb thin films at moderate temperatures", *Appl. Surf. Sci.*, **197-198**, 421 (2002).

[46]   Sokolov A., Zhang L., Dubenko I., Samanta T., Stadler S., Ali N., "Evidence of martensitic phase transitions in magnetic Ni-Mn-In thin films", *Appl. Phys. Lett.*, **102**, 072407 (2013).

[47]   Grunin A., Goikhman A.Y., Rodionova V., "Ni-Mn-In Heusler Alloy Thin Films Grown by Pulsed Laser Deposition", *Solid State Phenom.*, **190**, 311 (2012).

[48]   Niemann R., Heczko O., Schultz L., Fähler S., "Metamagnetic transitions and magnetocaloric effect in epitaxial Ni–Co–Mn–In films", *Appl. Phys. Lett.*, **97**, 222507 (2010).

[49]   Nogués J., Sort J., Lanlais V., Skumryev V., Surinach S., Munoz J. S., Baró M. D., "Exchange bias in nanostructures", *Phys. Reps.*, **422**, 65 (2005).

[50]   Nogués J., Schuller I. K., "Exchange Bias", *J. Magn. Magn. Mater.*, **192**, 203 (1999).

[51]   Meikeljohn W. H., Bean C. P., "New Magnetic Anisotropy," *Phys. Rev.*, **102**, 1413 (1956).

[52]   Pathak A. K., Khan M., Gautam B. R., Stadler S., Dubenko I., Ali N., "Exchange bias in bulk Ni–Mn–In-based Heusler alloys", *J. Magn. Magn. Mater.*, **321**, 963 (2009).

[53]   Khan M., Dubenko I., Stadler S., Ali N., "Exchange bias behavior in Ni–Mn–Sb Heusler alloys" *Appl. Phys. Lett.*, **91**, 072510 (2007).

[54]   Gschneidner K. A, Pecharsky V. K., Tsokol A. O., "Recent developments in magnetocaloric materials", *Rep. Prog. Phys.*, **68**, 1479 (2005).

[55]   Sandeman K. G., "Magnetocaloric materials: The search for new systems", *Scr. Mater.*, **67**, 566 (2012).

[56]   Lai J. W., Zheng Z. G., Zhong X. C., Franco V., Montemayor R., Liu Z. W., Zeng D. C., "Table-like magnetocaloric effect of $Fe_{88-x}Nd_xCr_8B_4$ composite materials", *J. Magn. Magn. Mater.*, **390**, 87 (2015).

[57]   Szymczak R., Kolano R., Burian A. K., Pietosa J., Szymczak H., "Cooling by adiabatic pressure application in $La_{0.7}Ca_{0.3}MnO_3$ magnetocaloric effect material", *J. Magn. Magn. Mater.*, **322**, 1589 (2010).

[58]   Nicholson D. M., Odbadrakh K., Shassere B. A., Rios O., Hodges J., Ludtka G. M., Porter W. D., Sefat A. S., Rusanu A., Brown G., Evans B. M., "Modeling and characterization of the magnetocaloric effect in Ni_2MnGa materials", *Int. J. Refrig.*, **37**, 289 (2014).

[59]   Nayak A. K., Suresh K. G., Nigam A. K., "Giant inverse magnetocaloric effect near room temperature in Co substituted NiMnSb Heusler alloys", *J. Phys. D.: Appl. Phys.*, **42**, 035009 (2009).

[60]   Yu S. Y., Wei J. J., Kang S.S., Chen J. L., Wu G. H., "Large temperature and magnetic field induced strain in polycrystalline $Ni_{50}Mn_{36}In_{14-x}Sb_x$ alloys", *J. Alloys Compd.*, **586**, 328 (2014).

Chapter 2

Synthesis and Characterization Techniques
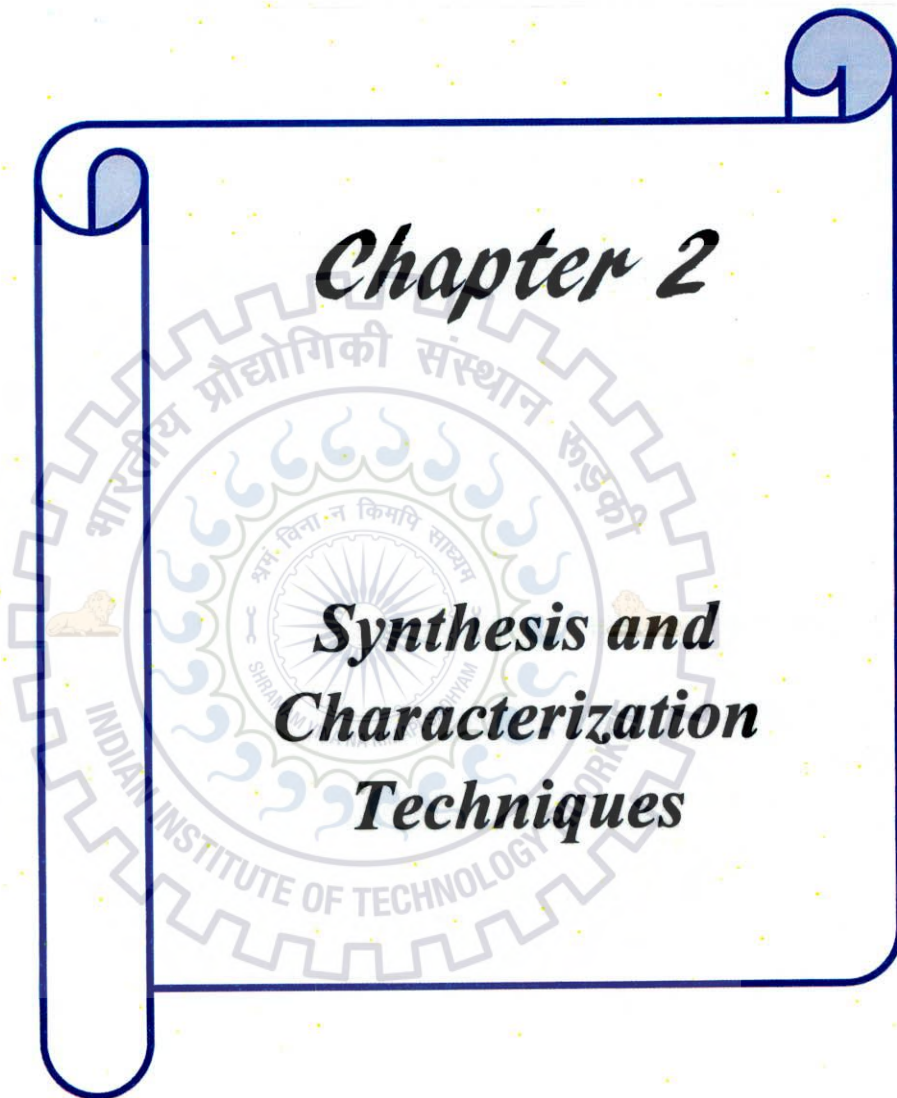
CHAPTER 2

SYNTHESIS AND CHARACTERIZATION TECHNIQUES

2.1   **Synthesis of thin films**

2.2   **DC magnetron sputtering**

2.3   **Characterization techniques**

      2.3.1   X-ray diffraction (XRD)

      2.3.2   Specimen beam interactions

      2.3.3   Field Emission Scanning Electron Microscopy (FE-SEM)

      2.3.4   Atomic Force Microscopy (AFM)

      2.3.5   Electrical transport measurement

      2.3.6   Vibrating Sample Magnetometer (VSM)

      2.3.7   Superconducting Quantum Interference Device (SQUID)

      2.3.8   Nanoindentation

2.4   **References**

2.1 Synthesis of thin films

Thin film formation is a process starting with nucleation followed by coalescence and subsequent thickness growth, all stages of which can be influenced by deposition parameters. The properties of a thin film of a given material depend on the films real structure, which can be defined as the link between thin films deposition parameters and its properties. During thin film growth generally three different types of growth modes can be thermodynamically distinguished by considering the various energy contributions to the total Gibbs energy of the thin film/substrate system, i.e. the surface energies of the film, γ_f, and the bare substrate, γ_s, as well as the interface energy, γ_i, of the interface between the substrate and the film.

Islands: If $\gamma_s < \gamma_f + \gamma_i$, Volmer-Weber type of growth occurs, as characterized by the nucleation of individual islands on the substrate, which grow laterally until they impinge and coalesce.

Volmer-Weber: (island growth)

Layer by layer: If $\gamma_s \geq \gamma_f + \gamma_i$, Frank-Van der Merwe type of growth occurs, as characterized by a maintained, two dimensional progression of the film surface during thickening of the film.
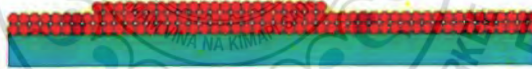
Frank- Van der Merwe: (layer growth; ideal epitaxy)

Layer plus islands: If $\gamma_f + \gamma_i < \gamma_s < \gamma_f + \gamma_i + \gamma_{elastic}$, Stranski-Krastanov type of growth occurs, i.e. initial layer by layer growth proceeds until the elastic deformation energy, $\gamma_{elastic}$, arising from the lattice mismatch accommodation exceeds at a certain thickness a critical value and subsequent island growth becomes favored instead [4].

Stranski-Krastanov: (layer+islands)
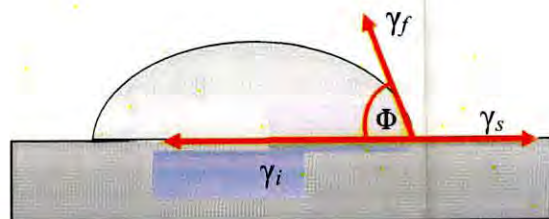
Figure 2.1. Schematic diagram of surface energy of substrate (γ_s),
thin film material (γ_f) and interface energy of film-substrate (γ_i).

Young's equation **(equation 2.1)** represents the growth modes can classified in terms of surface energies:

$$\gamma_s = \gamma_i + \gamma_f \cos\Phi \dots\dots\dots\dots\dots\dots\dots\dots\dots\dots(2.1)$$

where Φ is the wetting angle of a liquid nucleus on a substrate, γ_s is the surface energy of substrate, γ_f is the surface energy of thin film material, and γ_i is the interface energy between film and substrate.

Various chemical vapor deposition (CVD) and physical vapor deposition (PVD) techniques have been used to fabricate thin films such as spray pyrolysis, metal-organic chemical vapour deposition (MOCVD), evaporation by resistive heating, electron beam evaporation, magnetron sputtering, pulse laser deposition (PLD), laser molecular beam epitaxy (LMBE) with each technique having its own specific advantages and disadvantages. The choice of a particular technique usually depends on the specific characteristics of material of thin film and application of interest. Although, wet-chemical techniques are very useful for the synthesis of highly mono-dispersed, surface passivated nanopowder in large quantities, however the production of densely packed, uniform, nanocrystalline thin films required for device applications are not possible with these methods. The usual techniques of spin coating and dip coating lead to films that lack uniform density and thickness.

If the primary requirement is to get highly uniform nanocrystalline thin films with a moderate size distribution, then physical vapor deposition (PVD) techniques such as evaporation, sputtering and laser ablation are found to be very effective. As in these processes, synthesis is usually carried out from the same material whose film is to be synthesized; so its purity is decided by the purity of starting material. For the case of deposition by evaporation, disadvantage is that it is difficult to keep constant rate of evaporation for all the materials. The disadvantage with PLD is

(26)

that although we get stoichiometric composition of target onto the film, but we do not get large area uniformity. Among various PVD techniques, sputtering process exhibits several advantages; any material can be sputtered in form of atoms and/or molecules and film deposition rates can be made uniform over large areas.

The advantages of sputtering as deposition technique are as following:

- The deposited films have high uniformity at large area.
- Better reproducibility of deposited films.
- Good adhesion of film with substrate.
- High flexibility of large-scale as well as production of complex geometries.
- Easy deposition of materials with high melting points and high reactivity.
- Better film thickness control.
- High deposition rate.

Here, we describe briefly about the sputtering process and about the setup used for the synthesis of thin films and heterostructures.

2.2 DC Magnetron Sputtering

Magnetron sputtering is a thin film deposition technique based on the physical sputtering effects caused by the bombardment of a target material with accelerated ions produced in a glow discharge plasma. A wide variety of thin film materials, from metals to insulators, may be produced using this technique. **Figure 2.2** shows the different particles involved in a magnetron sputtering process **[1]**. A plasma is generated when secondary electrons, produced by the collision of positive ions with the target atoms, collide and ionize the inert gas atoms. The initial positive ions needed to trigger the generation of secondary electrons are thought to be either the stray ions always present in the atmosphere or the ions produced by field ionization of the inert gas atoms. Due to radial magnetic field, the secondary electrons get confined in an annular region close to the target surface with a boundary corresponding to the location of the magnetic poles (the impressions of which can be seen in a sputter-eroded target), where electric field E and magnetic field B become parallel. This confinement of secondary electrons leads to an increase in the probability of ionizing the inert gas atoms, making the plasma more intense and sustainable at lower pressures. When an inert gas hits a target atom, the latter gains part of the momentum and transfer it to other atoms through further collisions, leading to a cascade which results in

some of the target atoms to 'sputter' out of the target. The sputtered atoms get deposited on all the surfaces, with maximum deposition taking place on the substrate, which is the nearest surface to the target and subtends the maximum area perpendicular to the momentum of ejected target atoms and clusters. In the present work, Ni-Mn-In, Ni-Mn-Sb films were deposited by DC magnetron sputtering in an Ar atmosphere.
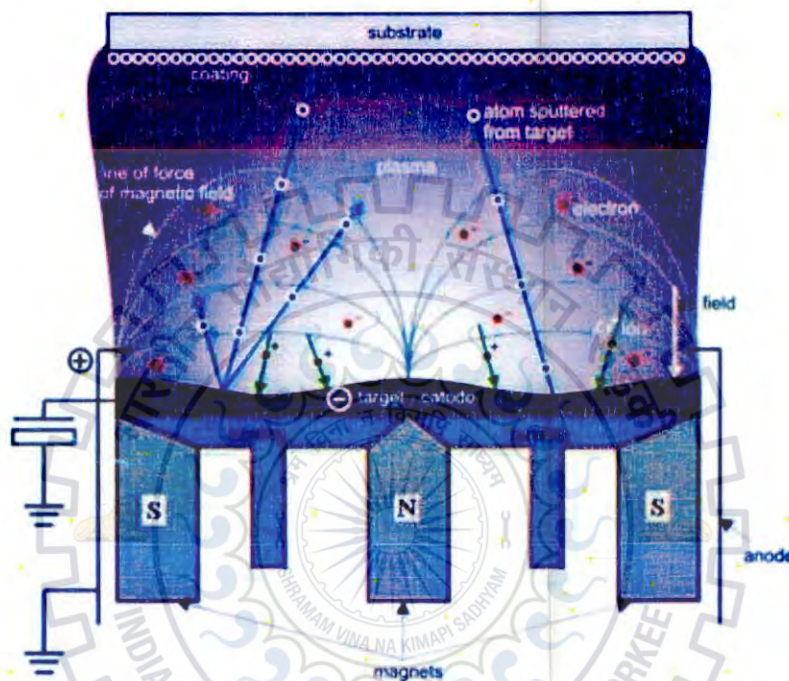
Figure 2.2. Schematic diagram of different particles involved in the magnetron sputtering process [1].

Figure 2.3 shows the actual photograph of the magnetron sputtering system assembled in Functional Nanomaterials Research Laboratory, Department of Physics, IIT Roorkee. The Pfeiffer Vacuum company pumps and gauges are assembled in to the chamber. For DC magnetron sputtering, Aplab high voltage DC power supply (50-1000 V, 0-1 A) was used. Circular discs of diameter 50.8 mm and thickness 3-5 mm of Ni-Mn-In and Ni-Mn-Sb were used as target materials, which were mounted on the magnetron gun for sputtering. For the preparation of thin films the substrate silicon (100) was fixed on a heater (Range: Room temperature to1123 K), with the help of clips as well as with the help of silver paste. The substrate temperature was monitored from the temperature controller. The chamber was evacuated using a rotary and turbo molecular pump up to high vacuum pressure ($\leq 2 \times 10^{-6}$ Torr). After evacuation process, an inert gas Argon (99.9%

(28)

purity) was filled into the chamber through gas inlet valve. Finally, the negative potential is applied to the target and the sputtering process starts.

Figure 2.3. Magnetron sputtering system

2.3 Characterization techniques

2.3.1 X-ray Diffraction (XRD)

X-ray diffraction is a powerful analytical tool to produce unique fingerprint corresponding to Bragg reflections of crystalline materials. Every crystalline sample has its own exclusive XRD pattern where each peak relates to a unique and repeating set of parallel planes that are present and oriented in all the different directions of three-dimensional lattice of crystals. However, in order to map diffraction pattern of a particular set of parallel planes with inter-planar spacing (d), this set must be aligned with respect to the incident monochromatic X-ray beam of wavelength λ, in such manner that Bragg's law is satisfied according to the **equation (2.2)** [2];

$$2d\sin\theta = n\,\lambda \ldots\ldots\ldots\ldots\ldots\ldots\ldots\ldots\ldots(2.2)$$

where n is an integer signifying order of the reflection and θ, also called Bragg's angle, is the angle between the incident ray and reflecting plane. The XRD pattern is sensitive to the relative atomic positions in the crystals and the length scale over which the crystallinity prevails. The number of peaks observed in an XRD pattern is directly linked with unit cell symmetry in such a way that

(29)

higher symmetry crystalline samples normally produce fewer peaks. The position of the peaks (2θ) is a measure of inter planner spacing or d-spacing between planes of atoms in the structure. Finally, the peak intensities tell us about the type of atoms present in the repeating crystal planes. The light atoms having less number of electrons scatter X-rays weakly. On the other hand, heavy atoms having large number of electrons scatter X-rays more effectively. In nutshell, three vital parameters extracted from an XRD pattern regarding the number, positions and intensities of peaks, together define a unique fingerprint or identity of material which is used in following applications [3-5];

- Measurement of purity and crystalline content of materials.
- Identification and quantification of crystalline phases including mixtures of phases present.
- Determination of crystalline to amorphous ratio in thin-film and bulk samples.
- Measurements of average crystallite size, strain and substrate-film lattice mismatch in thin-film and bulk samples.
- Quantification of texture, multi-layer stacks, dislocation density in thin films.
- Qualitative examination of the film by rocking curve analysis.
- Determination of the film density, roughness and thickness using glancing incidence X-ray reflectivity method.

In case of nano-scale crystalline materials, the crystallite size is an important parameter which can be derived from the width of the XRD peaks as given by the Scherrer's formula (**equation (2.3)**) [2].

$$D = \frac{0.9\lambda}{\beta \cos\theta} \dots\dots\dots\dots\dots\dots\dots\dots\dots\dots(2.3)$$

where D is the crystallite size (length of the crystal in the direction perpendicular to the reflecting planes), β is the full width at half maximum (FWHM) of the Bragg reflection on 2θ scale.

Schematic and photograph of Bruker D8 Advance X-ray Diffractometer, used in the present study to characterize the samples, are shown in **figure 2.4 (a)** and **(b)**, respectively. Diffractometer, essentially, comprises an X-ray tube, an X-ray detector and a sample holder. The radiation of $\lambda =$ 1.54 Å (Cu K_α) originating from the X-ray tube using copper target are collimated and focused onto the sample. With the rotation of the sample and detector, the intensity of the reflected X-rays is measured. When incident X-rays hit some appropriate set of parallel planes at Bragg's angle 'θ', Bragg equation is satisfied and intensity peak corresponding to constructive interference appears. Suitable detectors are employed to record diffracted X-ray that are further converted in to appropriate signal and sent to printer or monitor as an output. The geometry of diffractometer

allows sample to rotate in the path of the focused X-ray beam at angle θ and the X-ray detector collects the signals and rotates at 2θ angle relative to the direction of incident X-ray beam.
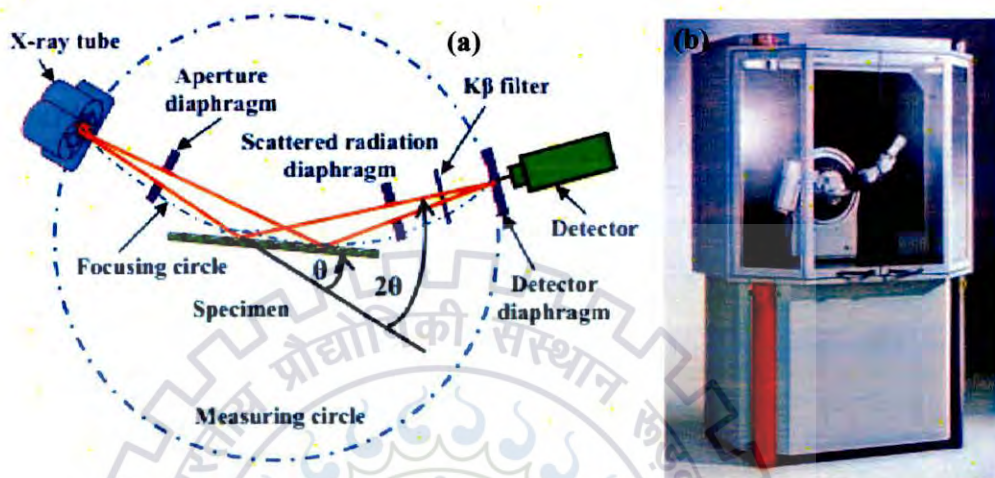
Figure 2.4. (a) Schematic diagram of beam path (b) Photograph of Bruker D8 Advanced X-ray diffractometer.

The hardware assembly used to control the angles and provide mechanism of rotation to the sample and detector is called goniometer. Bruker D8 Advance Diffractometer uses NaI scintillation counter as detector. It can detect the diffracted radiations in the wavelength ranging from 0.5 to 3 Å. Monochromators are arranged in the path of X-rays to suppress the undesired portions of X-rays. First aperture diaphragm is placed between specimen and tube to restrict the irradiated specimen area. A second aperture diaphragm is used to suppress scattered radiation coming from first aperture. The resolution of the signal is controlled by detector diaphragm.

2.3.2 Specimen beam interactions

When an incident electron beam strikes the specimen composed of a crystalline and amorphous structure, it undergoes a series of complex interactions with the nuclei and electrons of the atoms of the sample **(figure 2.5).** The interactions produce a variety of secondary products, such as:

Secondary electrons: When the specimen is struck by the primary beam, electrons are set free from the specimen. The electrons released from the surface are mostly low energy secondary electrons between 0 and 50 electron volts. They mainly give information about morphology and topology of the specimen.
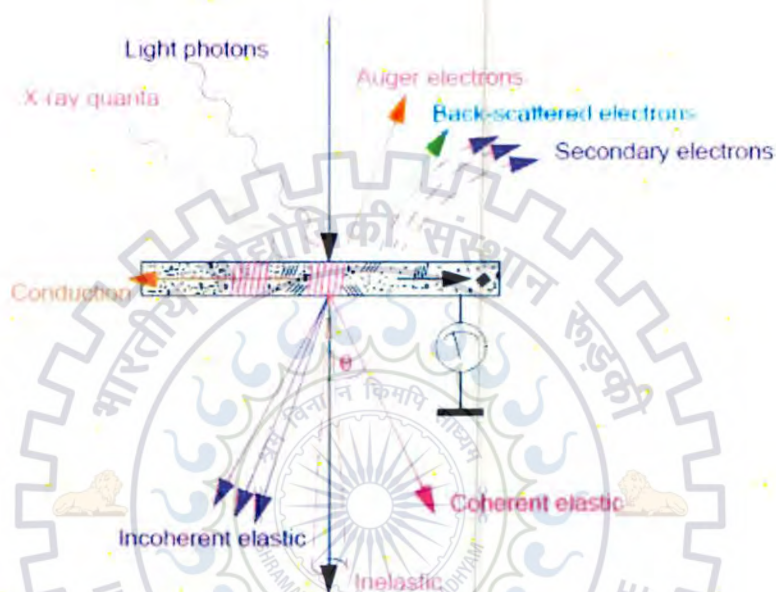
Figure 2.5. A schematic representation of the various interactions of an electron beam with a solid target.

Backscattered electrons: When the specimen is struck by the primary beam, electrons are elastically and non-elastically scattered back. Elastically means the primary electrons did not lose any of their primary energy. Back-scattered electrons provide information on the composition of a material, the so-called Z contrast or atomic number contrast.

Photons: Photons or light quanta are set free when the primary beam strikes a material like some minerals. These light quanta can be detected using a cathode luminescence detector. The light detected can vary from infrared to ultraviolet.

Auger electrons: Due to collisions with the primary beam, auger electrons are set free. These electrons are element specific and their energy can be detected using an auger mass spectrometer. This technique is applied for detection of light elements and gives information on the top atomic layers of the specimen.

X-ray quanta: X-ray radiation takes place when an electron has received extra energy, e.g. due to a collision with an electron of the primary beam. As this is an unstable situation, the electron will fall back into its original orbit, the extra energy is released in the form of an X-ray quantum.

Conduction: Electrons that are stopped in the specimen must leave the specimen, therefore all specimens that are not conductive are made conductive by an extra layer of gold or carbon. If the specimen was non-conductive it would start to become charged and thus an unwanted electrostatic lens would be made, which increases the inherent astigmatism.

Heat: The energy of the electrons stopped in the specimen is transferred to kinetic energy. The local temperature of the specimen can rise to temperature higher than 100 °C. The temperature depends on the acceleration voltage, the number of electrons (emission) and size (spot size) of the primary beam. If the temperature is too high for the type of specimen under investigation, the specimen will be damaged either in the form of contamination, evaporation, or complete tearing of the film layer.

Elastic scattering: Elastic scattering takes place when the negatively charged electrons are scattered due to interaction with the positively charged atomic nucleus. Because the mass of the nucleus is much higher than the mass of the electrons, therefore a negligible energy transfer takes place. This means that the speed and thus the associated wavelength of the electron do not change. There are two types of elastic scattering:

(a) Incoherent elastic scattering: This is the case when the specimen has an amorphous structure. The deflected electron waves have no phase relation to the specimen.

(b) Coherent elastic scattering: This is the case when the specimen has a crystalline structure. There is now a phase relation between the specimen and waves which are deflected under defined angles.

Inelastic scattering: Inelastic scattering takes place when the negatively charged electrons are scattered due to interaction with the negatively charged electrons. Now energy transfer takes place, this means that the speed and thus the associated wavelength of the electron changes.

2.3.3 Field emission scanning electron microscopy (FE-SEM)

Scanning electron microscopy mainly depends on the detection of SE, BSE and X-rays. Highly energetic monochromatic beam of electrons, needed for scanning microscopy, are produced from high performance electron guns developed from single crystals of lanthanum hexaboride (LaB_6) or an ultrafine tungsten tip (field emission guns) [6]. The filament is placed inside a Wehnelt

cylinder to focus and controls the number of electrons emitted from the gun. Electrons are accelerated towards anode at very high voltages of 2 to 50 kV [7]. The controlled electron beam, required for proper column optics, needs ultra clean dust free environment. Therefore, very high vacuum of the order of 5×10^{-5} torr is created inside the electron column with the help of one or two vacuum pumps [8]. The diameter of the electron beam used for scanning specimen is 5 nm to 2 μm. A schematic diagram of the optical column of the SEM is shown in **figure 2.6**. The electron beam, which typically has an energy ranging from a few hundred eV to 50 keV, is focused by two condenser lenses into a beam with a very fine focal spot size. The first condenser lens that works in conjunction with the condenser aperture helps to narrow the beam and also limit its current. The second condenser lens then makes the electron beam more thin and coherent. The objective lens does the final focusing of the beam onto the sample. During scanning, electron beam is thus made to deflect over the specimen in the raster form. At each point the number of secondary and back-scattered electrons reaching the detector are counted to be used for determining the relative intensity of the pixel representing that point in the final image.
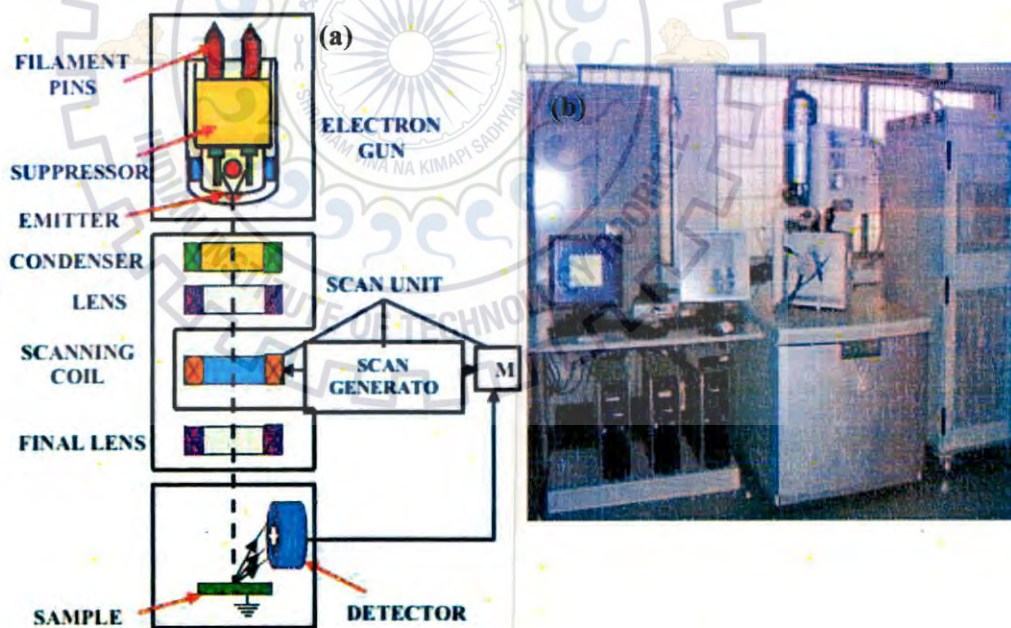
Figure 2.6. (a) Schematic diagram of the scanning electron microscope (b) Photograph of FESEM (FEI Quanta 200F).

The higher the atomic number of the specimen material, the greater is the number of secondary electrons that reach the detector, giving rise to a higher intensity in the image. Limitation associated with the SEM is that the specimen that has to be analyzed should be conducting. In case of non-metals, it is required to make them conducting by covering the sample with a thin layer of conductive material like gold or platinum in order to enhance the signals.

In the present study, field emission scanning electron microscope or FESEM (FEI Quanta 200F model) with resolution of 2 nm and magnification of 100000X was used to study the surface morphology of the deposited nanocomposite thin films (**figure 2.5 (b)**). FESEM uses field emission electron gun which is based on the basic mechanism of field emission i.e. electronic emission due to very high voltage applied between a pointed cathode and a plate anode. The cathode is generally a single crystal tungsten wire sharpened by electrolytic etching and having tip diameter of 100 to 1000 Å. FESEM provides better resolution than conventional SEM with minimum sample charging and damage. The field emission depends on the work function of the metal which is very sensitive to adsorbed gases. That further necessitates the requirement of very high vacuum in the electron column. Elemental analysis can also be performed by using the energy dispersive X-ray analysis (EDAX) attached to the FESEM system.

2.3.4 Atomic force microscopy (AFM)

Atomic force microscopy (AFM) maps out the topography of a surface by sensing the forces of interaction between the atoms belonging to the sample surface and the ones on the tip of the probe. One of the great advantages of the AFM compared to traditional microscopes such as the optical or scanning electron microscope is the ability to magnify in the x, y and z axis. In the present study, atomic force microscope from NT-MDT: NTEGRA was used and the photograph is shown in **figure 2.7 (a)**. **Figure 2.7 (b)** shows the schematic of AFM. To image the surface features, the sample is scanned by an atomically sharp tip, usually made of Si or Si_3N_4, attached to the lower side of a reflective cantilever. Light from a diode laser is focused on the cantilever and is reflected onto a segmented photodiode. As the sample is scanned below the tip, the cantilever moves up and down which changes the ratio of light falling on the four elements of the photodiode. The difference in the intensity falling on the four elements is converted into a proportional voltage by the photodiode. This voltage serves as a feedback signal enabling the tip to maintain either a constant force or a constant height above the sample. Atomic force microscope can be operated in one of three modes as described below:

(35)

(i)   **Contact Mode:** In this mode, the tip scans the sample in close contact with the surface. A repulsive force on the tip is set by pushing the cantilever against the sample surface with a piezoelectric positioning element. During scanning, the deflection of the cantilever is sensed and compared in a DC feedback amplifier to some desired value of deflection

(ii)   **Non-Contact Mode:** In the non-contact region, the cantilever is held on the order of tens to hundreds of angstroms away from the sample surface, and the attractive interatomic Van der Waals forces between the tip and sample are detected and topographic images are constructed by scanning the tip above the surface

(iii) **Semi-Contact or Tapping Mode:** In this mode, the cantilever is made to oscillate at its natural frequency by using a piezo-electric crystal. The oscillating tip is moved close to the sample surface till it begins to just tap it and is then immediately lifted off again, while the sample is continuously scanned below the tip.
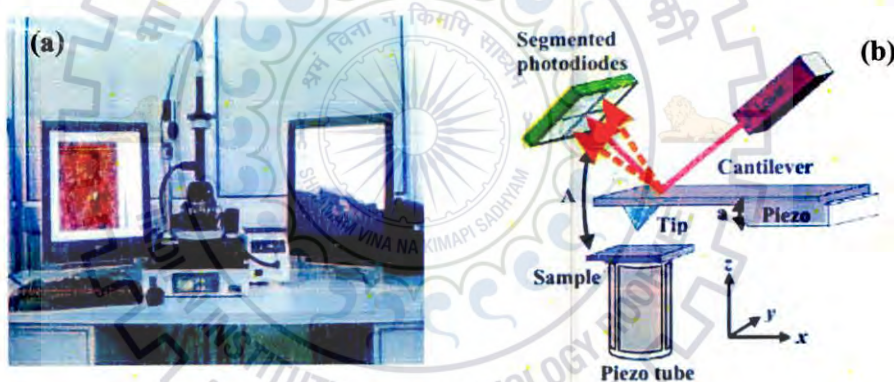
Figure 2.7. (a) Photograph of AFM (NT-MDT: NTEGRA) (b) Schematic diagram of AFM.

2.3.5 Electrical transport measurement

The temperature dependence of the sample resistance (R-T curve) was determined by standard four probe technique. This technique is used to eliminate both the lead resistance and the contact resistance. The sample resistance is determined by measuring the low voltage drop at two points of the film; generated by passing a constant current in the range of 1 µA-10 mA.

In the present study, four probe DC resistance measurement technique was used for the measurement of temperature dependence of sample resistance. The schematic diagram is shown in **figure 2.8 (a)**. Silver paste contacts were used for R-T measurement of the samples. The outer two

contacts were used for passing current in the samples and the corresponding voltage drop was measured across two inner contacts. A 100Ω platinum resistance thermometer (Lake Shore Cryotronics, USA) was used as temperature sensor in the range from 30 to 450 K. A heater of Lake Shore Cryotronics, USA was mounted below the sample holder and was used to heat the sample up to 50K. The temperature was controlled by temperature controller (Lake Shore, USA). The constant current was fed to the sample through a programmable current source (Keithley, USA 2400) and the voltage drop was measured by a digital nanovoltmeter (Keithley, USA 2182A). The automatic recording of data was done using computer Lab View software. The photograph of R-T setup with a closed cycle cryostat interfaced with Keithley instrument is shown in **figure 2.8 (b)**.
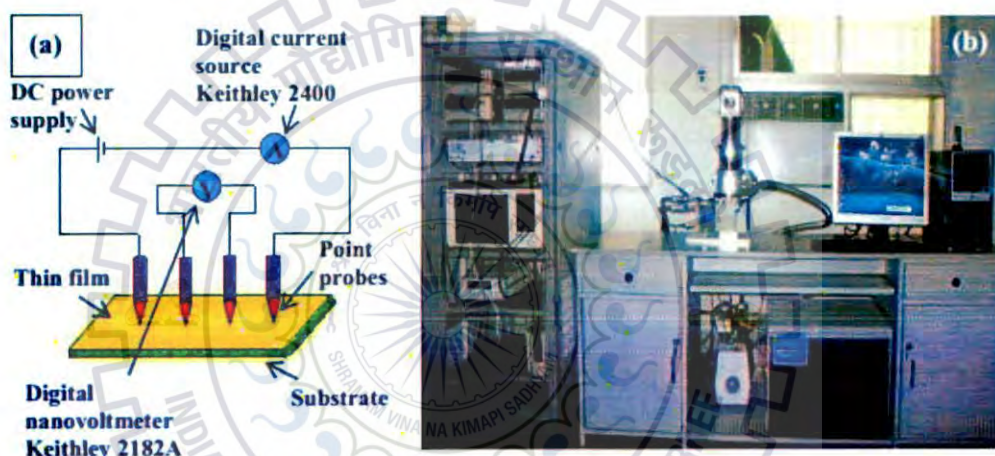
Figure 2.8. (a) Schematic diagram and (b) Experimental setup of four probe resistance measurement method.

2.3.6 Vibrating Sample Magnetometer (VSM)

A vibrating sample magnetometer is a scientific instrument that measures magnetization of a sample. It is based on Faraday's law of induction. In this instrument a magnetic is used to magnetize the sample. The magnetized sample is allowed to vibrate vertically inside of pick up coil. An e. m. f. is induced across this coil. This induced e. m. f. is a measure of the magnetization of the sample and causes an electric current in the coil. This current is proportional to the magnetization of the sample. The higher is the magnetization, the larger is the induced current. The induction current is amplified by an amplifier. The basic measurement of the magnetic moment by VSM is accomplished by oscillating the sample up and down near the pickup coil and

(37)

simultaneously detecting the induced voltage. The VSM consists primarily of a VSM linear motor transport (head) for vibrating the sample, a pick up coil set for detection, electronics for driving the linear motor transport and detection of the response from the pickup coils, and a copy of the Labview software application for automation and control. **Figure 2.9 (a)** shows the schematic diagram of VSM and **Figure 2.9 (b)** shows the photograph of VSM.
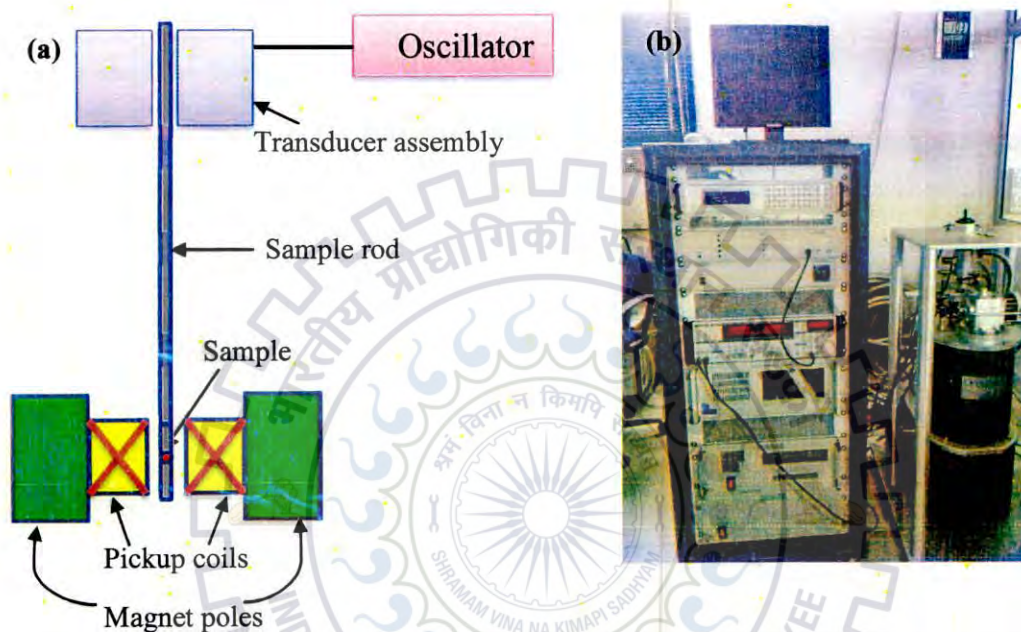
Figure 2.9. (a) Schematic diagram of VSM (b) Photograph of VSM (Cryogenic Ltd. UK) Functional Nanomaterials Research Laboratory, Department of Physics, IIT Roorkee.

2.3.7 Superconducting Quantum Interference Device (SQUID)

The SQUID magnetometer is extremely sensitive for measuring small magnetic signals and its sensitivity is up to 10^{-8} emu. SQUID uses the properties of Josephson junction to detect these signals. In a SQUID based magnetometer, magnetic sample passes through a set of sensing coils. The sensing coils are comprised of superconducting coils separated by thin insulating layers. The insulating layers are called Josephson junctions after Brian Josephson who, in 1962, showed that Cooper pairs (electron pairs in superconducting materials) in superconductors could tunnel through an insulating layer. The sample is moved through the sensing coils to generate a voltage signal as a function of sample position (**figure 2.10 (a) & (b)**).

Figure 2.11 shows the photograph of SQUID. The SQUID magnetometer is equipped with a sample rotator, which can rotate the sample about the measurement axis. This response curve is used to evaluate the sample's magnetic moment. If the sample is not centered, the coils read only part of the magnetic moment. Voltage readings that are taken as a function of samples position in the coils comprise the raw measurement data.
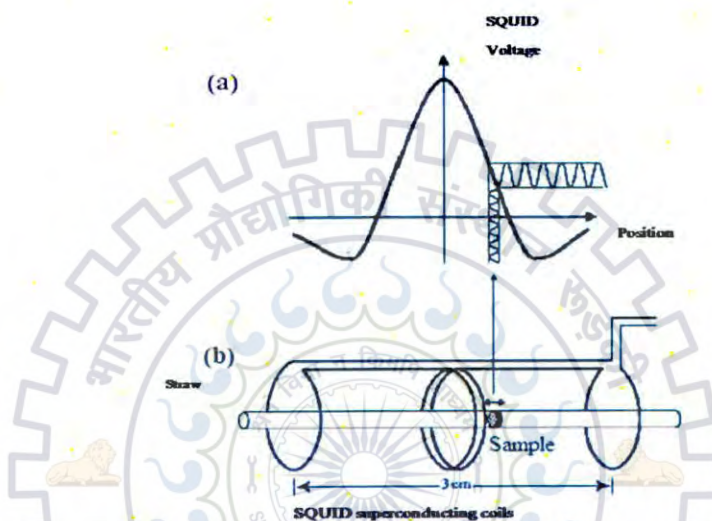
Figure 2.10. (a) The ideal SQUID response and (b) the movement of the sample within the SQUID superconducting coils.

The probe contains a high precision temperature control system, allowing measurements from 5K to 400K with an accuracy of 0.01K. The superconducting magnet system which provides reversible field operation up to ± 7 Tesla uses an oscillatory technique to minimize magnetic drift immediately following field changes. The sample handling system (sample translator and sample transport) allows automatic sample measurements and position calibrations using a microstepping controller having a positioning resolution of 0.0003 cm. The dewar consists of an inner liquid helium reservoir and outer liquid nitrogen jacket, to reduce excessive liquid helium boil off. Liquid helium system provides refrigeration for the superconducting detection system and magnet, as well provides the operation down to 5K. Sample is mounted within a plastic straw and connected to one end of a sample rod which is used to position the sample within the center of the SQIUD pickup coils. The SQUID detector system includes SQUID amplifier control electronics, sensing pick up loop and specially designed filtering with computer control via the interface computer.

(39)
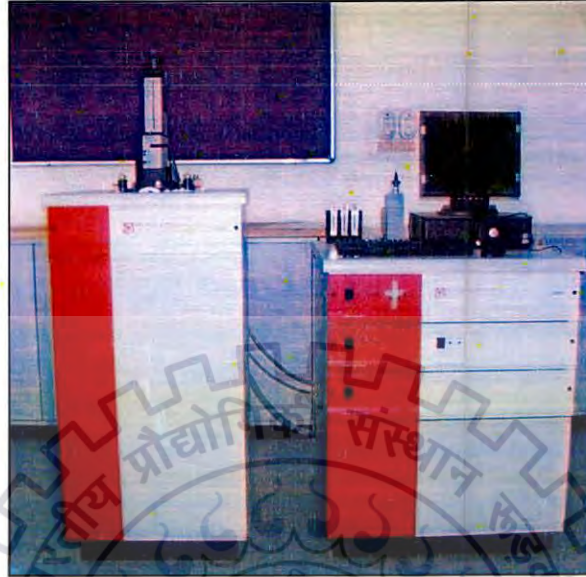
Figure 2.11. Photograph of SQUID (Quantum Design MPMS XL) at IIC, IIT Roorkee.

2.3.8 Nanoindentation

Nanoindentation is a powerful experimental technique which is being developed for more than a decade together with precise device fabrication, characterization of lower scale physical laws, theories and small scale numerical modeling. Nowadays, it is fairly widely used for assessing of mechanical properties of small material volumes at nano and micrometer range. NanoTest system (Micro materials, Wrexham, U.K) has been used in the present work and image of nanotester is shown in **figure 2.12 (a)**. It is a pendulum-based depth sensing system, with the sample mounted vertically and the load applied electromagnetically as shown schematically in **figure 2.12 (b)**. **Figure 2.13** depicts an example of a load versus displacement curve in which the load is increased at a constant rate to some peak value (loading), held at that value for a set of time, and then decreased to zero (unloading). Though many analyses exist for the interpretation of load-displacement data from nanoindentation, the most popular was proposed by Oliver and Pharr [9-10]. This is utilized throughout this work to determine hardness and modulus from indentation data. Oliver and Pharr determined that the unloading curve follows a power law relation (**equation 2.4**):

$$P = \alpha(h-h_f)^m \ldots\ldots\ldots\ldots (2.4)$$

where α and m are power law fitting constants.

(40)
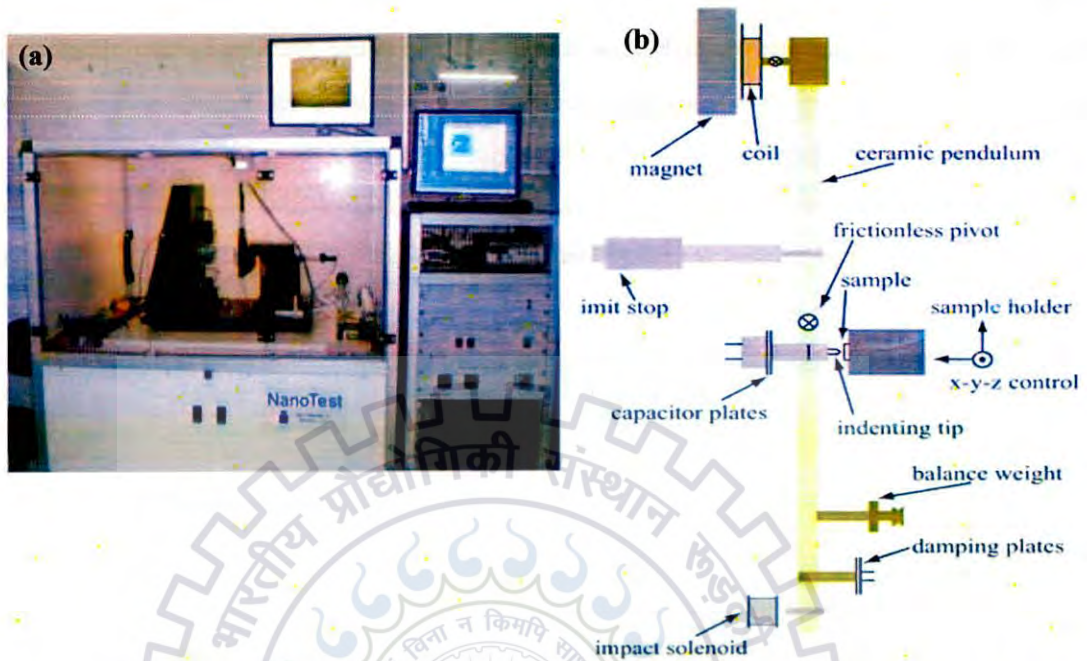
Figure 2.12. (a) Nanoindnetation (Micromaterials, UK) (b) Schematic diagram of Nanotest system.

The stiffness of the elastic contact, S, is the derivative of **equation 2.4**, dP/dh, evaluated at the peak load, P_{max}, and peak depth, h_{max}. Displacement of the surface surrounding the contact region is expected and differs from sink-in, which will be discussed later, in that it does not affect the contact area. The contact area is dictated by the indenter geometry,

$$A = F\left(h_c\right)\ldots\ldots\ldots\ldots(2.5),$$

where F is a function relating penetration depth to projected contact area for the indenter. This projected contact area is the cross sectional area of the indenter at the depth of interest. This is used, instead of the surface area in contact with the material, because it has a physical relationship to the stress applied to the sample.

The hardness (H) was calculated from the peak load (P_{max}) and the projected area of contact, A:

$$H = \frac{P_{max}}{A}\ldots\ldots\ldots\ldots\ldots\ldots\ldots\ldots.(2.6)$$

The contact area is determined from a probe calibration function A (h_c), where h_c, the contact depth, is found by using the equation:

(41)

$$h_c = h_{max} - \varepsilon \frac{P_{max}}{S} \dots\dots\dots\dots\dots\dots\dots\dots\dots\dots\dots(2.7)$$
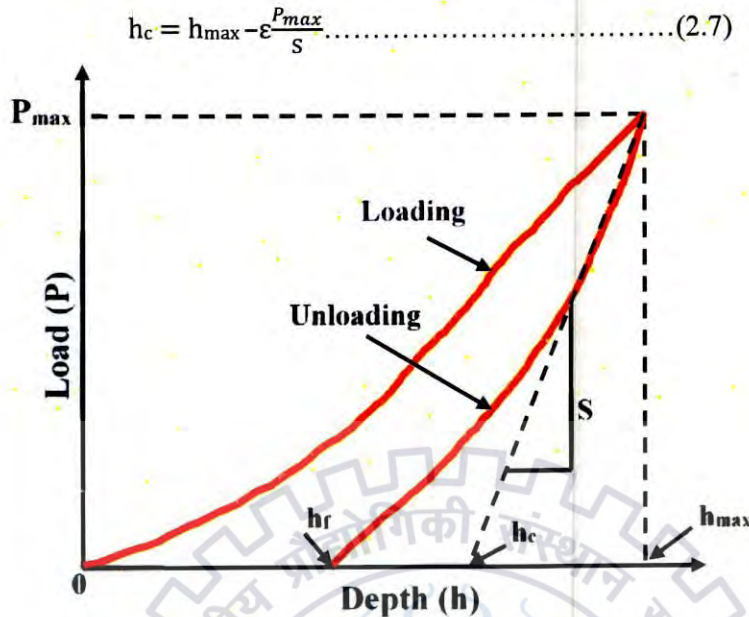
Figure 2.13. Load versus depth curve.

To obtain the reduced modulus, the unloading portion of the load-displacement curve is analyzed according to the relationship:

$$Er = \frac{\sqrt{\pi}}{2B} \frac{S}{\sqrt{A}} \dots\dots\dots\dots\dots\dots\dots\dots\dots\dots\dots(2.8)$$

where S (unloading stiffness) = dP/dh
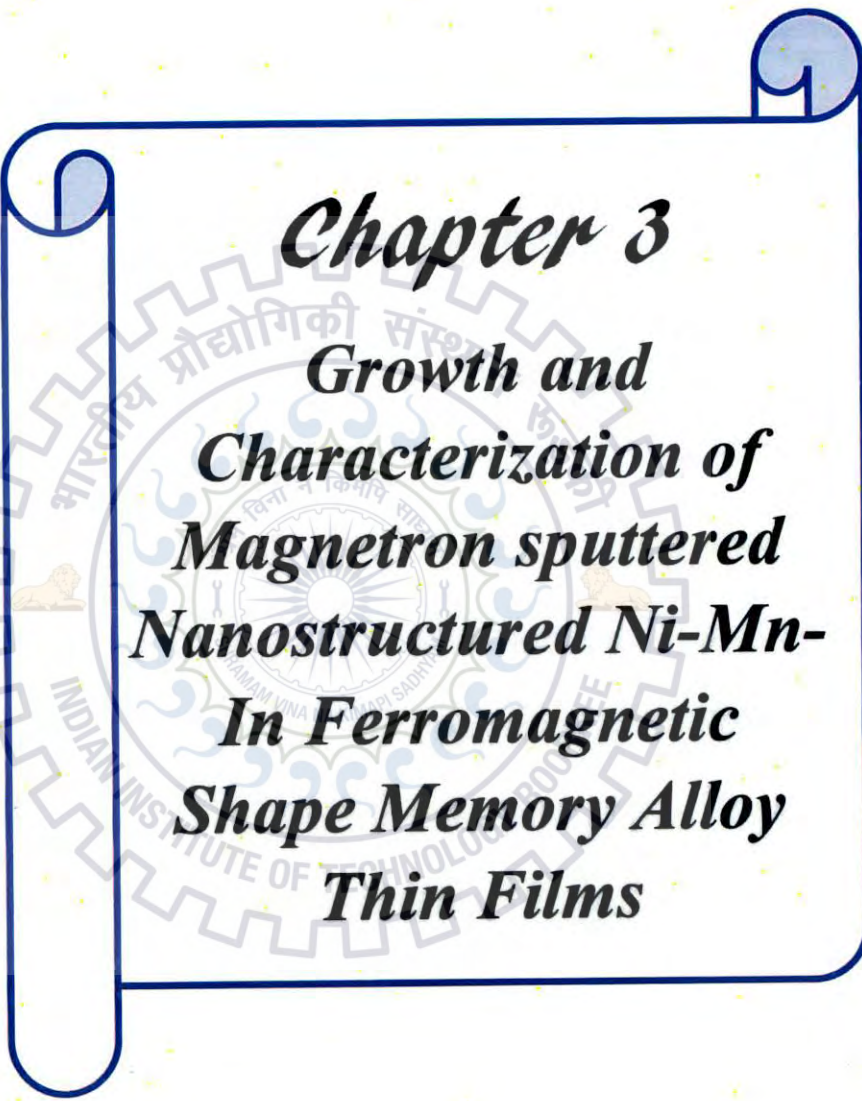
The reduced elastic modulus (E_r) is related to the modulus of elasticity (E) through the equation:

$$E_r = \frac{(1-v_i^2)}{E_i} + \frac{(1-v_s^2)}{E_s} \dots\dots\dots\dots\dots(2.9)$$
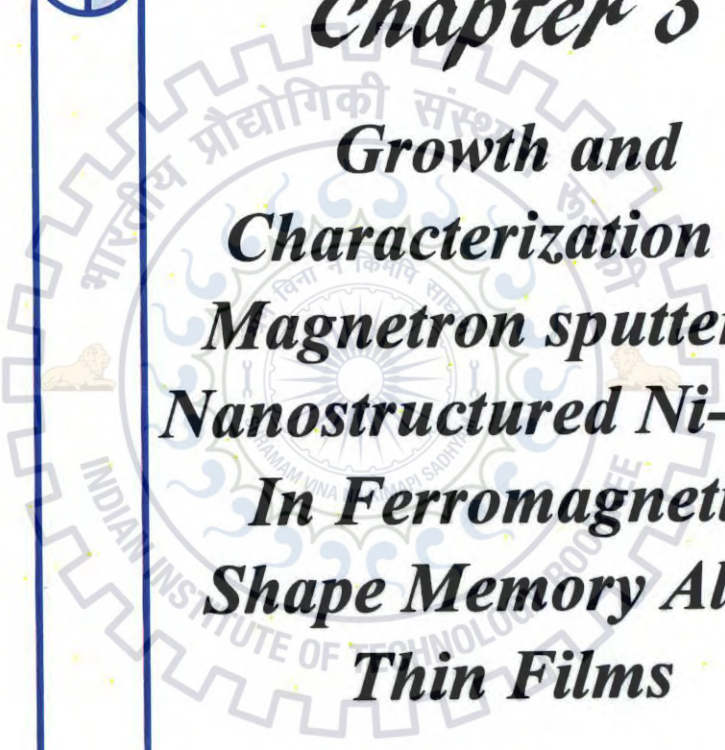
where the subscript i corresponds to the indenter material, the subscript s refers to the indented sample material, and v is the Poisson's ratio. For a diamond indenter probe, E_i is 1140 Gpa and v_i is 0.07 [11]. However, the most common use of nanoindentation is for the measurement of hardness and elastic modulus, but there has been considerable progress in the measurement of other mechanical parameters using nanoindentation technique such as nano-scratch, friction, wear, creep, impact and profilometry testing [12-13].

(42)

2.4 References

[1]   Ohring M., "Materials Science of Thin Films", Academic Press, New York (2006).

[2]   Cullity B. D., "Elements of X-ray Diffraction", 2nd Ed., Addission-Wesley Publishing Company (1978).

[3]   https://www.ionicviper.org/system/files/active/0/PowderXRD.doc.

[4]   http://serc.carleton.edu/research_education/geochemsheet/techniques/XRD.html.

[5]   http://epswww.unm.edu/xrd/xrdclass/01-xrd-intro.pdf.

[6]   Tarrant R., "The Scanning Electron Microscope", EXPERIMENT 31(2009- 2011).

[7]   Voutou B., Stefanaki E. C., "Electron Microscopy: The Basics" Physics of Advanced Materials Winter School (2008).

[8]   Cheney B., "Introduction to Scanning Electron Microscopy", Materials Engineering Department, San Jose State University, USA.

[9]   Oliver G. M., Pharr W. C., "An Improved Technique for Determining Hardness and Elastic Modulus Using Load and Displacement Sensing Indentation Experiments," *J. Mater. Res.*, **7**, 1564 (1992).

[10]   Oliver G. M., Pharr W. C., "Measurement of hardness and elastic modulus by instrumented indentation: Advances in understanding and refinements to methodology," *J. Mater. Res.*, **19**, 3 (2004).

[11]   Dhara S., Das C. R., Hsu H. C., Raj B., Bhaduri A. K., Chen L. C., Chen K. H., Albert S. K., Ray A., "Recrystallization of epitaxial GaN under indentation", *Appl. Phys. Lett.*, **92**, 143114 (2008).

[12]   NanoTest Manual Version P3, Micro Materials, Wrexham UK, September (2010).

[13]   Trelewicz J. R. Schuh C. A., "The Hall–Petch breakdown at high strain rates: Optimizing nanocrystalline grain size for impact applications", *Appl. Phys. Lett.*, **93**, 171916 (2008).

Chapter 3

Growth and Characterization of Magnetron sputtered Nanostructured Ni-Mn-In Ferromagnetic Shape Memory Alloy Thin Films

CHAPTER 3

GROWTH AND CHARECTERIZATION OF MAGNETRON SPUTTERED NANOSTRUCTURED Ni-Mn-In FERROMAGNETIC SHAPE MEMORY ALLOY THIN FILMS
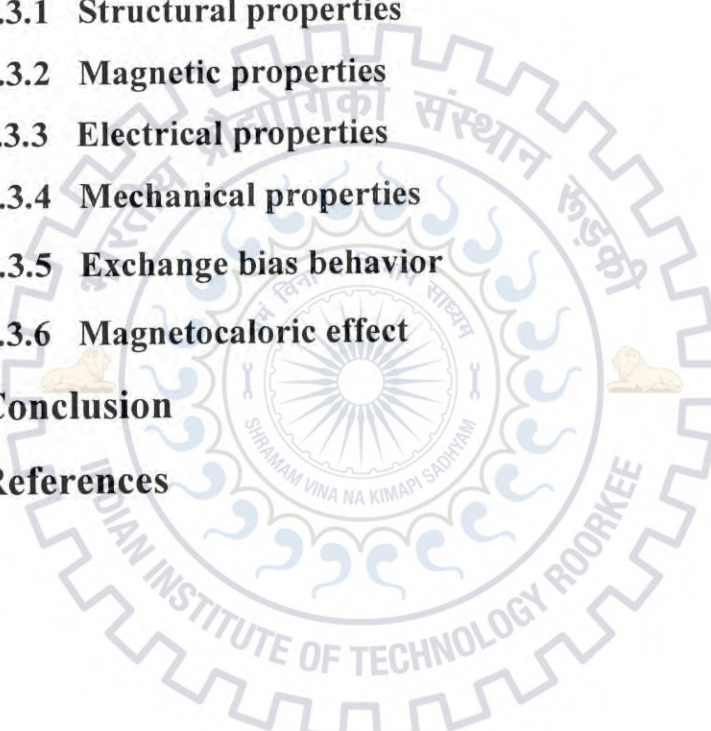
3.1 Introduction

Soon after discovery of large magnetic field induced strain (MFIS) in Ni_2MnGa single crystalline ferromagnetic FSMA alloy system [1], primarily Ni–Mn based FSMAs have received much attention due to their potential applications in magnetic sensors and actuators. Among these alloys, Ni–Mn–In alloys are a new class of materials owing to their multifunctional properties, namely the large magnetocaloric effect [2], magnetoresistance [3], magnetic field induced strain [4] and magnetic shape memory effect [5]. The exchange bias (EB) behavior was also reported in these alloys [6]. The remarkable properties of these alloys are usually addressed to the occurrence of any solid–solid displacive, diffusion less first order thermo elastic martensitic transformation (MT), which is taking place from high temperature austenitic phase (high-symmetrical) to a low temperature martensitic phase (low-symmetrical). Several authors have systematically studied the bulk form Ni–Mn–In alloy properties with various compositions; for example Krenke *et al.* [7] reported the structural and magnetic phase transformations in $Ni_{50}Mn_{50-x}In_x$ alloy with composition range $5 < x < 25$. Miyamoto *et al.* [8] observed the order-disorder transformation temperatures in the $Ni_{50}Mn_{50-x}In_x$ alloy with composition range $13 < x < 35$. The magnetic properties of $Ni_{2+x}Mn_{1-x}In$ have been investigated experimentally as well as theoretically [9]. Bhobe *et al.* [10] found an inverse magnetocaloric effect and large magnetoresistance in $Ni_{50}Mn_{35}In_{15}$ alloy at moderate field values. Consequently, there are few reports about doping atoms like Sn, Cu, Fe, Cr etc., inside the Ni–Mn–In alloy in order to improve magnetic properties as well as mechanical properties, to make it potential material for practical applications [11-13]. Many authors explored the physical properties of bulk Ni–Mn–In FSMAs, however for the effective use of these materials in emerging micro-devices, such as magnetically driven Micro-Electro-Mechanical- Systems (MEMS) and for faster response of these devices, thin films of FSMAs of high quality grown on semiconductor substrates are required [14]. The structural, magnetic and martensitic phase transformation properties of Ni–Mn–In alloys in the form of the thin film have been explored to a very little extent. Recently, Sokolov *et al.* [15] investigated the magnetic properties of $Ni_{50}Mn_{35}In_{15}$ FSMA alloy thin films deposited on single crystal MgO and $SrTiO_3$ (STO) (100) substrates using a laser-assisted molecular beam epitaxy method. Niemann *et al.* [16] analyzed growth conditions required to obtain metamagnetic transformations and magnetocaloric effects in epitaxial Ni–Co–Mn–In-films. In Ni–Mn-X (X = Sn, Sb and In) FSMA alloy thin films, the characteristic phase transformation temperatures are highly depending on the microstructure of the film which is often altered by

(46)

different variables like composition, substrate temperature, the thickness, post-deposition annealing, etc. However, for the use of FSMAs in MEMS applications, where the fast response frequency, higher recovery stress, and small dimensions are required, thin films with the thickness of few hundred nanometers are promising. For that reason, it is worthwhile to study the influence of film thickness on magnetic and mechanical properties. Thickness is one of the main parameter which would affect the microstructure, magnetic, electrical and mechanical properties of thin films and it is necessary to investigate in detail.

In the present study, attempts have been made to synthesize Ni-Mn-In FSMA thin films using dc magnetron sputtering on Si (100) substrate at 823 K without post annealing. Precise control of sputtering parameter was done to obtain high-quality thin films. Then the influence of film thickness on structural, magnetic, electrical and mechanical properties of these films was studied in detail. The investigation reveals the increase in grain size, saturation magnetization, martensitic transformation temperature and decrease of mechanical hardness and elastic modulus of the films with corresponding increase of film thickness.

3.2 Experimental details

The various thicknesses of Ni-Mn-In thin films starting from 90 to 655 nm were grown on silicon (100) at a temperature of 823 K using dc magnetron sputtering technique. The $Ni_{50}Mn_{35}In_{15}$ alloy of 50.8 mm diameter and 3 mm thickness was used as a sputtering target material. The thicknesses of the films were simply governed by changing the deposition time. Before every deposition, the target was pre sputtered for 5 minutes to obtain the same state of the target. The deposition parameters for the films were given in **table 3.1**. Post annealing was not performed after the deposition. The cross-sectional Field Emission Scanning Electron Microscope (FESEM) was used to measure the films thicknesses and found to be 90, 153, 360, and 655 nm, which are represented as films A1, A2, A3 and A4, respectively. The FESEM attached energy dispersive X-ray analysis (EDAX) was used to determine the compositions of the films and found to be same as the target composition (**Table 3.2**). The crystallographic orientations of the deposited films were analyzed using a Bruker advanced diffractometer of Cu K_α (1.54 Å) radiations in θ-2θ geometry at a scan speed of 1°/min. The microstructure and surface morphology were studied using FESEM (FEI Quanta 200F model) and atomic force microscope (NTEGRA model). The average roughness of the surface of films was calculated from atomic force microscope scans over substrate areas of

$1 \times 1 \ \mu m^2$, carried out four times at various places for each sample. The magnetic properties were studied with a vibrating sample magnetometer (VSM, cryogenics, UK). The M–H loops of the films were recorded at various temperatures with magnetic fields up to ±2 T. Further, the temperature dependence magnetization (M–T) measurement were performed to characterize the phase transformation behavior of the films with varying temperature ranging from 10 K to 330 K under field cooled (FC) and field heating (FH) cycles. The resistivity versus temperatures (R–T) measurements were performed by four-probe resistivity method over temperature range from 100 K to 350 K. The mechanical properties were studied using depth-sensing nanoindentation (Nano Test, Micro Materials Ltd., Wrexham, UK). Multiple load-depth nanoindentation experiments were performed with a diamond Berkovich indenter (tip radius = 100 nm) at room temperature. A constant load 2 mN was applied for the nanoindentation of each sample. Loading and unloading rates were kept constant at 0.1 mN/s. To prevent the substrate effect on the indentation response of the films, the maximum load is selected such that the indentation depth is within 10% of the film thickness.

Deposition Process	Magnetron sputtering
Target	$Ni_{15}Mn_{35}In_{15}$
Base pressure	$\leq 2 \times 10^{-6}$ Torr
Gas used	Argon
Sputtering pressure	10 mTorr
Deposition time	5, 10, 15, 20 minutes
Sputtering power	110 W
Substrate	Silicon (100)
Substrate temperature	823 K
Substrate to Target distance	5 cm

Table 3.1. Sputtering parameters for Ni-Mn-In thin films.

3.3 Results and Discussion

3.3.1 Structural properties

Figure 3.1 (a) shows the room temperature XRD pattern of different thicknesses of Ni–Mn–In thin films. The XRD results revealed that the A1 film showed a broad fundamental (220) peak along with small super lattice reflections of (111) and (311) which are indexed to austenitic cubic $L2_1$ structure. Further, A2–A4 films also exhibit the austenitic cubic $L2_1$ structure with a high intensity fundamental lattice reflection of (220) and super lattice reflections of (111) and (311), which implies that the martensitic temperatures are lower than the room temperature. It can be seen that for A1–A4 films, the intensity of the (220) diffraction peaks has become more intense and sharp with increase of film thickness, resulting the improvement in the crystallinity. Usually, an
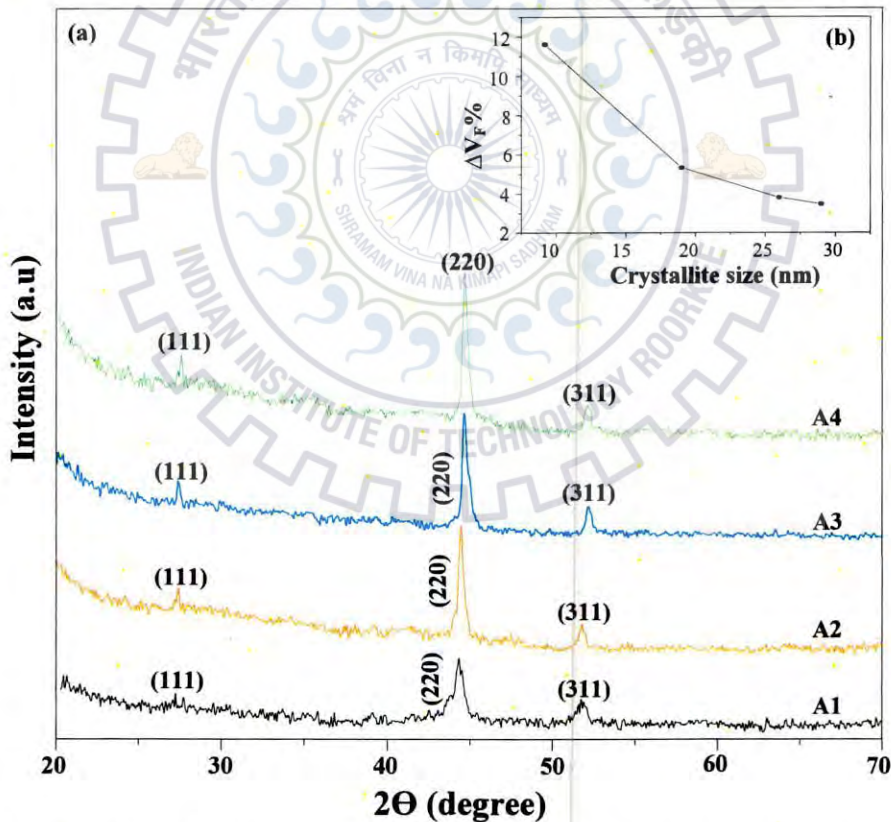
Figure 3.1. (a) XRD pattern and (b) the variation of free volume versus crystallite size of A1, A2, A3 and A4 films.

increase of film thickness increases the possibility of crystallization. With an increase in film thickness, the strain imposed by the film-substrate interface decreases which usually promotes the grain growth as proved by the increased intensity of different reflections. The average crystallite size values are calculated by Debye–Scherrer formula using the FWHM of (220) reflection and found to be 9.2, 19, 26 and 29 nm for the films A1, A2, A3 and A4, respectively (**Table 3.2**). **Table 3.2** shows that the crystallite size values increases with an increase in film thickness that might be due to the fact that the mobility of sputtered adatoms is increased by surface heat causing accumulation of energetic sputtered particles. Moreover, the fundamental (220) austenite peak began to shift toward higher angles for the A1 to A4 films, which indicates that residual microstrain was developed between the substrate and film with a variation of thickness. The developed residual microstrain calculated using $\delta = [(a_{substrate}-a_{film})/a_{substrate}]$, where a is the lattice constant of substrate/film, is observed to be compressive in nature with negative δ value. The values of δ has been found to be -0.0601, -0.0592, -0.0581 and -0.0570 for sample A1 to A4, respectively (**Table 3.2**). It can be observed that the strain is decreasing with an increase in film thickness. In the present study, the increase in grain size with film thickness result in the suppression of higher strained region, which in turn decreases the microstrain in the films. Generally, in bulk materials the conventional grain growth is due to decrease in free energy of the system with an increase in temperature. Nevertheless, in the current situation for various thicknesses of films, the grain growth is governed by the lattice misfit and lattice strain enforced by the substrate on the film which varies with film thickness. Hence, the conventional grain growth may not enough to describe the observed grain sizes of the films. Two essential driving forces are required for grain growth: (i) decrease in grain boundary free energy (ii) decrease in surface strain energy. The density of grain boundaries is less than that of perfect crystallite due to the excess free volume of grain boundaries. The excess free volume associated with the grain boundaries can be calculated using **equation (3.1) [17].**

$$\Delta V_F = \frac{(L+d/2)^2 - L^2}{L^2} \dots\dots\dots\dots\dots\dots\dots\dots\dots\dots\dots(3.1)$$

where L is the crystallite size and d is the mean width of the grain boundaries.
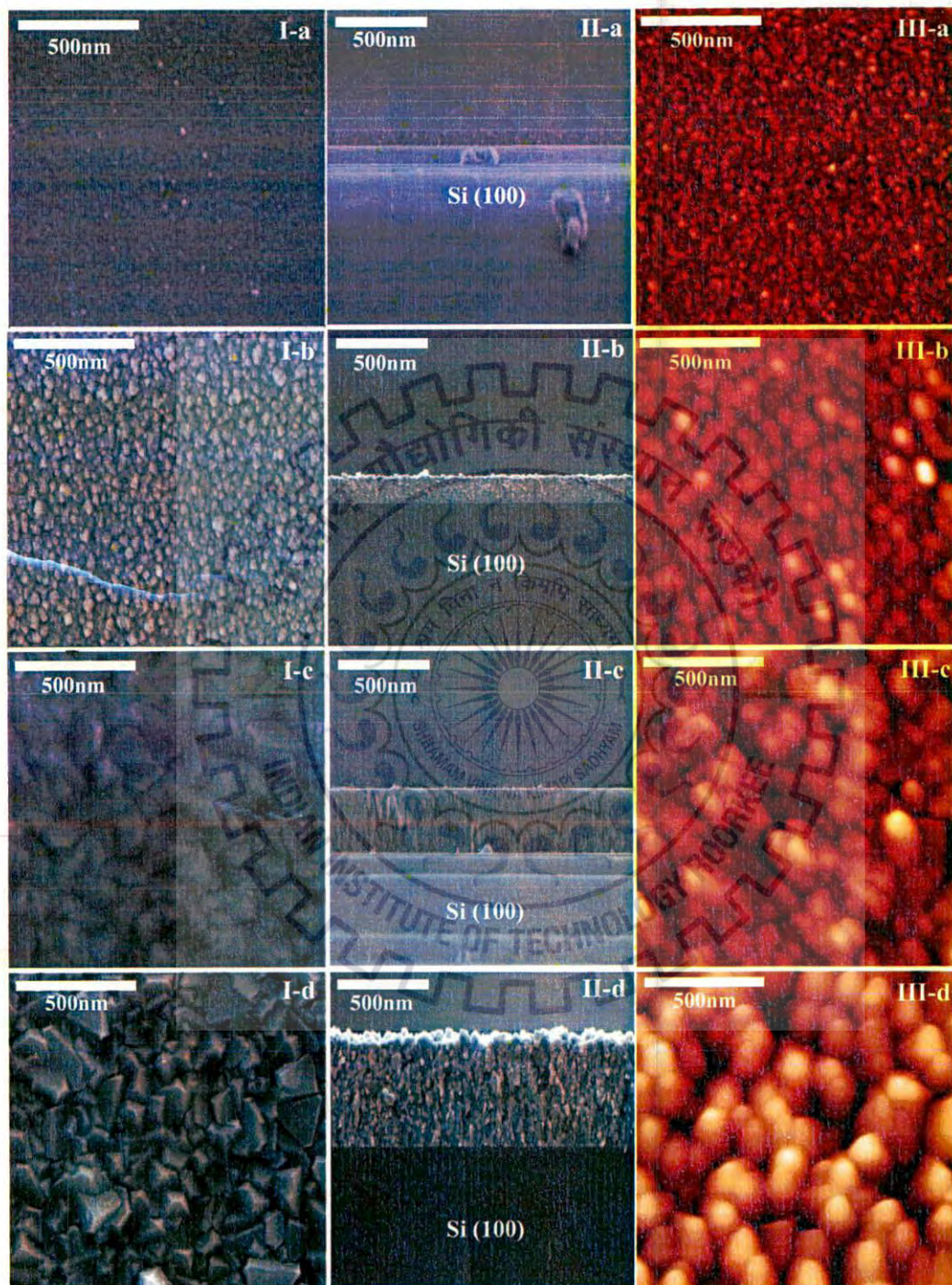
Figure 3.2. I(a–d) FESEM images, II(a–d) FESEM cross sectional images and III(a-d) atomic force microscope images of films A1, A2, A3 and A4, respectively.

(51)
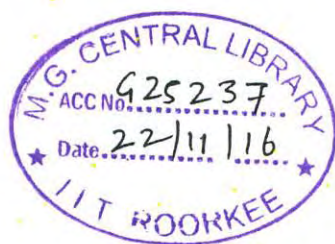
In many previous calculations of the excess free volume, the grain boundary width has been assumed to be constant ($d = 1$ nm), independent of the grain size [18]. Inset of **figure 3.1 (b)** shows the variation of free volume calculated with crystallite size of Ni–Mn–In thin films. When a crystallite size decreases in the material, the number of grain boundaries increases as a result increase in grain boundary free volume [19]. **Figure 3.2** shows the FESEM, cross-sectional FESEM and atomic force microscope micrographs of A1, A2, A3 and A4 films. Both FESEM and atomic force microscope micrographs replicate that the grain size increases with an increase in film thickness (**Table 3.2**), and are also in good agreement with the XRD results. The average grain size values observed by FESEM for the films A1, A2, A3 and A4 was found to be 14, 48, 86, and 95 nm, respectively. The calculated grain sizes determined by FESEM and atomic force microscope are quite similar. Nevertheless the overall particle size determined by FESEM as well atomic force microscope micrographs demonstrate agglomeration of the particles, in contrast XRD gives a typical average mean crystallite size. The actual XRD and also FESEM/atomic force microscope data could be reconciled with the belief that smaller primary particles employ a large surface free energy and would certainly therefore, have a tendency to agglomerate rapidly and develop into larger grains. The cross sectional FESEM micrographs show the clear interface between the substrate and film, which indicates that there is no diffusion at the interface. For the quantitative estimation of surface topography, the average roughness (R_{avg}) of the surface were obtained from AFM scans over film areas of 1×1 μm^2, three times at a different spot for each sample by using the following equation [20]:

$$R_{avg} = \frac{1}{N} \sum_{i=1}^{N} |Z_i - \bar{Z}| \quad \dots\dots\dots\dots\dots\dots\dots\dots(3.2)$$

where N is the number of surface height data and $\bar{Z}$ is the mean height distance. AFM topography reveals that the average roughness (R_{avg}) is increased with increase of Ni–Mn–In thickness and values are reported in **table 3.2**

Sample	Thickness (nm)	Lattice parameter a (Å)	Microstrain (δ)	Crystallite size XRD (nm)	Avg. grain size (nm)		R_{avg} (nm)	Composition from EDAX (at%)		
					FESEM	Atomic force microscope		Ni	Mn	In
A1	90	5.758	-0.0601	9.2	14	15	4.8	50.10	34.96	14.94
A2	153	5.754	-0.0592	19	48	49	11	50.11	34.95	14.94
A3	360	5.749	-0.0581	26	86	88	32	50.12	34.96	14.92
A4	655	5.740	-0.0570	29	95	98	36	50.10	34.98	14.92

Table 3.2. Various parameters for different thickness of Ni–Mn–In films.

3.3.2 Magnetic properties

The temperature dependent magnetization (M–T) curves for 90, 153, 360, and 655 nm thickness films were studied using VSM in the temperature range between 10 K and 330 K in an applied magnetic field of 0.02 T and are shown in **figure 3.3**. The magnetization data have been corrected with a constant diamagnetic contribution of the Si (100) substrate using the equation:

$$M_{film} (H) = M_{total} (H) - \chi_{substrate} .H \dots\dots\dots\dots\dots\dots\dots(3.3)$$

where $\chi_{substrate}$ is the susceptibility of the substrate, M_{total} is the magnetization of film substrate, and H is the applied magnetic field. The A2, A3 and A4 films exhibit the structural and magnetic transformation points along with slight change in the magnetic moment. The Curie temperature was determined by differentiation of magnetization data. **Figure 3.3(a)** shows the thermo magnetic curve of film A1 of thickness 90 nm. In the A1 film, there is no sign of first order phase transformation between martensitic and austenitic phase (an indication of thermal hysteresis between FC and FH curves) which is evidenced by the continuous decrease in magnetization with increase in temperature. The possible lack of first order phase transformation behavior in this film is caused by the following reasons: (a) the numerous grain boundaries at lower film thickness can restrict the martensitic phase growth and confine the transformed volume fraction in the nano grained structures; (b) the spatial constraints imposed by the film and substrate due to large lattice misfit can lead to an increase in lattice strain and the twinned structure density [21-22] and (c) some sort of martensitic variants nucleated within a grain is going to be stopped at the grain boundaries, acting as obstacles intended for martensitic growth [22]. In order to propagate the actual transformation, the martensitic variants need to exert stress which should be sufficient to be able to stimulate nucleation along with growth associated with favorable martensitic variants within the adjacent grains. The (M–T) curves of sample A2, A3 and A4 clearly indicate the first order phase transformation between martensitic and austenitic phase and vice versa during subsequent field heating and field cooling cycles (**Figure 3.3 (b)–(d)**). Film A2 had shown weak signs of first order phase transformation between FC and FH modes with a small hysteresis loop. The austenitic Curie temperature (T_C^A) was 291 K and thermal hysteresis width was 26.5 K. In case of A3, it was observed that, a clear well shaped thermo magnetic curve between FC and FH modes except that the characteristic temperatures (M_s, M_f, A_s and A_f) were shifted toward higher temperatures as shown in **figure 3.3 (c)**. Film A3 undergoes the second order magnetic transition

(54)
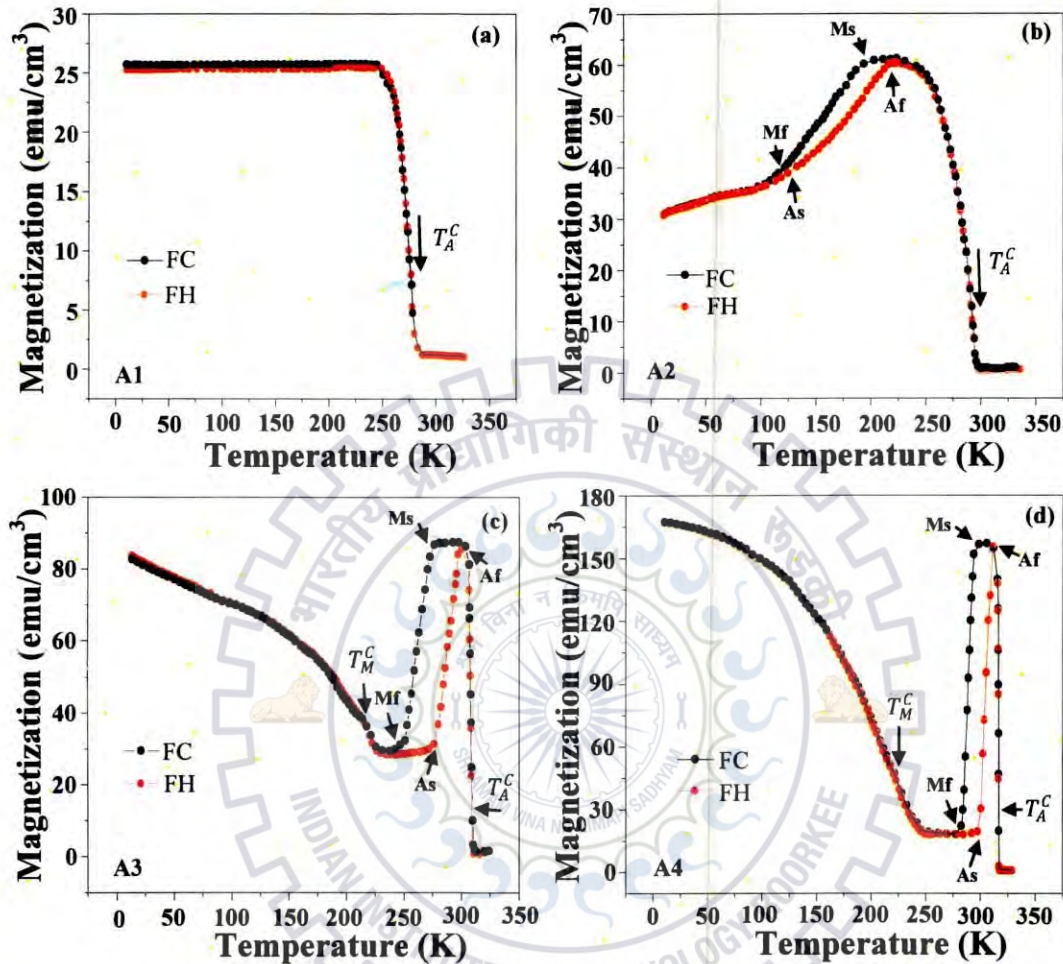
Figure 3.3. Field cooled (FC) and field heating (FH) (M-T) curves obtained in
A1, A2, A3 and A4 films, respectively.

at T_C^A = 311 K. The start and finish temperatures of the martensite phase transformations are M_s =
274 K and M_f = 249 K, while those for austenite are A_s = 277 K and A_f = 299 K. The thermal
hysteresis of phase transformation is 25 K. In case of A4 film (**Figure 3.3 (d)**), the magnetization
sharply increases to maximum value during FC mode, this can due to second-order magnetic phase
transformation from paramagnetic (PM) to ferromagnetic (FM) transformation in austenitic state
at ferromagnetic Curie temperature (T_C^A = 317 K) of austenite phase. It shows an abrupt decrease
in martensite start temperature (M_s = 292 K) and reaches a minimum value of martensite finish

Sample	Thickness (nm)	M-T temperatures (K)							R-T temperatures (K)						S_M (emu/cm³)	H_{EB} (T)	H_C (T)	ΔS_M (mJ/cm³ K)	RC (mJ/cm³)
		M_s	M_f	A_s	A_f	ΔT	T_C^M	T_C^A	M_s	M_f	A_s	A_f	ΔT	T_C^A					
A1	90	---	---	---	---	---	---	275	---	---	---	---	---	274	163	---	---	---	---
A2	153	195	113	123	218	26.5	---	291	174	130	155	202	26.5	280	190	---	---	---	---
A3	360	274	249	277	299	25	214	311	273	233	263	294	25	315	241	---	---	---	---
A4	655	292	281	297	310	17	215	317	299	283	297	313	14.5	325	283	0.0096	133×10⁻⁴	15.2	155.04

Table 3.3. Transition temperature values obtained from M–T and R–T curves and S_M values of Ni–Mn–In films of different thicknesses, H_{EB}, H_C, ΔS_M and RC values obtained in A4 film.

temperature (M_f = 281 K). To further decrease in temperature, an FM-like transformation was observed around 214 K. This temperature is defined as T_C^M and represents the FM Curie temperature of the martensitic phase. The similar transformation temperature was also observed in bulk Ni–Mn–In alloy [23]. In FH mode, the magnetization decreases with increasing temperature and FH curve retraces the FC curve up to austenitic starting temperature A_s = 297 K. Then magnetization sharply increases and reaches an austenitic finish temperature A_f = 310 K. The thermal hysteresis was observed between the FC and FH cycles, which is conforming to the occurrence of first order structural transition from highly symmetric austenite phase to less symmetric martensitic phase. In FH and FC cycles, the behavior of the A4 film is similar to that of A3 film with the exception that the characteristic phase transformation temperatures M_s, M_f, A_s, and A_f are shifted toward higher temperatures (values given in **table 3.3**) and the phase transformation hysteresis width is slightly decreased (17 K). The magnetization values in this film are considerably higher than those of films A2 and A3. Generally, the martensitic phase transformation behavior of FSMAs depends critically on the microstructure and dimensional constraint. Sputter-deposited thin films are usually found to be under a stressed condition when the substrate is still attached [24]. The induced stress in the substrate - attached thin films also strongly affects the martensitic phase transformation characteristics. In this study, the complete phase transformation behavior in A4 film is due to the increase in grain size approaching the value needed for the growth of martensitic variants and reduces the constraints so that complete martensitic transformation takes place. The above said discussion clears that the A4 film (thickness 655 nm) exhibits the prominent phase transformation behavior compared to other films (A1, A2 and A3). The following parameters could be responsible for prominent phase transformation in the A4 film i.e., (a) decreased number of grain boundaries (higher grain size), because the constraints imposed by the grain boundaries on the growth of martensitic phase will be suppressed (b) low interfacial strain between film and substrate.

The field dependence magnetization (M–H) loops were taken at 10 K to confirm the ferromagnetic nature of these films and are shown in **figure 3.4**. The hysteresis loops were measured as parallel to the film surface. In order to determine the saturation magnetization (S_M), the loops are analyzed in the high field region ±2 T and corresponding values are listed in **table 3.3**. It was found that the saturation magnetization increases with increasing thickness of the films.

Film A4 showed higher saturation magnetization (283 emu/cm^3) than the other films. This could be attributed to higher grain size and low film-substrate interfacial strain.
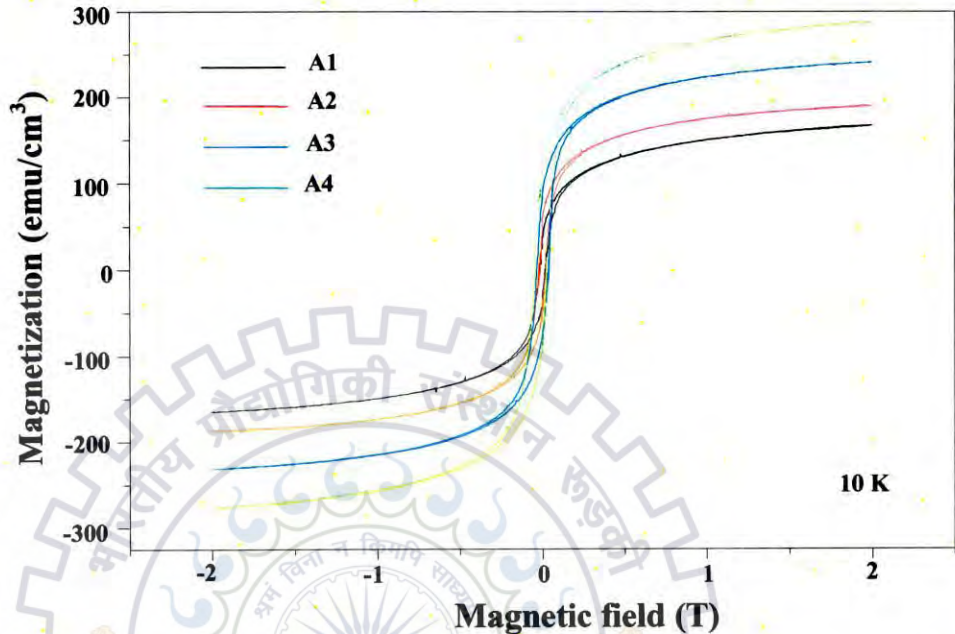
Figure 3.4. M-H loops of A1, A2, A3 and A4 films measured at 10 K.

3.3.3 Electrical properties

Figure 3.5(a)–(d) shows the resistance versus temperature (R–T) curves of different thicknesses of Ni–Mn–In thin films corresponding to films A1, A2, A3 and A4, respectively and their corresponding phase transformation temperatures are summarized in **table 3.3**. The martensitic start and finish phase transformations are denoted by M_s and M_f, whereas A_s and A_f represent the start and finish temperature of the reverse transformation to the austenitic phase. The variation in resistance with temperature was found to differ with Ni–Mn–In thickness. When the Ni-Mn-In film thickness increased to above 153 nm, the first-order phase transformation behavior was observed during heating and cooling in the temperature range of 100–350 K. The R-T curve of A1 film showed metallic like behavior without any indication of first-order phase transformation during heating and cooling cycles (**Figure 3.5(a)**). The lack of phase transformation behavior in this particular film could be a result of the presence of higher quantity of grain boundaries at a lower thickness which in turn restricts the actual martensitic phase growth.
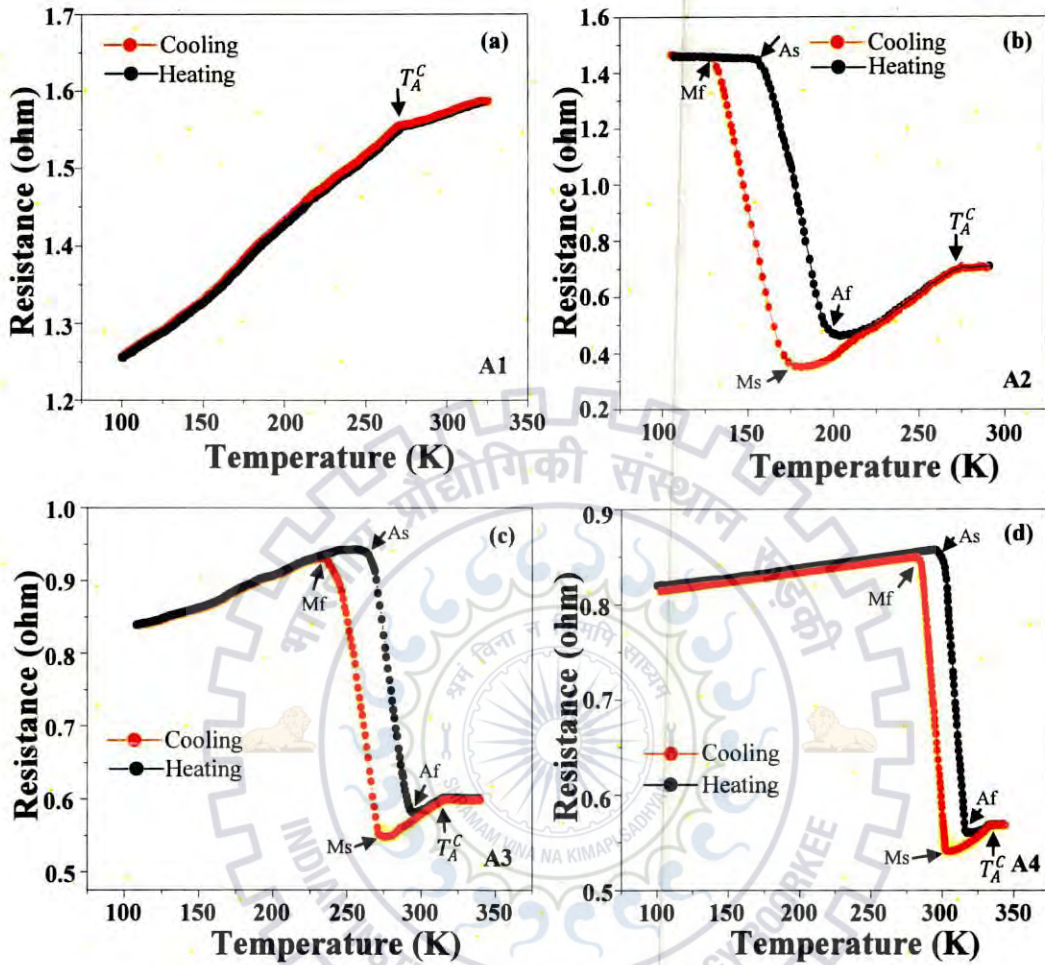
Figure 3.5. Electrical resistance versus temperature (R-T) curves of A1, A2, A3 and A4 films, respectively.

It can be seen that with increase in Ni–Mn–In film thickness the corresponding grain size increases which in turn reduces the constraints imposed by grain boundaries and results in the formation of prominent shape memory behavior. From **figure 3.5 (b)**, it can be seen that the A2 film exhibited martensitic phase transformation in the temperature range from 174 to 130 K with broad hysteresis loop. **Figure 3.5 (c)** shows the R-T curve of A3 film (thickness = 360 nm) which also exhibits the first-order phase transformation behavior during subsequent heating and cooling cycles. When the temperature increases, the resistance is comparatively constant till the temperature reached to about 263 K after which it decreases rapidly at the martensitic transformation. With further increase in temperature, the resistance increases linearly until it reaches about 315 K, where the slope of the

curve changes due to second order transformation from ferromagnetic austenitic to paramagnetic austenitic state. The sudden fall of electrical resistance throughout the martensitic transformation might be ascribed toward the formation associated with super zone boundary gaps, which adjusts the occurrence of electronic states nearby the Fermi surface [22, 25]. For the film A4 (**Figure 3.5(d)**), the electrical resistance as a function of temperature is similar to the film A3 except that the respective transformation temperatures, during heating and cooling cycles, of film A4, are shifted to higher temperatures.

3.3.4 Mechanical properties

Nanoindentation is really a powerful method to measure the actual mechanical properties such as hardness, elastic modulus along with other properties associated with materials within nano range dimensions. **Figure 3.6** shows the typical load–displacement curves for different thicknesses of Ni-Mn-In films corresponding films are A1, A2, A3 and A4, respectively. The maximum load applied in this measurement was 2 mN for all the films. The indentation curves were used to determine average hardness (H), elastic modulus (E), plasticity index (H/E), resistance to plastic deformation (H^3/E^2), the depth recovery ratio (δ) and their values are summarized in **table 3.4**. The hardness and elastic modulus were measured by Oliver and Pharr method [26]. It was observed that the hardness and elastic modulus get influenced by the thickness of the films. The higher hardness (7.2 GPa) and elastic modulus (190 GPa) were found in sample A2 as compared to other films. The average hardness decreased almost linearly with increasing thickness of the Ni–Mn–In films. This can be attributed to the two factors, (1) with thickness, grain size increases and (2) grain refinement which obeys the well-known Hall–Petch relationship.

$$\sigma = \sigma_0 + \frac{k}{d^{1/2}}\dots\dots\dots\dots\dots\dots\dots\dots\dots\dots(3.4)$$

where σ is the yield stress, σ_0 is a materials constant for the starting stress for dislocation movement, k is the strengthening coefficient and d is the average grain diameter. This equation is valid only when the grain size is approximately greater than the tens of nanometer. Further decrease in grain size leads to a reduction in strength as a result of grain boundary sliding.
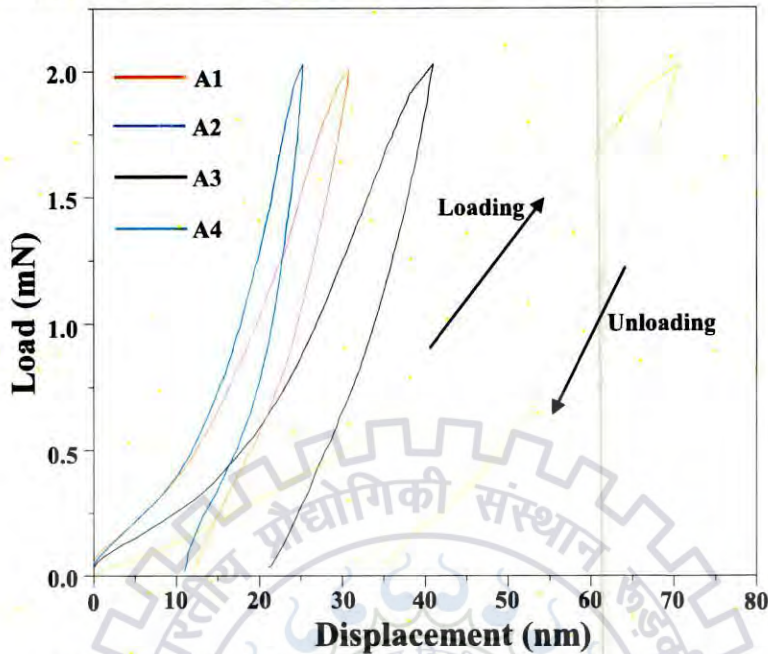
Figure 3.6. Load versus depth curves obtained in A1, A2, A3 and A4 films.

The measured hardness decreases below the critical grain size of 19 nm and this may be ascribed to grain boundary sliding mechanisms. Softening initiated by the grain boundary sliding is especially ascribed to a wide range of defects within grain boundaries, which permit fast diffusion involving atoms and vacancies within stress. It is observed that the yield strength of the material is strongly influenced by the grain size. The increase in hardness a result of large variety of grain boundaries which act as a barrier to the dislocation movements. Therefore, grain boundaries become a pinning thing and impede this dislocation propagation. As a way to obtain excessive hardness, generally plastic deformation will be strongly disallowed, and dislocation activity and grain boundary slipping are eliminated, thus probably causing loss of ductility. However, contrary to this, A1 sample having a smaller grain size as compared to other films exhibit a decrease in hardness, which means that they have a greater tendency toward plastic deformation i.e., smaller resistance to deformation. The other important mechanical property is the elastic modulus of the material which is related to stiffness. Typically, stiffer materials show higher value of elastic modulus. In our case, film A2 showed a higher value of elastic modulus. The plasticity index (H/E) and resistance to plastic deformation (H^3/E^2) were also important mechanical parameters to calculate the wear resistance and toughness, respectively. A relatively higher value of H/E (0.0378) and H^3/E^2 (0.0103) obtained in A2 film, it indicates that the A2 film has better wear resistance and

toughness as compared to other films which can be due to its higher hardness as a result of numerous grain boundaries which restricts the wearing of the films to a larger extent by acting as barriers to dislocation motion. The indentation induced super elastic depth recovery ratio is obtained from the load–displacement curves as [27]

$$\delta = \frac{h_{max} - h_r}{h_{max}} \dots\dots\dots\dots\dots\dots\dots\dots\dots\dots\dots\dots (3.5)$$

where h_{max} is the penetration depth at maximum load, and h_r is the residual depth when the load returns to zero during unloading. The values of h_{max}, h_r and δ are given in **table 3.4**. The lower the value of h_{max}, the greater the hardness of the film, and the lower the value of h_r, the greater the elasticity of the film. For the film A2, the room temperature depth recovery ratio is higher as compared to the other films.

Sample	Thickness (nm)	Total depth h_{max} (nm)	Residual depth h_r (nm)	Depth recovery ratio (δ)	Hardness H (GPa)	Elastic modulus E (GPa)	H/E	H^3/E^2
A1	90	30.9	12.38	0.599	6.4±1.3	172±2.8	0.0372	0.0088
A2	153	25.4	11.03	0.565	7.2±1.2	190±3.4	0.0378	0.0103
A3	360	41	21.18	0.483	5.5±1.8	146±2.0	0.0376	0.0078
A4	655	70.5	34.73	0.507	3.9±1.1	105±4.1	0.0371	0.0053

Table 3.4. Mechanical properties various thicknesses of Ni–Mn–In films.

3.3.5 Exchange bias behavior

In 1956, Meiklejohn and Bean [28] discovered the exchange bias (EB) effect in ferromagnetic (FM) Co and antiferromagnetic (AFM) CoO system. They discovered a shift in the hysteresis loop from the origin when the system was cooled down to the Neel temperature in the presence of a magnetic field. After discovery of exchange bias, these materials have been extensively studied in many magnetic material systems due to their potential applications in spintronic devices [29], permanent magnets [30] and many other materials [31] etc. The EB phenomenon is mainly attributed to exchange interaction coupling between the FM and AFM interface, resulting into a shift of hysteresis loop, H_{EB}, in presence of magnetic field after cooling through the Neel temperature. The exchange bias behavior has been observed in various systems containing FM–AFM interfaces, such as FM–AFM bilayers [32], FM–AFM heterostructure and multilayer thin films [33-34] and magnetic nano particles [35].

(62)
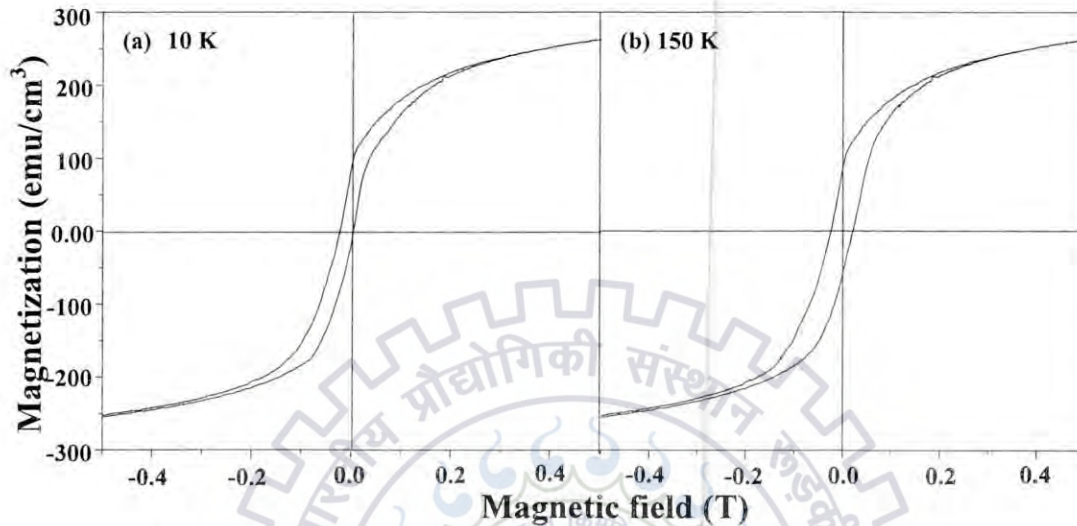
Figure 3.7. M-H loops of A4 film measured at (a) 10 K and (b) 150 K.

The EB behavior of bulk FSMAs especially Ni–Mn-X (X = In, Sn and Sb) has been studied in detail. In order to study the EB behavior in Ni-Mn-In films, we measured the magnetization versus magnetic field (M–H) loops at different temperatures by cooling the films from 330 K down to the required temperature in the presence of an applied field up to ±2 T. Here we measured the EB behavior only in film A4 showing prominent and well-defined martensitic transformation. **Figure 3.7** shows the (M–H) loops of 655 nm thickness film at 10 K and 150 K. For clear visibility of hysteresis loop shift from the origin, the loops are shown only in the low field range -0.5 to 0.5 T. The EB mechanism can be described with regards to an alignment of the AFM spins at the FM–AFM interface parallel toward FM spins occurring during the field cooling procedure. However, for sufficiently large AFM anisotropy in the material, the AFM spins at the interface exert a microscopic torque on the FM spins, which has to overcome of external field. Therefore, it is clear that the hysteresis loop shift is dependent on the strength of AFM anisotropy. If the material is having large AFM anisotropy, the loop shift is also large and if AFM anisotropy is less, we only observe the enhancement of coercivity without loop shifting. The existence of antiferromagnetism in these non-stoichiometric, Mn-rich Ni–Mn–In films is due to the excess Mn (4(a) sites) atoms occupying In (4(b)) sites since the coupling between regular Mn sites is FM while the coupling

(63)

between the Mn and In sites is AFM. Extended X-ray absorption fine structure results show that the distance of Mn–Mn between 4(a) and 4(b) will decrease during martensitic phase transformation from austenite to martensitic [36]. The decrease in the Mn–Mn distance may introduce AFM exchange between each other. That is why the magnetization decreases drastically during martensitic transformation. In our case, the observed EB at 10 K has been attributed to the fact that the FM domains are embedded in AFM matrix and FM–AFM interaction occurs at interface which causes a unidirectional anisotropy. It is clear from **figure 3.7** that the maximum EB of 0.0096 T is found in the film A4 of thickness 655 nm since it possesses higher AFM anisotropy. **Figure 3.8** shows the EB field (H_{EB}) and coercivity (H_C) variation with the temperature.
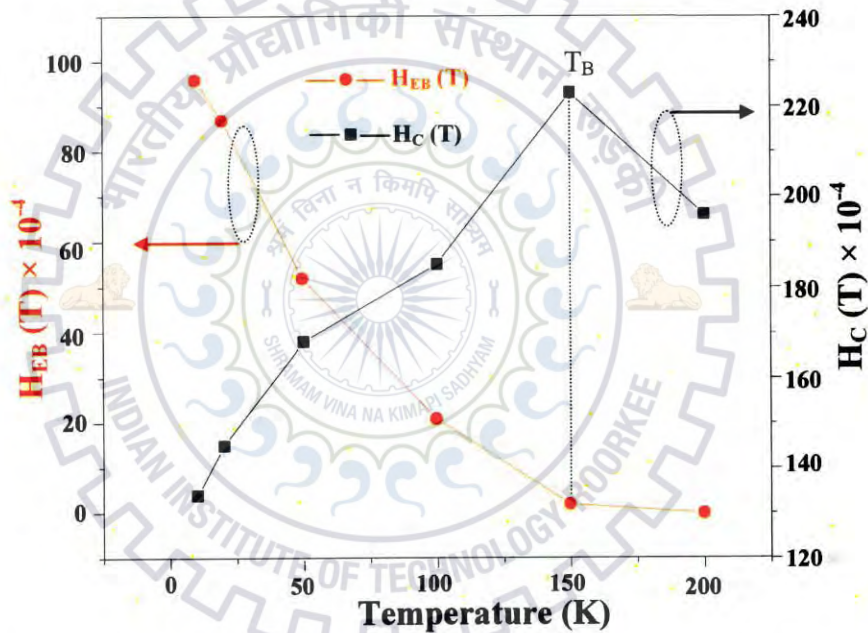
Figure 3.8. The variation of exchange bias (H_{EB}) and coercvity (H_C) with temperature.

The H_{EB} and H_C are defined as;

$$H_{EB} = -(H_{left} + H_{right})/2 \ldots\ldots\ldots\ldots\ldots\ldots\ldots(3.6)$$

and

$$H_C = (H_{left} - H_{right})/2\ldots\ldots\ldots\ldots\ldots\ldots\ldots\ldots(3.7)$$

Here H_{left} and H_{right} are the negative and positive coercive fields at which magnetization vanishes, respectively. The H_{EB} almost linearly decreases with increasing temperature in the low temperature regions and gradually disappears at around blocking temperature (T_B) as indicated in **figure 3.8**. This could be due to a weakening of FM–AFM interface coupling and also decrease of AFM anisotropy with increasing temperature. In addition, the H_C approximately increases with increasing temperature up to T_B and then starts decreasing. This is mainly due to the decrease in AFM anisotropy, as a result of which the FM is able to drag more AFM spins. This behavior provides the existence of an EB effect in the present thin film only when $T < T_B$. A similar behavior was also reported in Ni–Mn-X (X = In, Sn, and Sb) bulk FSMAs [37-38] and bilayer thin films [32]. All of the above results suggest that the occurrence of EB effect is attributed to AFM anisotropy present in the system at lower temperature. At lower T_B, the decrease in H_{EB} with increasing temperature is due to the fact that FM interaction starts to dominate as result FM–AFM interfaces coupling responsible for EB.
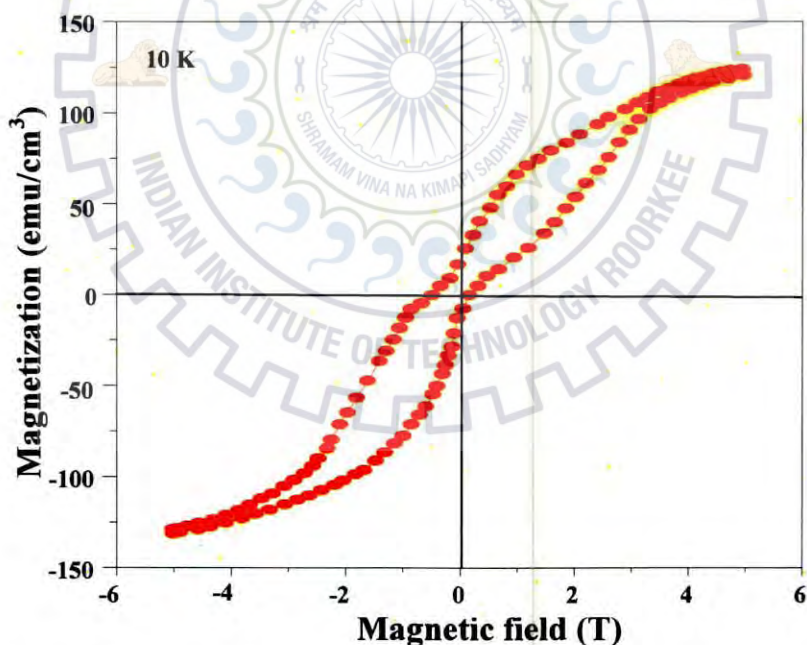
Figure 3.9. Magnetic hysteresis loop obtained for A4 film in ZFC cycle at 10 K.

Further confirming the EB effect in A4 film, we measured the (M–H) loop in zero field cooled (ZFC) mode as shown in **figure 3.9**. The ZFC hysteresis loop showed a double shift due to

existence of EB effect in film. Usually, when a system is cooled under absence of field, EB materials show double shifted loops. In ZFC process, the AFM regions are locally oriented in the opposite direction and divided into two types of regions. During magnetization measurement, these two types of regions are coupled in an opposite direction to the FM regions, as a result the double shifted hysteresis loop occurs [39].

3.3.6 Magnetocaloric effect

In recent years, the magnetocaloric effect (MCE) phenomenon is extensively used in a magnetic refrigeration process due to its more potential applications in refrigeration technology as compared to conventional compressor type refrigerators. In magnetic materials, MCE is measured by the change in magnetic entropy (ΔS_M) or adiabatic temperature change (ΔT) on application of magnetic field. An entropy change can be induced by either structural or magnetic phase transformations due to difference in magnetization between the initial and final phases. Several magnetic material systems, such as Gd–Si–Ge [40], Mn–As–Sb [41], La–Fe–Si [42], Fe–Mn–As [43] and DySb [44] only possess a conventional MCE as a result of second order magnetic transformation. In these systems, the sign of isothermal magnetic entropy was negative. The family of FSMAs, such as Ni–Mn–Ga, Ni–Mn-X (X = Sn, Sb and In) have been found to be potential candidates for both conventional and inverse MCE [45-47]. In these alloys, the MCE is higher than the rare-earth based compounds and also less expensive raw materials are used. This makes these alloys potential materials to be used in environmental friendly magnetic refrigeration applications. To the best of our knowledge, there is no report on the MCE in Ni–Mn–In FSMA alloy thin film.

In the present investigation, we report the MCE in A4 film (showing prominent thermal hysteresis between FC and FH curve). As a way to study the MCE, the isothermal magnetization (M–H) measurements were performed by applying magnetic field from 0 to 2 T with a temperature step of ΔT = 3 K. **Figure 3.10** shows the isothermal (M–H) curves for A4 film, within the martensitic transformation temperature region. The measurements were carried out by cooling the film from 330 K down to the required temperature and then varying field from 0 to 2 T. The A4 film has shown a ferromagnetic behavior within the martensitic temperature region from 281 K to 293 K. The magnetic entropy change (ΔS_M) was measured from isothermal magnetization curves using the Maxwell relation [48].

$$\Delta S_M\left(T,H\right) = \int_0^H \left| \frac{\partial M(T,H)}{\partial T} \right|_H dH \quad ....(3.8)$$

(66)

Since we used a constant temperature interval, equation (3.8) can be written as

$$\Delta S_M \approx \frac{1}{\Delta T}\left[\int_0^H \left(M(T+\Delta T, H) - M(T, H)\right)dH\right] \ldots\ldots\ldots\ldots\ldots\ldots(3.9)$$

The sign of ΔS_M is determined by the sign of $\frac{\partial M}{\partial T}$ as shown in **equation (3.8)**. Many authors used **equation (3.8)** and they reported the positive values of entropy change ΔS_M in first order phase transformations of Ni–Mn based FSMA systems [49]. The temperature dependence of ΔS_M was estimated with a maximum field change equal to 2 T and depicted in **figure 3.11**. As temperature
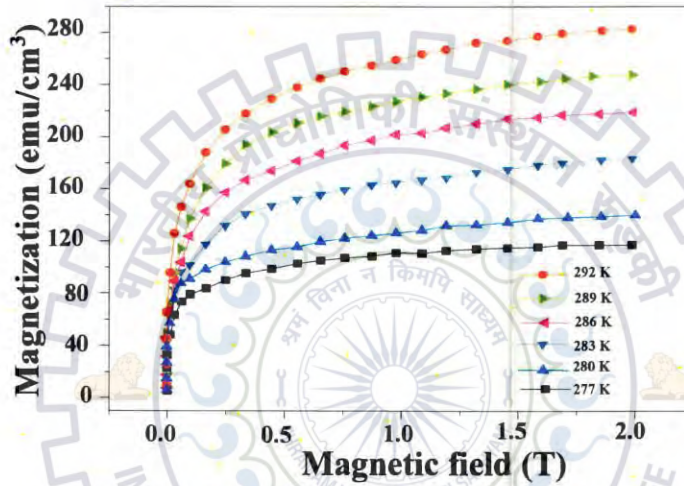
Figure 3.10. Isothermal M–H curves obtained in A4 film around the martensitic transformation temperature.

increases, the ΔS_M also increases of the film and reaches to maximum value at martensitic transition temperature. Such a positive sign of ΔS_M was attributed to the inverse MCE [50]. The entropy change $\Delta S_M = 15.2$ mJ/cm^3 K (**Table 3.3**) was measured only in A4 (thickness = 655 nm) film. This is mainly due to more prominent first order structural transition and higher value of $\frac{\partial M}{\partial T}$ in A4 film. For this film, both the crystal and magnetic structures are different from the original phase during martensitic phase transformation in an applied field. This gives rise to a MCE due to a strong magneto crystalline coupling. Another important parameter for magnetocaloric materials is the refrigeration capacity (RC) which is a direct measure of the heat transferred from the cold reservoir to the hot reservoir in a refrigeration cycle [52]. It is defined as,

$$RC = \int_{T_{cold}}^{T_{hot}} \Delta S_M (T)dT \ldots\ldots\ldots\ldots\ldots\ldots\ldots(3.10)$$

(67)

where T_{cold} and T_{hot} are the temperatures of the cold and hot reservoir of the refrigeration cycle. The material with higher refrigerant capacity value is needed to transport greater amount of heat in a refrigeration cycle. Here, the RC value is defined by the full width at half maximum of the ΔS_M peak. In the present work, we used temperature interval 277 K to 292 K for A4 film to calculate the RC value. The RC value derived for this film is 155.04 mJ/cm^3, listed in **table 3.3**. The A4 film has shown the maximum RC value. This is mainly due to its wide temperature span of ΔS_M. The obtained results are very promising for micro length scale magnetic refrigeration applications.
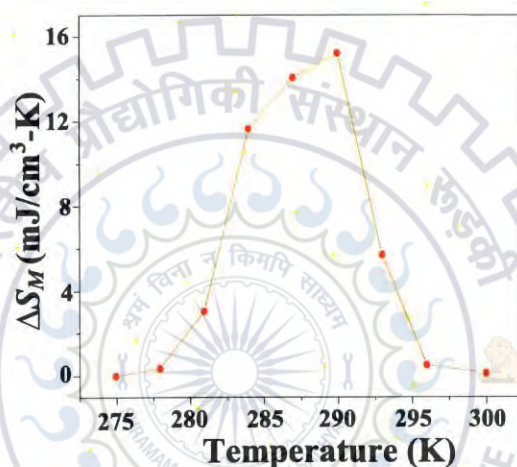
Figure 3.11. Magnetic entropy change ΔS_M versus temperature for A4 film in a field of 2 T.

3.4 Conclusions

In conclusion, we have systematically studied the thickness dependent structural, magnetic, electrical and mechanical properties of Ni–Mn–In in-situ FSMA thin films successfully grown on Si (100) substrate. X-ray diffraction results reveal that all the films have shown austenitic cubic L2$_1$ structure at room temperature. Temperature dependent magnetic and electrical resistance measurements have shown that the martensitic phase transformation temperatures are increased with increasing thickness and lower thickness of film (90 nm) has not shown any phase transformation behavior. The field dependent magnetization curves show that the saturation magnetization (S$_M$) increases with increasing thickness in addition to the 655 nm film showed higher saturation magnetization 283 emu/cm^3. Further, nanoindentation studies revealed that the

higher values of hardness (7.2 GPa) and elastic modulus (190 GPa) occurred in the A2 film with thickness of 153 nm. In A4 film with thickness of 655 nm, we observed an exchange bias of 0.0096 T and higher magnetization with smaller thermal hysteresis width. Nevertheless, from the study of isothermal magnetization curves we found the magnetic entropy change ΔS_M = 15.2 mJ/cm^3 K (field 2 T) at martensitic transition temperature in 655 nm film, which is associated with the first order martensitic phase transformation. The refrigeration capacity (RC = 155.04 mJ/cm^3) was also calculated for this film.

3.5 References

[1]   Ullakko K., Huang J. K., Kantner C., O'Handley R. C., Kokorin V. V., "Large magnetic-field-induced strains in Ni$_2$MnGa single crystals," *Appl. Phys. Lett.*, **69**, 1966 (1996).

[2]   Pathak A. K., Khan M., Dubenko I., Stadler S., Ali N., "Large magnetic entropy change in Ni$_{50}$Mn$_{50-x}$In$_x$ Heusler alloys," *Appl. Phys. Lett.*, **90**, 262504 (2007).

[3]   Pathak A. K., Gautam B. R., Dubenko I., Khan M., Stadler S., Ali N., "Phase transitions and magnetoresistance in Ni$_{50}$Mn$_{50-x}$In$_x$ Heusler alloys," *J. Appl. Phys.*, **103**, 07F315 (2008).

[4]   Sharma V. K., Chattopadhyay M. K., Chouhan A., Roy S. B., "Temperature and magnetic field induced strain in Ni$_{50}$Mn$_{34}$In$_{16}$ alloy," *J. Phys. D. Appl. Phys.*, **42**, 185005 (2009).

[5]   Heczko O., Straka L., "Temperature dependence and temperature limits of magnetic shape memory effect," *J. Appl. Phys.*, **94**, 7139 (2003).

[6]   Wang B. M., Liu Y., Xia B., Ren P., Wang L., "Large exchange bias obtainable through zero-field cooling from an unmagnetized state in Ni-Mn-Sn alloys," *J. Appl. Phys.*, **111**, 043912 (2012).

[7]   Krenke T., Acet M., Wassermann E., Moya X., Mañosa L., Planes A., "Ferromagnetism in the austenitic and martensitic states of Ni-Mn-In alloys," *Phys. Rev. B*, **73**, 174413 (2006).

[8]   Miyamoto T., Ito W., Umetsu R. Y., Kainuma R., Kanomata T., Ishida K., "Phase stability and magnetic properties of Ni$_{50}$Mn$_{50-x}$In$_x$ Heusler-type alloys," *Scr. Mater.*, **62**, 151 (2010).

[9]   Chatterjee S., Singh V. R., Deb A. K., Giri S., De S. K., Dasgupta I., Majumdar S., "Magnetic properties of Heusler alloys: Theory and experiment," *J. Magn. Magn. Mater.*, **322**, 102 (2010).

[10]   Bhobe P. A., Priolkar K. R., Nigam A. K., "Room temperature magnetocaloric effect in Ni-Mn-In," *Appl. Phys. Lett.*, **91**, 242503 (2007).

[11]   Feng Y., Sui J. H., Gao Z. Y., Zhang J., Cai W., "Investigation on martensitic transformation behavior, microstructures and mechanical properties of Fe-doped Ni–Mn–In alloys," *Mater. Sci. Eng. A*, **507**, 174 (2009).

[12]   Sharma V. K., Chattopadhyay M. K., Khandelwal A., Roy S. B., "Martensitic transition near room temperature and the temperature- and magnetic-field-induced multifunctional properties of Ni$_{49}$CuMn$_{34}$In$_{16}$ alloy," *Phys. Rev. B*, **82**, 172411 (2010).

[13]   Sánchez-Alarcos V., Recarte V., Pérez-Landazábal J. I., Chapelon J. R., Rodríguez-Velamazán J. A., "Structural and magnetic properties of Cr-doped Ni–Mn–In metamagnetic shape memory alloys," *J. Phys. D. Appl. Phys.*, **39**, 395001 (2011).

[14] Bhattacharya K., James R. D., "A theory of thin films of martensitic materials with applications to microactuators," *J. Mech. Phys. Solids*, **47**, 531 (1999).

[15] Sokolov A., Zhang L., Dubenko I., Samanta T., Stadler S., Ali N., "Evidence of martensitic phase transitions in magnetic Ni-Mn-In thin films," *Appl. Phys. Lett.*, **102**, 2013 (2013).

[16] Niemann R., Schultz L., Fähler S., "Growth of sputter-deposited metamagnetic epitaxial Ni-Co-Mn-In films," *J. Appl. Phys.*, **111**, 093909 (2012).

[17] Banerjee R., Sperling E. A., Thompson G. B., Fraser H. L., Bose S., Ayyub P., "Lattice expansion in nanocrystalline niobium thin films," *Appl. Phys. Lett.*, **82**, 4250 (2003).

[18] Siegel R.W., in: Cahn R.W., Haasen P., Kramer (Eds) E. J., *1019 Processing of Metals and Alloys*, VCH, Weinheim, pp. 583 (1991).

[19] Kumar D., Kaur D., "Structural and magnetic properties of La_2NiMnO_6 thin films on $LaAlO_3$ substrate with varying thickness," *J. Alloys Compd.*, **554**, 277 (2013).

[20] Zhang H. S., Endrino J. L., Anders A., "Comparative surface and nano-tribological characteristics of nanocomposite diamond-like carbon thin films doped by silver," *Appl. Surf. Sci.*, **255**, 2551 (2008).

[21] Choudhary N., Kharat D. K., Kaur D., "Structural, electrical and mechanical properties of magnetron sputtered $NiTi/PZT/TiO_x$ thin film heterostructures," *Surf. Coatings Technol.*, **205**, 3387 (2011).

[22] Vishnoi R., Singhal R., Kaur D., "Thickness dependent phase transformation of magnetron-sputtered Ni–Mn–Sn ferromagnetic shape memory alloy thin films," *J. Nanoparticle Res.*, **13**, 3975 (2011).

[23] Bhobe P. A., Priolkar K. R., Sarode P. R., "Local atomic arrangement and martensitic transformation in $Ni_{50}Mn_{35}In_{15}$: An EXAFS Study," *J. Phys. D. Appl. Phys.*, **41**, 045004 (2007).

[24] Liu Y., Huang X., "Substrate-induced stress and transformation characteristics of a deposited Ti–Ni–Cu thin film," *Philos. Mag.*, **84**, 1919 (2004).

[25] Vishnoi R., Singhal R., Asokan K., Kanjilal D., Kaur D., "Ion irradiation induced modifications of nanostructured Ni-Mn-Sn ferromagnetic shape memory alloy thin films," *Thin Solid Films*, **520**, 1631 (2011).

[26] Oliver W. C., Pharr G. M., "Measurement of hardness and elastic modulus by instrumented indentation: Advances in understanding and refinements to methodology," *J. Mater. Res.*, **19**, 3 (2004).

[27] Ni W., Cheng Y.T., Grummon D. S., "Microscopic superelastic behavior of a nickel-titanium alloy under complex loading conditions," *Appl. Phys. Lett.*, **82**, 2811 (2003).

[28] Meikeljohn W. H., Bean C. P., "New Magnetic Anisotropy," *Phys. Rev.*, **102**, 1413 (1956).

[29] Kools J. C. S., "Exchange-biased spin-valves for magnetic storage," *IEEE Trans. Magn.*, **32**, 3165 (1996).

[30] Nogués J., Sort J., Langlais V., Skumryev V., Suriñach S., Muñoz J. S., Baró M. D., "Exchange bias in nanostructures," *Phys. Rep.*, **422**, 65 (2005).

[31] Nogués J., Schuller I. K., "Exchange bias," *J. Magn. Magn. Mater.*, **192**, 203 (1999).

[32] Hu Y., Wu G. Z., Liu Y., Du A., "Relative-thickness dependence of exchange bias in bilayers and trilayers," *J. Magn. Magn. Mater.*, **324**, 3204 (2012).

[33] Hochstrat A., Binek C., Kleemann W., "Training of the exchange-bias effect in NiO-Fe heterostructures," *Phys. Rev. B*, **66**, 1 (2002).

[34] Kumar D., Kaur D., "Exchange biasing in SFMO/SFWO double perovskite multilayer thin films," *J. Alloys Compd.*, **509**, 7886 (2011).

[35] Gangopadhyay S., Hadjipanayis G. C., Sorensen C. M., Klabunde K. J., "Exchange anisotropy in oxide passivated Co fine particles," *J. Appl. Phys.*, **73**, 6964 (1993).

[36] Bhobe P. A., Priolkar K. R., Sarode P. R., "Factors influencing the martensitic transformation in $Ni_{50}Mn_{35}Sn_{15}$: an EXAFS study," *J. Phys. Condens. Matter*, **20**, 015219 (2008).

[37] Khan M., Dubenko I., Stadler S., Ali N., "Exchange bias behavior in Ni-Mn-Sb Heusler alloys," *Appl. Phys. Lett.*, **91**, 48 (2007).

[38] Pathak A. K., Khan M., Gautam B. R., Stadler S., Dubenko I., Ali N., "Exchange bias in bulk Ni-Mn-In-based Heusler alloys," *J. Magn. Magn. Mater.*, **321**, 963 (2009).

[39] Vishnoi R., Kaur D., "Exchange bias behaviour in magnetron sputtered $Ni_{49.8}Mn_{36.1}Sn_{13.9}$ ferromagnetic shape memory alloy thin film," *J. Alloys Compd.*, **509**, 2833 (2011).

[40] Pecharsky V. K.,. Gschneidner, Jr. K. A, "Giant Magnetocaloric Effect in $Gd_5(Si_2 Ge_2)$," *Phys. Rev. Lett.*, **78**, 4494 (1997).

[41] Wada H., Tanabe Y., "Giant magnetocaloric effect of $MnAs_{1-x}Sb_x$," *Appl. Phys. Lett.*, **79**, 3302 (2001).

[42]   Hu F. X., Shen B. G., Sun J. R., Cheng Z. H., Rao G. H., Zhang X. X., "Influence of negative lattice expansion and metamagnetic transition on magnetic entropy change in the compound LaFe$_{11.4}$Si$_{1.6}$," *Appl. Phys. Lett.*, **78**, 3675 (2001).

[43]   Sun N. K., Ma S., Zhang Q., Du J., Zhang Z. D., "Large room-temperature magnetocaloric effects in Fe$_{0.8}$ Mn$_{1.5}$ As," *Appl. Phys. Lett.*, **91**, 2013 (2007).

[44]   Hu W. J., Du J., Li B., Zhang Q., Zhang Z. D., "Giant magnetocaloric effect in the Ising antiferromagnet DySb," *Appl. Phys. Lett.*, **92**, 90 (2008).

[45]   Huang C., Wang Y., Tang Z., Liao X., Yang S., Song X., "Influence of atomic ordering on elastocaloric and magnetocaloric effects of a Ni–Cu–Mn–Ga ferromagnetic shape memory alloy," *J. Alloys Compd.*, **630**, 244 (2015).

[46]   Jing C., Chen J., Li Z., Qiao Y., Kang B., Cao S., Zhang J., "Exchange bias behavior and inverse magnetocaloric effect in Ni$_{50}$Mn$_{35}$In$_{15}$ Heusler alloy," *J. Alloys Compd.*, **475**, 1 (2009).

[47]   Varzaneh A. G., Kameli P., Karimzadeh F., Aslibeiki B., Varvaro G., Salamati H., "Magnetocaloric effect in Ni$_{47}$Mn$_{40}$Sn$_{13}$ alloy prepared by mechanical alloying," *J. Alloys Compd.*, **598**, 6 (2014).

[48]   Krenke T., Duman E., Acet M., Wassermann E. F., Moya X., Mañosa L., Planes A., Suard E., Ouladdiaf B., "Magnetic superelasticity and inverse magnetocaloric effect in Ni-Mn-In," *Phys. Rev. B*, **75**, 104414 (2007).

[49]   Nayak A. K., Suresh K. G., Nigam A. K., "Giant inverse magnetocaloric effect near room temperature in Co substituted NiMnSb Heusler alloys," *J. Phys. D. Appl. Phys.*, **42**, 035009 (2010).

[50]   Phan T. L., Zhang P., Dan N. H., Yen N. H., Thanh P. T., Thanh T. D., Phan M. H., Yu S. C., "Coexistence of conventional and inverse magnetocaloric effects and critical behaviors in Ni$_{50}$Mn$_{50-x}$Sn$_x$ (x = 13 and 14) alloy ribbons," *Appl. Phys. Lett.*, **101**, 212403 (2012).

[51]   Han Z. D., Wang D. H., Zhang C. L., Tang S. L., Gu B. X., Du Y. W., "Large magnetic entropy changes in the Ni$_{45.4}$Mn$_{41.5}$In$_{13.1}$ ferromagnetic shape memory alloy," *Appl. Phys. Lett.*, **89**, (182507) 2006.

[52]   Sharma V. K., Chattopadhyay M. K., Kumar R., Ganguli T., Tiwari P., Roy S. B., "Magnetocaloric effect in Heusler alloys Ni$_{50}$Mn$_{34}$In$_{16}$ and Ni$_{50}$ Mn$_{34}$Sn$_{16}$," *J. Phys. Condens. Matter*, **19**, 496207 (2007).

Chapter 4

Growth and Characterization of Ni-Mn-Sb-Al and Ni-Mn-In-Cr FSMA Thin Films

CHAPTER 4

GROWTH AND CHARECTERIZATION OF Ni-Mn-Sb-Al AND Ni-Mn-In-Cr FSMA THIN FILMS

4.1 **Martensitic phase transformation and magnetocaloric effect in Al co-sputtered Ni-Mn-Sb alloy thin films**

    4.1.1   **Introduction**

    4.1.2   **Experimental details**

    4.1.3   **Results and discussion**

            4.1.3.1   Structural properties

            4.1.3.2   Magnetic properties

            4.1.3.3   Electrical properties

            4.1.3.4   Magnetocaloric effect

    4.1.4   **Conclusion**

4.2 **Ni-Mn-In-Cr ferromagnetic shape memory alloy thin films**

    4.2.1   **Introduction**

    4.2.2   **Experimental details**

    4.2.3   **Results and discussion**

            4.2.3.1   Structural properties

            4.2.3.2   Magnetic properties

            4.2.3.3   Electrical properties

            4.2.3.4   Magnetocaloric effect

            4.2.3.5   Mechanical properties

    4.2.4   **Conclusion**

4.3   **References**

4.1 Martensitic phase transformation and magnetocaloric effect in Al co-sputtered Ni-Mn-Sb alloy thin films

4.1.1 Introduction

In recent years, considerable attention has been drawn from the scientific community and industry on the development of magnetic materials that exhibit a large magnetocaloric effect (MCE) near room temperature [1-2]. The magnetocaloric effect (MCE) is an attracted phenomenon in which a magnetic material exhibits an adiabatic temperature change or an entropy change when subjected to a variation in the magnetic field [3]. The materials exhibiting MCE effect are finding potential applications in the newly emerging area of environmental friendly refrigeration technology [4]. They are manifold efficient than the conventional compression/expansion type refrigerants where a large amount of energy is consumed and the liquid chemicals used as refrigerants are exposed to the environment causing threats to ozone layer and are responsible for several health hazards [3]. There are numerous reports based on rare earth materials showing a large MCE [5-6]. Hughes et al. [7] developed magnetic refrigerators with gadolinium as a refrigerant and showed a high efficiency up to 60% which is better than any of the conventional refrigerators. Talik et al. [8] observed a giant magnetocaloric effect in Tb_3Rh at different applied fields. In addition to these conventional magnetic materials [9-11], a large inverse MCE has been observed in the family of ferromagnetic shape memory alloys such as Ni-Mn-Ga [12-13] and Ni-Mn-X (X= Sn, Sb and In) [14-15]. As a consequence, these alloys display several other interesting properties like shape memory effect [16], large magnetoresistance (MR) [17], and large magnetic field induced strain in the vicinity of the martensitic transformations [15]. Khan et al. [18] showed a maximum positive magnetic entropy change of $\Delta S_M \approx 19$ J /kg K at approximately 297 K for a magnetic field change of 5 T. Feng et al. [19] found the large reversible magnetic entropy change of $\Delta S_M = 5.21$ J/kg K at 347 K in $Ni_{49}Mn_{39}Sb_{12}$ alloy. Apart from monolithic FSMA materials, several dopants like B, Cu and Co were added to further improve their magnetocaloric properties [20-22]. $Ni_{50-x}Co_xMn_{38}Sb_{12}$ alloy system produced by Nayak et al. [23] showed a maximum MCE value of 34 J/kg K in 50 kOe. Similarly a very high magnetic entropy change of 14.2 J/kg K was observed in $Ni_{50}Mn_{36}Fe_2Sb_{12}$ at 288 K for 50 kOe. Such properties for bulk FSMA exhibit a great perspective for multifunctional applications of these materials [24].

With the advent of micro and nanoscale electronic devices, miniaturization of the cooling techniques for Micro-Electro-Mechanical-Systems (MEMS) applications are required. Nevertheless, the knowledge on their thin behavior is still sparse. The magnetic field required to enable the MCE in bulk FSMAs is more than 2T. And such a large magnetic field is undesirable for MEMS structures because it can interfere with the electronics of the device, reducing its performance and a significant power is also required to generate such high fields. It is therefore imperative to study and develop MCE in FSMA thin films to test their viability for microscale refrigeration systems. On the other hand, investigating the magnetocaloric effect and associated materials at nanoscale is still a novel effort. Hence, in the present study, we investigated the influence of Al doping on magnetic and magnetocaloric properties of Ni-Mn-Sb FSMA thin films in detail. This study is useful for micro-length-scale magnetic refrigeration technology.

4.1.2 Experimental details

The Ni-Mn-Sb-Al thin films were deposited by co-sputtering of $Ni_{50}Mn_{37}Sb_{13}$ and Al targets onto Si (100) substrates at 823 K substrate temperature. The substrates were initially cleaned thoroughly in an ultrasonic bath using a combination of distilled water and trichloroethylene in 4:1 ratio followed by washing in boiled acetone. Experimental procedure is given in **section 3.1.2** and sputtering parameters are summarized in **table 4.1.** The composition of the films was determined by energy dispersive X-ray analysis (EDAX) and films with composition $Ni_{49.9}Mn_{37.4}Sb_{12.7}$, $Ni_{49.8}Mn_{36.28}Sb_{12.8}Al_{1.12}$, $Ni_{49.9}Mn_{35.1}Sb_{12.7}Al_{2.3}$ and $N_{49.8}Mn_{32.97}Sb_{12.8}Al_{4.43}$ are represented by S0, S1, S2 and S3, respectively. The crystallographic orientations of the deposited films were studied using Bruker advanced diffractrometer of Cu Kα (1.54Å) radiations in θ–2θ geometry at a scan speed of 1°/min. The magnetic properties were studied with a vibrating sample magnetometer (VSM). The magnetic field dependence magnetization loops (M-H) of the films were recorded at various temperatures with magnetic fields up to 2 T. To further characterize the magnetic properties, the temperature dependence magnetization (M-T) of the films was measured by varying temperatures range from 10 K to 350 K under field cooled (FC) and field heating (FH) cycles. The measurement in FC cycle was taken by first cooling the film from 350 K to 10 K in the presence of field and the data was recorded. Finally, the temperature was increased to 350 K in the presence of field and measurements were obtained in FH cycle. The resistance verses temperature (R-T) measurements were performed by four-probe resistivity method in the temperature range from 100 K to 350 K. The magnetic

entropy change, ΔS_M, was calculated from the isothermal magnetic data using the Maxwell relation.

Deposition Process	Magnetron sputtering
Target	$Ni_{50}Mn_{37}Sb_{13}$, Al
Base pressure	$\leq 2 \times 10^{-6}$ Torr
Gas used	Argon
Sputtering pressure	10 mTorr
Deposition time	15 minutes
Sputtering power	$Ni_{50}Mn_{37}Sb_{13}$:100 W, Al: 10-20W
Substrate	Silicon (100)
Substrate temperature	823 K
Substrate to Target distance	5 cm

Table 4.1. Sputtering parameters for Ni-Mn-Sb-Al thin films.

4.1.3 Results and discussion

4.1.3.1 Structural properties

Figure 4.1 **(a)** shows X-ray diffraction (XRD) pattern of S0, S1, S2 and S3 films at room temperature. The high symmetric austenitic cubic $L2_1$ structure (space group *Fm3m*) can be indexed as the main phase in the films S0 and S1 and the corresponding lattice parameters were a = 0.5927 nm and 0.5841 nm, respectively. However, the film S3 showed only low-symmetric martensitic phase at room temperature, which can be indexed to an orthorhombic structure (space group *Pmm2*, a = 0.608 nm, b = 0.5578 nm and c = 0.5751 nm). Both austenitic and martensitic phases were found in the film S2 at room temperature. **Figure 4.1 (b)** shows the decrease of unit cell volume with increasing Al content. This could be attributed to the fact that the atomic radius of Al (121 pm) is smaller than that of Mn (132 pm). The lattice parameter and unit cell volume values of all the films are listed in **table 4.2**. **Figure 4.2 (a)-(d)** shows the typical EDAX spectrum of S0, S1, S2 and S3 films. The composition of the Ni-Mn-Sb film greatly varied with the concentration of Al. An increasing Al content brings slight changes in the Ni, Sb concentration, however there was an appreciable change in the Mn concentration of Ni-Mn-Sb-Al thin films.
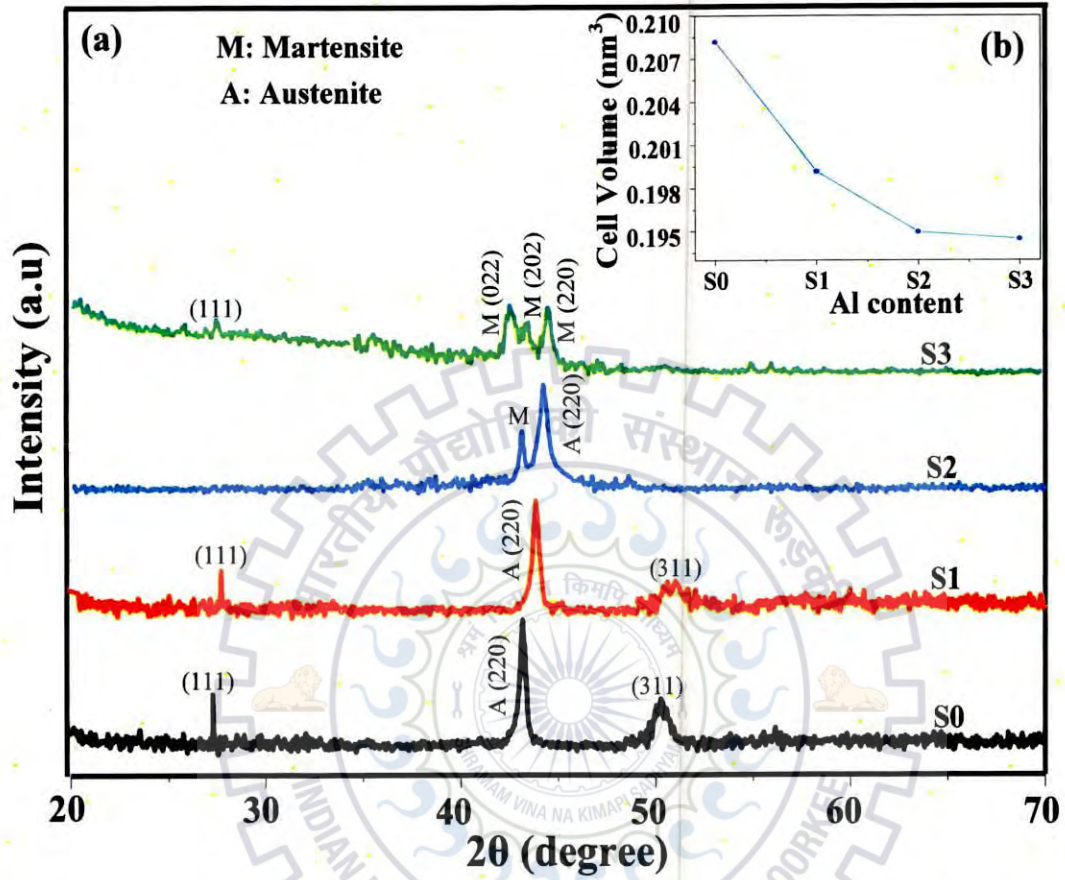
Figure 4.1. (a) The XRD pattern of $Ni_{49.9}Mn_{37.4}Sb_{12.7}$ (S0), $Ni_{49.8}Mn_{36.28}Sb_{12.8}Al_{1.12}$ (S1), $Ni_{49.9}Mn_{35.1}Sb_{12.7}Al_{2.3}$ (S2) and $N_{49.8}Mn_{32.97}Sb_{12.8}Al_{4.43}$ (S3) samples at room temperature (b) unit cell volume versus Al content.
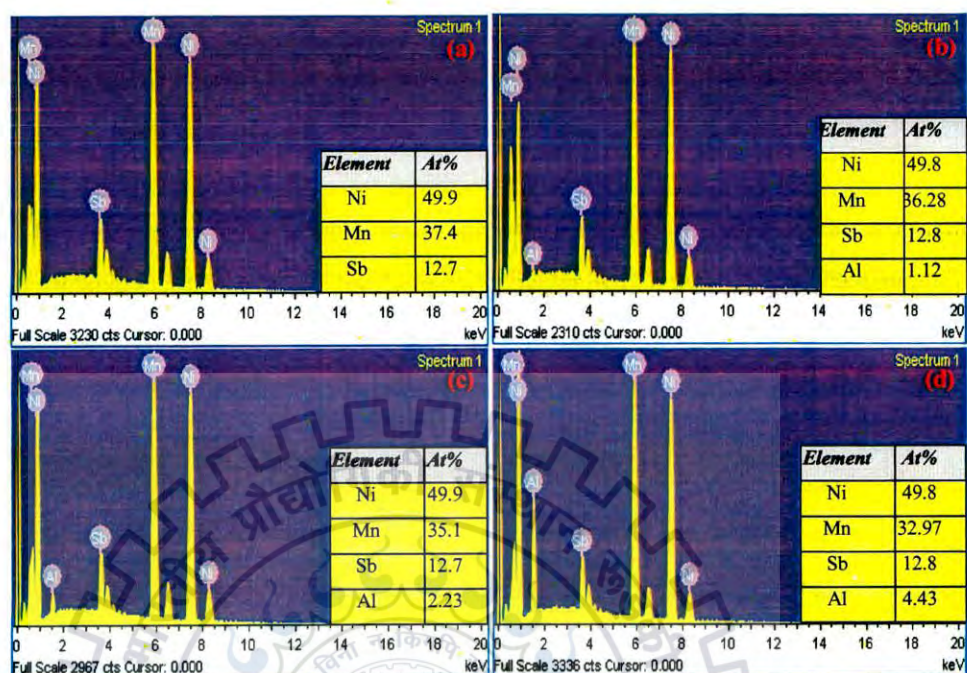
Figure 4.2. EDAX spectrum of (a)-$Ni_{49.9}Mn_{37.4}Sb_{12.7}$ (S0), (b)-$Ni_{49.8}Mn_{36.28}Sb_{12.8}Al_{1.12}$ (S1), (c)-$Ni_{49.9}Mn_{35.1}Sb_{12.7}Al_{2.3}$ (S2) and (d)-$N_{49.8}Mn_{32.97}Sb_{12.8} Al_{4.43}$ (S3) films.

4.1.3.2 Magnetic properties

In order to understand the effect of Al addition on magnetic and magnetocaloric properties of Ni-Mn-Sb alloy thin films, magnetization was recorded as a function of temperature (M-T) for films S0-S3, at a magnetic field of 0.02T as shown in **figure 4.3 (a)-(d)**. It is clear from the (M-T) curves that all the films undergo a ferromagnetic (FM) to paramagnetic (PM) transition during the field heating (FH) cycle. The temperature at which this transition takes place is called Curie temperature (T_C^A) of austenitic phase. The Curie temperature (T_C^A) was found approximately constant for all the films and the values are reported in **table 4.2**. The Curie temperature in our films is also in well agreement with the previously reported values for bulk Ni-Mn-Sb alloys **[15, 18]**. During the field cooled (FC) cycle of the (M-T) curve (below T_C^A), the magnetization first increases to a maximum value and thereafter, a sharp decrease was observed with further decrease in temperature. The corresponding maximum and minimum temperatures for this martensitic transition are called the martensitic start (M_s) and martensitic finish (M_f) temperatures, respectively. Temperature corresponding to the martensitic transition (T_M) is

defined as the mean of the M_s and M_f temperatures, i,e., $(M_s+M_f)/2$. It is to be noted that with decreasing temperature below M_s, the austenitic cubic phase temporarily gets converted into the mixed austenitic-martensitic phase where the magnetization decreases to the minimum value. An abrupt decrease in magnetization across the martensitic transition could be attributed to the change in exchange interaction that arises because of the coexistence of different lattice parameters of austenitic and martensitic phases. This is not surprising because the inter-atomic distances between the Mn-Mn atoms within the unit cell are different for the austenitic and martensitic lattices. Although these distances, to a large degree, determine the spin exchange interactions responsible for the magnetic ordering [25]. Similarly, the reverse martenisitc transformation occurring on field heating (FH) defines the austenitic start (A_s) and austenitic finish (A_f) temperatures. It is noted that, the FH curve does not retrace the FC curve and a thermal hysteresis width was observed in all films. The presence of this thermal hysteresis indicates the presence of first-order structural transition [26]. On the other hand, the absence of thermal hysteresis near T_C^A indicates a second order magnetic transition from FM to PM state. The values of different characteristic temperatures defining the austenitic-martensitic transformation temperatures (M_s, M_f, A_s, A_f and T_C^A) and corresponding hysteresis widths (ΔT) for all films are depicted in **table 4.2**. A slight deviation in the characteristic transition temperatures observed in our films as compared to bulk Ni-Mn-Sb alloy could be attributed to the strain effects present in the thin films. The strain effects in thin films might originate from the lattice misfit present between the film and the substrate that result in the change of the physical properties of the films. It has been previously reported that the stress present between the substrate and magnetron sputtered FSMA thin films strongly affects the martensitic phase transformation characteristics [27]. However, the (M-T) behavior (**figure 4.3 (b)-(d)**) in Al-doped Ni-Mn-Sb films were similar to pure Ni-Mn-Sb film, but the martensitic transformation temperatures (T_M) were shifted towards higher temperatures. A monotonic increase in the martensitic transformation temperatures with increasing Al concentration could be easily seen in the **table 4.2**. It has been reported in Ni-Mn-X (X = Sn, In and Sb) FSMAs that the T_M increases with an increase in the value of valence electron concentration (e/a) [21] and decrease of unit cell volume [26]. In addition, the hybridization between the Ni atoms and the Mn atoms on the X sites is also an important driving force for the martensitic transformation in Mn-rich Ni-Mn-X FSMAs [21, 25].
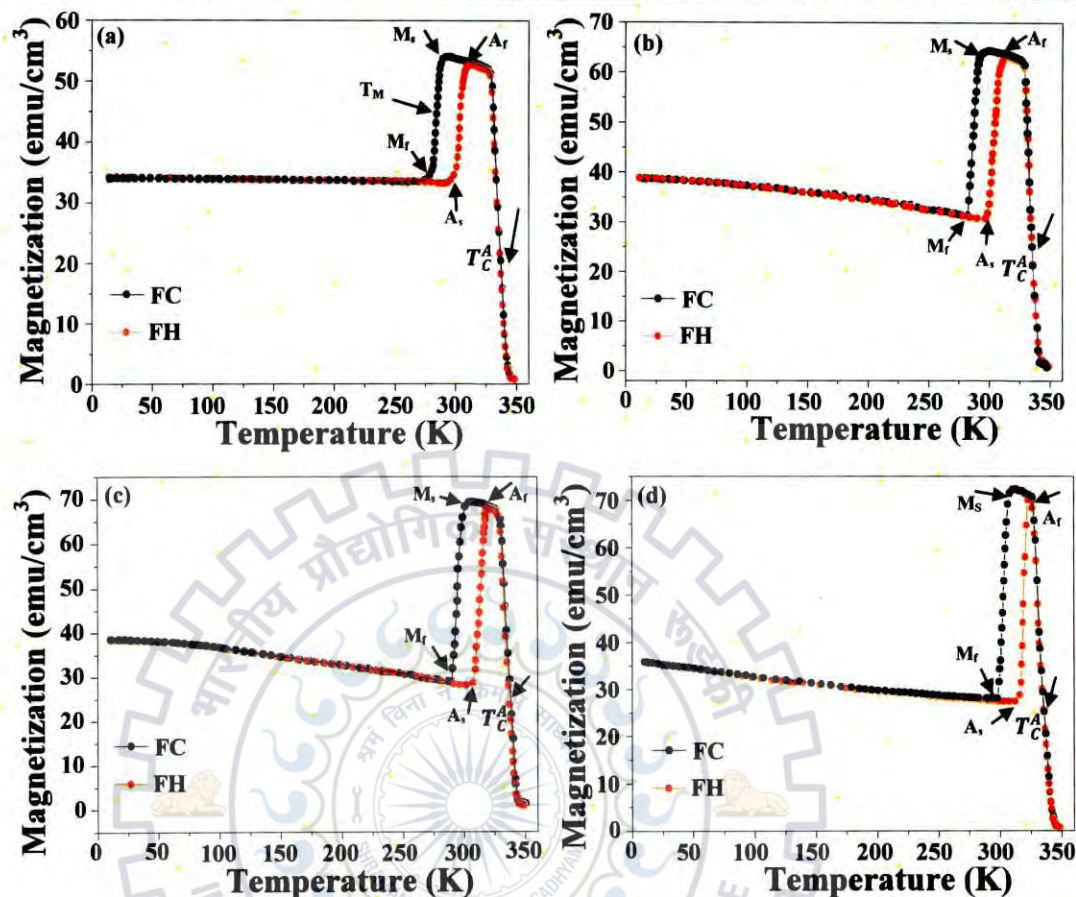
Figure 4.3. Magnetization versus temperature (M-T) curves obtained for (a)-$Ni_{49.9}Mn_{37.4}Sb_{12.7}$ (S0), (b)-$Ni_{49.8}Mn_{36.28}Sb_{12.8}Al_{1.12}$ (S1), (c)-$Ni_{49.9}Mn_{35.1}Sb_{12.7}Al_{2.3}$ (S2) and (d)-$N_{49.8}Mn_{32.97}Sb_{12.8}Al_{4.43}$ (S3) films.

While using the extended x-ray absorption fine structure (EXAFS) studies and first-principles calculations of Ni-Mn-In full Heusler alloys, it has also been suggested that the Ni-Mn hybridization may be responsible for the magnetic properties [28]. In such cases, once the Ni-Mn hybridization is established, any change in the Ni or Mn concentration will weaken the hybridization, leading to the shift of martensitic transformation. Despite the fact that several reports show that this can be the case, in order to confirm that Ni-Mn hybridization is the main factor that determines the shift of martensitic transformation temperature rather than e/a [29]. Roy *et al.* [30] demonstrated that the partial replacement of Mn by Cu in $Ni_2Mn_{0.75}Cu_{0.25}Ga$ enhanced the Ni-Mn hybridization resulting in a shift of T_M to higher temperature. However, in the present study, the valence electron concentrations (e/a) for S0, S1, S2 and S3 films were calculated by using the electron configurations of the outer shells for each element and the values

determined from the EDAX analysis were 8.243, 8.193, 8.151 and 8.06, respectively. According to Feng *et al.* [21], the martensitic transition temperature (T_M) supposed to shift towards lower temperature. On the contrary, T_M for the S1, S2 and S3 films was found to shift towards higher temperatures as compared to S1 film. Therefore, it is clear that in the present system, the factor that drives the martensitic transition cannot be simply described in terms of (e/a). Similar to our findings, an opposite dependence of T_M on e/a has also been observed in several other systems, including $Ni_{50}Mn_{35-x}Cu_xSn_{15}$ system [31], Fe doped Ni-Mn-Fe-Sb and Ni-Mn-Fe-Ga systems [24, 32]. Other than the e/a ratio, there exist two other factors that may affect the T_M of FSMAs. One factor is the Ni-Mn hybridization. The partial substitution of Al for Mn influences the strength of the Ni-Mn hybridization of Ni-Mn-Sb-Al alloy thin films.The strength of this hybridization is strongly influenced by the Ni-Mn distance [28-29, 33-34]. Therefore, Al addition affects the Ni-Mn distance in Ni-Mn-Sb-Al alloy thin films, and it gets smaller as compared to pure Ni-Mn-Sb film Another possible factor is unit cell volume suggested from the literature. Substitutions of smaller Al atoms as compared to the Mn atoms exerts a positive external pressure on the Mn atoms as a result decrease of cell volume, evident from **figure 4.1 (b)** and **table 4.2**. There have been reports that the decrease of unit cell volume due to doping increases the martensitic transformation temperatures [26]. Hence, it can be concluded that the decrease in the Ni-Mn distance and a corresponding decrease of cell volume are only factors responsible for increasing T_M in our Ni-Mn-Sb-Al thin films. It was also observed that with increasing Al concentration, the magnitude of the magnetization slightly increased at T_M as shown in **figure 4.3**. In Mn rich Ni-Mn based alloys, the change in magnetization at T_M is attributed to the suppression of the antiferromagnetic (AFM) interactions of the martensitic phase during the phase transition [20]. The thermal hysteresis width (ΔT) of phase transformation changes with increase of Al concentration for different films as shown in **table 4.2**. The presence of smaller hysteresis widths in film S1, S2 and S3 as compared to S0 indicates thermo elastic phase transformations in Ni-Mn-Sb-Al thin films. It means that the deformation energy during the martensitic phase transformations was elastically stored in the twin morphology of the martensitic structure and therefore less energy was consumed for phase transition in these films [35]. This can decrease the phase transition response time of materials as a result these materials could be working as actuators and sensor.

4.1.3.3 Electrical properties

To further study the martensitic transformations in detail, the temperature dependent resistance (R-T) measurements were performed in the temperature range of 100-350 K. **Figure 4.4** shows the (R-T) plots of film S0-S3 determined by four-probe method. Similar to the (M-T) behavior, a thermal hysteresis in the (R-T) curves was observed in all the films. It is clear from **figure 4.4 (a)** that the pure Ni-Mn-Sb film (S0) exhibits the first order martensitic and reverse martensitic transformations during heating and cooling cycles in the temperature range from 292 to 313 K. The characteristic transition temperatures M_s = 292 K, M_f = 278 K, A_s = 298K and A_f = 313 K were almost in agreement with those measured from the (M-T) curve of S0 film. With decreasing temperature, film S0 exhibited a change in slope around 333 K indicating PM to FM transition at the Curie temperature (T_C^A) of austenite phase. Below M_s, the resistance was increased with decreasing temperature associated with an advancing transition into the martensitic phase. The abrupt change in resistance was found during heating and cooling cycles in the temperatures ranging from 278 to 313 K as a result of the first order martensitic transformation. Since the martensitic phase has higher resistance as compared with the austenite phase, the value of overall resistance decreases with increasing temperature, showing semiconductor behavior around the transformation temperature [36]. The sharp decrease of electrical resistance during martensitic transformation may be attributed to the formation of super zone boundary gaps, which alters the density of electronic states near the Fermi surface, where the variation of density of states also occurs in the vicinity of the Fermi level [37, 38]. Similarly, a remarkable resistance change at the martensitic transition temeperature has also been found in Ni-Mn-Sn thin films and it is attributed to superzone boundary effects, which is caused by structural and magnetic superstructures [39].
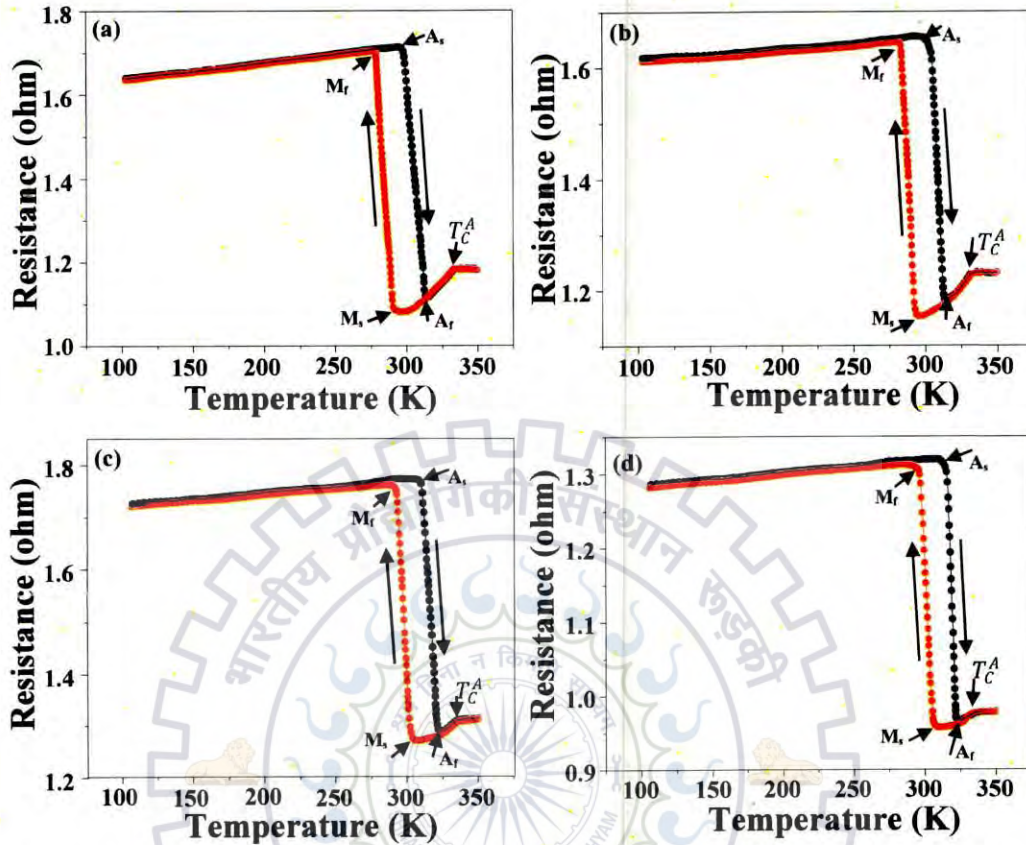
Figure 4.4. Electrical resistance versus temperature (R-T) curves obtained for (a) $Ni_{49.9}Mn_{37.4}Sb_{12.7}$ (A0), (b) $Ni_{49.8}Mn_{36.28}Sb_{12.8}Al_{1.12}$ (A1), (c) $Ni_{49.9}Mn_{35.1}Sb_{12.7}Al_{2.3}$ (A2) and (d) $N_{49.8}Mn_{32.97}Sb_{12.8}Al_{4.43}$ (A3) samples.

For the films S1, S2 and S3 the behavior associated with resistance as a function of temperature is relatively similar as that for film S0 except that the phase transition temperatures, during heating and cooling cycles, are shifted towards higher temperatures shown in **figure 4.4 (b)-(d)**. All the measured characteristic transition temperatures for Ni-Mn-Sb-Al alloy thin films are reported in **table 4.2**.

4.1.3.4 Magnetocaloric effect

To evaluate the MCE, isothermal magnetization (M-H) measurements were performed by applying a magnetic field from 0 to 2T at constant temperature intervals 3 K.

(85)
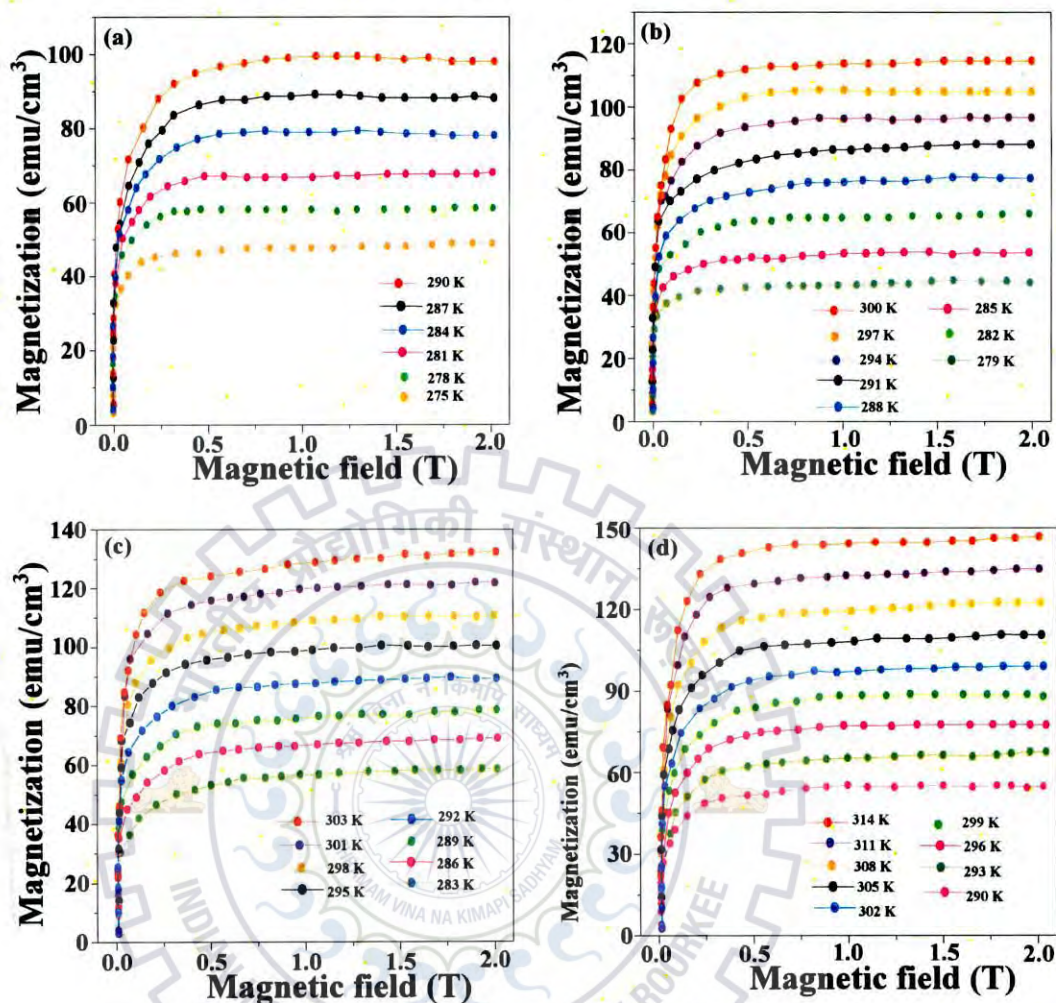
Figure 4.5. Isothermal (M–H) curves obtained for (a) $Ni_{49.9}Mn_{37.4}Sb_{12.7}$ (S0), (b) $Ni_{49.8}Mn_{36.28}Sb_{12.8}Al_{1.12}$ (S1), (c) $Ni_{49.9}Mn_{35.1}Sb_{12.7}Al_{2.3}$ (S2) and (d) $Ni_{49.8}Mn_{32.97}Sb_{12.8}Al_{4.43}$ (S3) films around the martensitic transformation temperature.

Figure 4.5 shows the isothermal (M-H) curves for films S0-S3 in the martensitic transformation temperature region. The measurements were carried out by cooling the films from 350 K down to the required temperature and then varying field from 0 to 2 T. With the increasing temperature, the magnetization increases and it is obvious from the **figure 4.5** that all films exhibited a ferromagnetic behavior. Due to the large difference of magnetization ΔM_{sf} (values are illustrated in **table 4.2**), a large entropy change (ΔS_M) is expected in Ni-Mn-Sb-Al films. The ΔS_M was calculated as a function of temperature at constant magnetic field from isothermal magnetization curves using the integrated Maxwell relation described in **section 3.3.6**. The

(86)

maximum value of ΔS_M and the width of the ΔS_M are the characteristic features of the MCE. The temperature dependence of ΔS_M was estimated for all the films with a maximum field change equal to 2 T and depicted in **figure 4.6**. As temperature increases, the ΔS_M also increases in the Ni-Mn-Sb-Al films and reaches to a maximum value at martensitic transformation temperature (T_M) before decreasing further. Such a positive sign of ΔS_M was attributed to the inverse MCE [40]. The increase in ΔS_M value upon Al concentration is evident from **figure 4.6**. The peak ΔS_M value obtained in the S0, S1, S2 and S3 films are 9, 15.1, 16.2 and 23 mJ/cm^3 K, respectively.
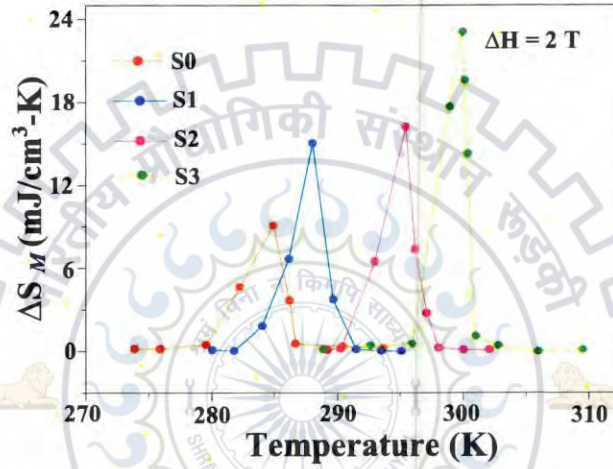
Figure 4.6. Magnetic entropy change SM versus temperature for Ni$_{49.9}$Mn$_{37.4}$Sb$_{12.7}$ (S0), Ni$_{49.8}$Mn$_{36.28}$Sb$_{12.8}$Al$_{1.12}$ (S1), Ni$_{49.9}$Mn$_{35.1}$Sb$_{12.7}$Al$_{2.3}$ (S2) and Ni$_{49.8}$Mn$_{32.97}$Sb$_{12.8}$Al$_{4.43}$ (S3) films in a field of 2 T.

The larger value obtained in the S3 film at 300 K, this is mainly due to a large magnetization difference (ΔM_{st}) and higher value of $\frac{\partial M}{\partial T}$. Remarkable enhancement of ΔS_M is obtained in the S3 film as compared to the S0. For these films, both the crystal and magnetic structures are different from the original phase during martensitic phase transformation in an applied field. This gives rise to a MCE due to a strong magneto crystalline coupling. Besides, the magneto-structural

Sample	Structural phase	Lattice parameter, a (nm)	Cell Volume (nm³)	M-T transition temperatures (K)						R-T transition temperatures (K)						ΔM_{sf} (emu/cm³)	ΔS_M (mJ/cm³ K)	RC (mJ/cm³)
				M_s	M_f	A_s	A_f	ΔT	T_C^A	M_s	M_f	A_s	A_f	ΔT	T_C^A			
S0	A	a = 0.5927	0.2082	287	276	297	310	23	333	292	278	298	313	20	333	49	9	27
S1	A	a = 0.5841	0.1992	292	283	301	311	19	333	294	283	301	314	18	333	69	15.1	45.3
S2	A+M	a = 0.5799	0.195	302	290	308	318	16	334	304	292	309	321	17	334	75	16.2	48.6
S3	M	a = 0.608, b = 0.5578, c = 0.5751	0.1945	306	298	312	321	15	335	307	297	313	323	16	335	94	23	64.4

Table 4.2. Variation of structural phase, cell volume, (M–T) & (R–T) transition temperatures, ΔM_{sf}, ΔS_M and RC values of $Ni_{49.9}Mn_{37.4}Sb_{12.7}$ (S0), $Ni_{49.8}Mn_{36.28}Sb_{12.8}Al_{1.12}$ (S1), $Ni_{49.9}Mn_{35.1}Sb_{12.7}Al_{2.3}$ (S2) and $Ni_{49.8}Mn_{32.97}Sb_{12.8}Al_{4.43}$ (S3) films.

transition gives rise to a change in the distance between the magnetic atoms in the crystal lattice which, in turn, results in a significant change in the magnetization. However, the physical mechanism of how the structural transition affects the magnetic interaction is still unknown and theoretical calculations in this Ni–Mn–Sb alloy system are required for further understanding.

Another important aspect of calculating a magnetic refrigerant for magnetocaloric materials is the refrigerant capacity (RC), which is a direct measure of the heat transferred from the cold reservoir to the hot reservoir in a refrigeration cycle. It is defined as in **section 3.3.6**. Here, the RC value is defined by the product of the maximum value of ΔS_M and full width at half maximum of the corresponding peak. In the present work, the RC values have been measured at martensitic transition temperature of all the films. The RC values for S0, S1, S2 and S3 films are 27, 45.3, 48.6 and 64.4 mJ/cm^3, respectively. This is mainly due to its wide temperature span of ΔS_M. The magnetic entropy change ΔS_M as well as RC are expected due to the large change of magnetization (ΔM_{sf}) during martensitic transition. The obtained results are very promising for micro length scale magnetic refrigeration applications.

4.1.4 Conclusions

In conclusion, we have investigated the effect of Al addition on martensitic phase transformation and MCE in Ni-Mn-Sb alloy thin films. Increase in Al content leads to a gradual increase in the martensitic transition temperature was observed in these films. A maximum magnetic entropy change of ΔS_M = 23 mJ/cm^3 K at 300 K for a magnetic field change of 2 T was observed in the $N_{49.8}Mn_{32.97}Sb_{12.8}Al_{4.43}$ alloy thin film. On the other hand, the refrigerant capacity RC reached to64.4 mJ/cm^3 at 2 T for this film. The increase in MCE is attributed to the large magneto-structural coupling, which causes a large magnetization difference and large value of $\frac{\partial M}{\partial T}$ upon Al concentration. Such a large MCE developed in the Ni-Mn-Sb-Al alloy thin films make them potential candidate for the micro length scale magnetic refrigeration.

4.2 Ni-Mn-In-Cr ferromagnetic shape memory alloy thin films

4.2.1 Introduction

In recent years, Ni-Mn based ferromagnetic shape memory alloys (FSMAs) have attracted considerable interest due to their technological applications as magnetic refrigerants, sensors and actuators. Due to the strong interaction coupling between the crystal structure and magnetism, these alloys experience a martensitic transformation from a high-symmetric austenitic phase to low-symmetric martensitic phase under cooling, and is associated with the abrupt drop of magnetization [41]. Since the discovery of magnetic field induced stain in N-Mn-Ga [43] and observation of martensitic transformation in Ni–Mn based FSMAs, there has been growing interest in the magneto-mechanical properties of Ni–Mn–X (X: In, Sb and Sn) [44–48]. In these alloys, the magnetic properties can affected by the change in Mn-Mn inter atomic distances and chemical composition of the alloy. In Ni-Mn based FSMAs, the martensitic transformation temperatures are strongly affected by the two main factors. Primarily, the valence electron concentration (e/a). Many experimental results shows that the martensitic transformation temperatures are almost linear relationship with the e/a [49–50]. Secondly, unit cell volume, it is broadly established that the unit-cell contraction of high-temperature austenite would promote the martensitic transformation owing to changes of the relative positions between the Fermi surface and the Brillouin zone. Han et $al.$ [51] observed that substituting smaller Ge for larger isoelectronic Sn atoms in $Ni_{43}Mn_{46}Sn_{11-x}Ge_x$ results in an increase of the phase transformation temperatures. Kokorin et $al.$ [52] found similar results when replacing larger In by smaller isoelectronic Ga atoms in $Ni_2MnGa_xIn_{1-x}$. In some cases, these size effects dominate the phase transformation behavior. Kanomata et $al.$ [53] observed that the phase transformation was suppressed in $Ni_{2-x}Cu_xMnGa$, where the substitution of Cu for Ni results in a higher e/a ratio and a larger unit-cell volume. Feng et $al.$ also found such abnormal e/a dependence in $Ni_{49-x}Cu_xMn_{39}Sb_{12}$ alloys [54].

Recently, several studies have also reported the magneto-structural properties of the Ni–Mn–In system [55–57]. With the aim of developing novel and better materials belonging to this series and to probe the effect of structural variation on the magnetic, mechanical and magnetocaloric effect in them, we have partially substituted Cr for In in the Ni-Mn-In alloy thin films. In this study, we significantly investigate the effect of Cr addition on the structural, phase transformation behavior, mechanical properties and manetocaloric effect of polycrystalline Ni-Mn-In FSMA thin films, and the main purpose is to pinpoint the martensitic transformation

behavior, microstructure changes, mechanical properties, and MCE. Our results show that Cr addition can significantly change in the structural transformation from $L2_1$ cubic austenitic phase to orthorhombic martensitic phase at room temperature and also it leads to a gradual increase in the martensitic transformation temperature (T_M). The magnetic entropy change ΔS_M of 7.0 mJ/cm^3 K at 302 K and refrigerant capacity of 39.2 mJ/cm^3 have observed in $Ni_{51.1}Mn_{34.9}In_{9.5}Cr_{4.5}$ film in an applied field of 2 T. Further, the room temperature nanoindentation measurements revealed a high hardness (28.2±2.4 GPa), elastic modulus (287.5±4.6 GPa), plasticity index (0.098), resistance to plastic deformation (0.261) and depth recovery ratio (0.613) were obtained in $Ni_{50.4}Mn_{34.96}In_{13.56}Cr_{1.08}$ alloy thin film. These findings indicate that the Cr substitution Ni-Mn-In alloy thin films are potential candidates for various multifunctional applications.

4.2.2 Experimental details

Ni-Mn-In-Cr alloy thin films were deposited by co-sputtering of $Ni_{50}Mn_{35}In_{15}$ and Cr targets onto Si (100) substrates at 823 K temperature using dc magnetron sputtering. Experimental procedure in detail is given in **section 3.1.2** and sputtering parameters are summarized in **table 4.3**. The crystallographic orientations of the deposited films were studied using a Bruker advanced diffractometer of Cu Kα (1.54Å) radiations in θ–2θ geometry at a scan speed of 1°/min. The surface morphology of the films was studied by field emission scanning electron microscopy (FESEM). The compositions of the films were determined by energy dispersive X-ray analysis (EDAX) attached with FESEM and the obtained nominal compositions were $Ni_{50.1}Mn_{34.98}In_{14.92}$, $Ni_{49.94}Mn_{34.96}In_{14.48}Cr_{0.62}$, $Ni_{50.4}Mn_{34.96}In_{13.56}Cr_{1.08}$, $Ni_{50.7}Mn_{34.93}In_{12.28}Cr_{2.2}$, $Ni_{51}Mn_{34.9}In_{10.9}Cr_{3.2}$ and $Ni_{51.1}Mn_{34.9}In_{9.5}Cr_{4.5}$ are represented by C0, C1, C2, C3, C4 and C5, respectively. The magnetic properties were studied with a VSM. The temperature dependent magnetization (M-T) measurements were performed with varying temperatures from 10 K to 350 K under field cooled (FC) and field heating (FH) cycles. The resistance versus temperatures (R-T) measurements were done by four-probe resistivity method over temperature range from 100 K to 350 K. The mechanical properties were studied using depth-sensing nanoindentation equipment. The nanoindentation experimental parameters were mentioned in **section 3.1.2**.

Deposition Process	Magnetron sputtering
Target	$Ni_{50}Mn_{35}In_{15}$, Cr
Base pressure	$\leq 2 \times 10^{-6}$ Torr
Gas used	Argon
Sputtering pressure	10 mTorr
Deposition time	15 minutes
Sputtering power	$Ni_{50}Mn_{35}In_{15}$:110 W, Cr: 10-40 W
Substrate	Silicon (100)
Substrate temperature	823 K
Substrate to Target distance	5 cm

Table 4.3. Sputtering parameters for Ni-Mn-In-Cr thin films.

4.2.3 Results and discussions

4.2.3.1 Structural properties

Figure 4.7 shows the room temperature XRD pattern of pure and Cr doped Ni-Mn-In thin films corresponding to sample C0, C1, C2, C3, C4 and C5.It is clear from the XRD pattern that all the films exhibited pure austenitic cubic $L2_1$ structure with the fundamental lattice reflection of (220) and super lattice reflections of (111) and (311). The broadening of the (220) austenite peak signifies decrease in the grain size with increase of Cr content. In addition, an observed shift in (220) reflection towards the higher angle indicates the decrease of cell volume due to smaller atomic radius of Cr atom as compared to the In. It is apparent from the XRD graph that an excess of Cr content in C4 and C5 transformed their crystal structure from an austenitic phase to orthorhombic martensitic phase. The presence of martensitic phase in C4 and C5 is reflected by the (202), (220) and (022) planes. The lattice constants for the films C0-C5 as estimated by the XRD pattern are depicted in **table 4.4**. Further, a gradual decrease in unit cell volume of Ni-Mn-In films was observed with increasing Cr content, and is summarized in **table 4.4**. However, for low Cr content (sample C1, C2 and C3) most of the Cr atoms are filled in the interstitial sites which leads to small volume contraction, whereas a large volume contraction could be considered for large Cr content in samples C4 and C5 as more Cr atoms enter the substitution sites. The average crystallite size was calculated from the XRD pattern using following Debye-Scherrer formula:[16].

$$L_{xrd} = 0.9\lambda/B\cos\theta\ldots\ldots\ldots\ldots\ldots\ldots\ldots(4.1)$$

where B is the full width half maximum (FWHM) of Bragg peak in radian, λ is the wave length of X-ray and θ is the Bragg angle. The average crystallite sizes was 36, 30, 18 and 10 nm for C0, C1, C2 and C3 films, respectively.
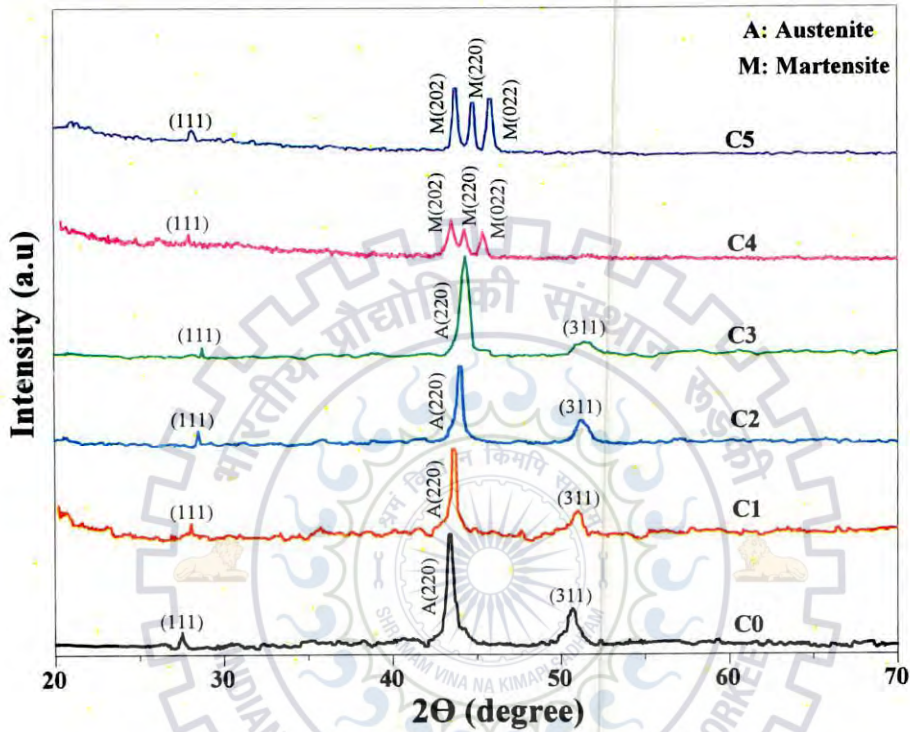
Figure 4.7. Room temperature XRD pattern of $Ni_{50.1}Mn_{34.98}In_{14.92}$ (C0), $Ni_{49.94}Mn_{34.96}In_{14.48}Cr_{0.62}$ (C1), $Ni_{50.4}Mn_{34.96}In_{13.56}Cr_{1.08}$ (C2), $Ni_{50.7}Mn_{34.93}In_{12.28}Cr_{2.2}$ (C3), $Ni_{51}Mn_{34.9}In_{10.9}Cr_{3.2}$ (C4) and $Ni_{51.1}Mn_{34.9}In_{9.5}Cr_{4.5}$ (C5) films.

Figure 4.8 (a)-(f) shows the surface morphology of the C0-C5 films as studied by FESEM. An apparent change in microstructure with changing Cr content could be easily seen in these films. The microstructure of the films gradually changes from a dense pyramidal shape for
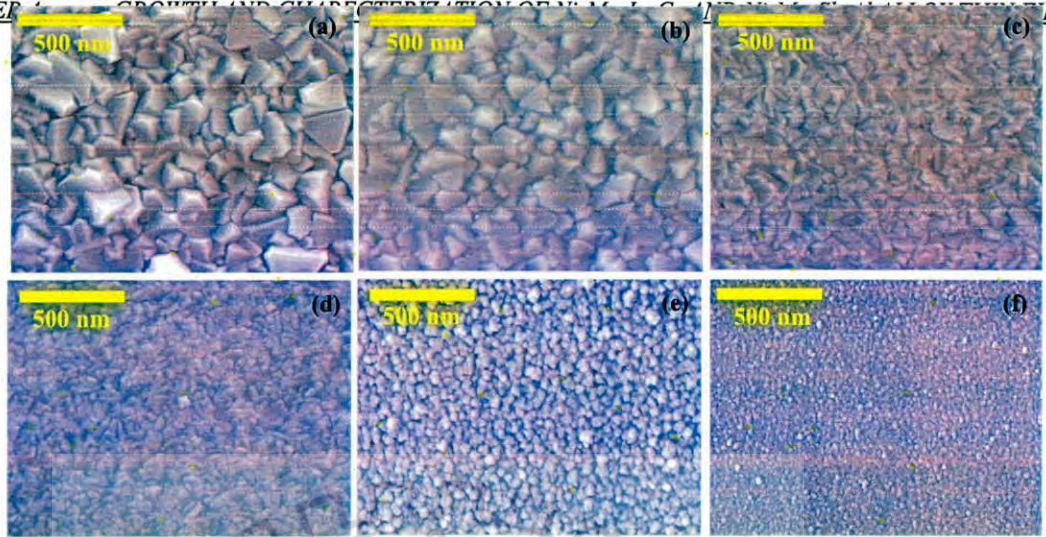
Figure 4.8. FESEM images of (a)-Ni$_{50.1}$Mn$_{34.98}$In$_{14.92}$, (b)-Ni$_{49.94}$Mn$_{34.96}$In$_{14.48}$Cr$_{0.62}$, (c)- Ni$_{50.4}$Mn$_{34.96}$In$_{13.56}$Cr$_{1.08}$, (d)-Ni$_{50.7}$Mn$_{34.93}$In$_{12.28}$Cr$_{2.2}$, (e)-Ni$_{51}$Mn$_{34.9}$In$_{10.9}$Cr$_{3.2}$ and (f)- Ni$_{51.1}$Mn$_{34.9}$In$_{9.5}$Cr$_{4.5}$ films.
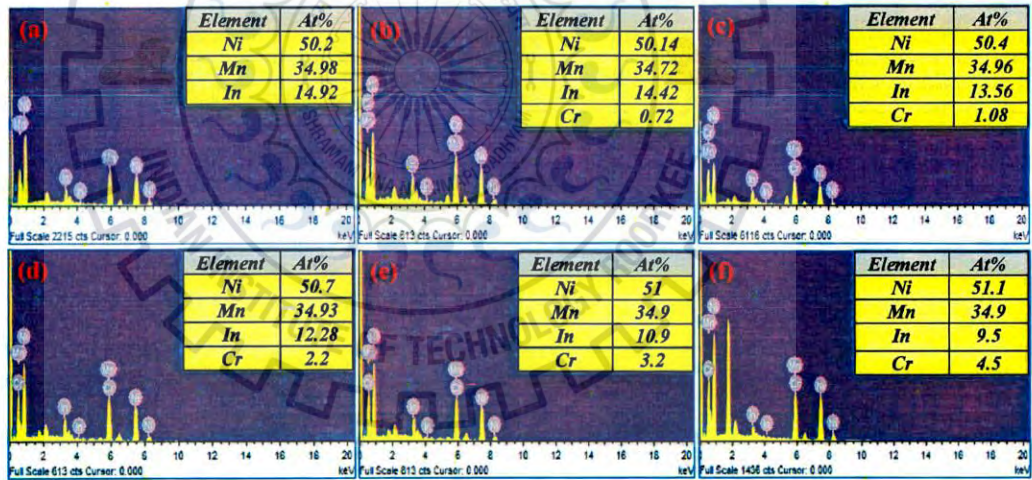
Figure 4.9. EDAX spectrum of (a)-Ni$_{50.1}$Mn$_{34.98}$In$_{14.92}$, (b)-Ni$_{49.94}$Mn$_{34.96}$In$_{14.48}$Cr$_{0.62}$, (c)- Ni$_{50.4}$Mn$_{34.96}$In$_{13.56}$Cr$_{1.08}$, (d)-Ni$_{50.7}$Mn$_{34.93}$In$_{12.28}$Cr$_{2.2}$, (e)-Ni$_{51}$Mn$_{34.9}$In$_{10.9}$Cr$_{3.2}$ and (f)- Ni$_{51.1}$Mn$_{34.9}$In$_{9.5}$Cr$_{4.5}$ films.

sample C0-C3 to spherical grains in sample C4 and C5 as a result of change in Cr concentration. The average grain size obtained by the section examination on different areas of the FESEM images for sample C0, C1, C2 and C3 was found to be 78, 57, 39 and 21 nm, respectively. The decrease in grain size with increasing Cr content is in well agreement with our XRD results.

(94)

However, the grain sizes determined by the FESEM results are quite larger than those shown by XRD, which is ascribed due to the fact that FESEM shows the agglomeration of the particles, whereas XRD gives an average mean crystallite size. The XRD and also FESEM information could be reconciled by simply believing that smaller primary particles possess a large surface energy and would, therefore, tend to agglomerate faster and grow into larger grains [37]. **Figure 4.9 (a)-(f)** shows the typical EDAX spectrum of C0-C5 films. The composition of the pure Ni-Mn-Infilm was greatly varied by increasing Cr concentration. We found that the increase of Cr content does not significantly affect the Ni and Mn concentrations, but reduces the In content to a great extent.

Sample	Lattice parameter a (nm)	Cell Volume (nm^3)	Avg. Grain size (nm)		e/a values
			XRD	**FESEM**	
C0	a= 0.5903, b= 0.5903, c= 0.5903	0.2056	36	78	7.906
C1	a= 0.5831, b= 0.5831, c= 0.5831	0.1982	30	57	7.912
C2	a= 0.5806, b= 0.5806, c= 0.5806	0.1957	18	39	7.915
C2	a= 0.5765, b= 0.5765, c= 0.5765	0.1916	10	21	7.927
C4	a= 0.6015, b= 0.5446, c= 0.5744	0.1881	--	--	7.934
C5	a= 0.6013, b= 0.5443, c= 0.5740	0.1878	--	--	8.123

Table 4.4. Various parameters obtained for pure Ni-Mn-In (C0) and Ni-Mn-In-Cr (C1, C2, C3, C4 and C5) films.

4.2.3.2 Magnetic properties

The influence of Cr addition on the martensitic transformation temperature of Ni-Mn-In thin films was further investigated by performing temperature dependent magnetization (M-T) measurements on C0-C5 films at a magnetic field of 0.02 T **(figure 4.10)**. The magnetization data for all the films was corrected to account for the diamagnetic contribution of the Si (100) substrate. In field cooling (FC) cycle, it can be clearly seen that these films undergo a paramagnetic (PM) to ferromagnetic (FM) transition. The temperature at which dM/dT data exhibit a minimum value is called the Curie temperature (T_C^A) of austenitic phase. With further decrease in temperature below T_C^A, the magnetization reached to a maximum value at M_s (martensitic start temperature) and thereafter, the austenitic phase loses its stability and magnetization suddenly reached to a minimum value M_f (martensitic finish temperature). In this transition region, the mixed austenitic and martensitic phases were found to co-exist [58]. The temperature corresponding to the martensitic transition (T_M) is defined as the mean of the M_s and M_f temperatures, i,e., (M_s+M_f)/2. Finally, with even more decrease in temperature, the

(95)

magnetization increases again and an inflection point appear, which is attributed to the Curie temperature of the martensitic phase (T_C^M) this could be due to the different crystal structure from the austenitic phase. This scenario usually occurs in Ni-Mn based FSMAs since Mn-Mn interatomic distances within the unit cell are different for the austenitic and martensitic phases, and these distances are determined to the magnetic ordering for the spin exchange interactions [59]. Similarly, during the field heating (FH) cycle, the reverse martensitic transformation was observed which defines the austenitic start (A_s) and austenitic finish (A_f) temperatures. It is found that the FH curve does not retrace the FC curve and a thermal hysteresis width (ΔT) was presented in all the films. The presence of this thermal hysteresis indicates the existence of first-order structural transition [60]. It can be seen that the Curie temperatures of martensitic (T_C^M) and austenitic phases (T_C^A) increases dramatically with an increase in the Cr content. The increasing T_C^M with increasing Cr content illustrates an enhancement of the martensitic exchange interaction in C1, C2, C3, C4 and C5 films. The characteristic phase transition temperatures (M_s, M_f, A_s, A_f, T_M, T_C^M and T_C^A) and corresponding hysteresis width (ΔT) values of all the films as determined from the (M-T) curves are listed in **table 4.5**. The (M-T) behavior (**figure 4.10 (b)-(f)**) of C1, C2, C3, C4 and C5 films were similar toC0, but the martensitic transformation temperatures (T_M) were shifted towards higher temperatures. A monotonous increase in martensitic transformation temperature was observed with the addition of Cr content as shown in **table 4.5**. There are reports that shows that the martensitic transformation temperatures (T_M) are very sensitive to the composition, mainly through the valence electron concentration (e/a) in Ni-Mn based FSMAs [61]. When the Fermi surface reaches the Brillouin zone boundary, structural instabilities appear and a martensitic transformation takes place [62]. The change in the number of valence electrons and the modification of the Brillouin zone boundary are considered to be the effective driving forces for the occurrence of martensitic structural transformations [63]. In the present study, the calculated valence electron includes are Ni ($3d^8\ 4s^2$), Mn ($3d^5\ 4s^2$), In ($5s^2\ 5p^1$) and Cr ($3d^5\ 4s^1$). The obtained value of e/a is 7.906, 7.912, 7.915, 7.927, 7.934 and 8.123 for C0, C1, C2 C3, C4 and C5, respectively. However, the substitution of Cr for In increases the value of e/a (**Table 4.4**) and thereby increases the martensitic transformation temperatures. For that reason, e/a factor can
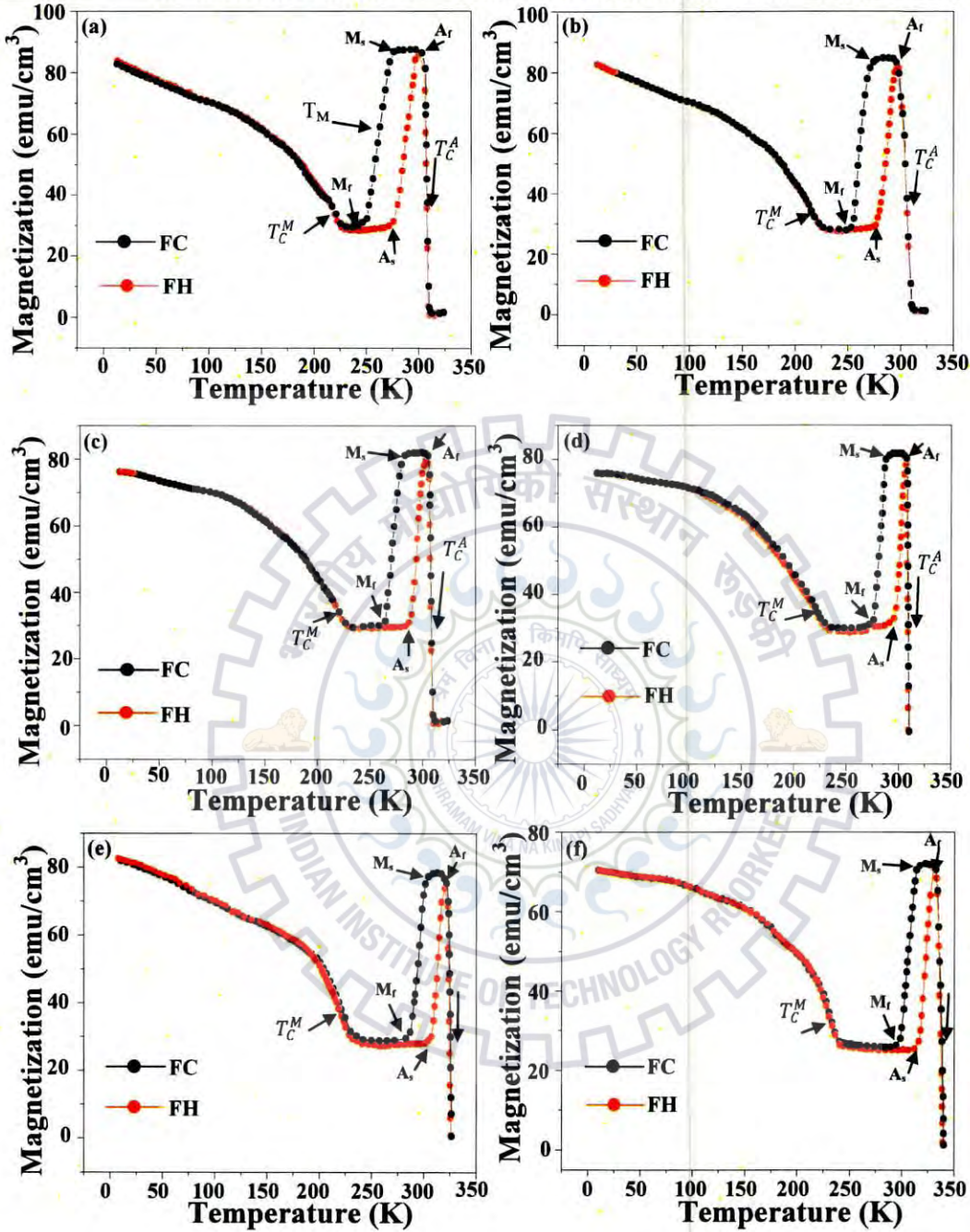
Figure 4.10. FC and FH magnetization as a function temperature (M-T) curves
(a)-$Ni_{50.1}Mn_{34.98}In_{14.92}$, (b)-$Ni_{49.94}Mn_{34.96}In_{14.48}Cr_{0.62}$, (c)-$Ni_{50.4}Mn_{34.96}In_{13.56}Cr_{1.08}$,
(d)-$Ni_{50.7}Mn_{34.93}In_{12.28}Cr_{2.2}$, (e)-$Ni_{51}Mn_{34.9}In_{10.9}Cr_{3.2}$ and (f)-$Ni_{51.1}Mn_{34.9}In_{9.5}Cr_{4.5}$.

be considered to be the driving force for increasing T_M temperatures in these films. Similarly,
previous reports on Fe doped Ni–Mn–In [64], Sb doped Ni-Mn-In [65], Cr doped Ni-Mn-In [66]

(97)

and Fe doped Ni–Mn–Sn [67] showed a good proportionally between T_M and valence electron concentration (e/a). Generally, the magnetization in Ni-Mn based FSMAs is mainly due to Mn atoms and thereby the magnetic exchange interactions and magnetic transformation temperatures are very sensitive to the distance of Mn-Mn atoms [68]. In the present study, the substitution of Cr for In may modify the Mn-Mn distance and may have some influence on the T_M of the parent phase. Moreover, in the martensitic phase, contraction of lattice parameter leads to a decrease in Mn–Mn distance. In this case, due to decrease in Mn–Mn distance, antiferromagnetic (AFM) interaction gets strengthened and this enhanced AFM interaction takes a toll on FM and hence the drop in magnetization around T_M arises [69]. Although the small decrease of magnetization with the increase of Cr content can be observed around the T_M for these films shown in **figure 4.10**. In addition, the substitution of smaller Cr atoms as compared to the In parent atoms exerts a positive external pressure on the parent atoms, as a result decrease in cell volume (**Table 4.4**). It can be related to the fact that the addition of Cr increases the martensitic transformation temperatures. In light of above discussion, in C1, C2, C3, C4 and C5 films, the shift of T_M towards higher temperatures due to increase of e/a values and decrease of cell volume as compared to C0 film. Therefore, both e/a and cell volume are responsible for the increasing of T_M in these films. Similar to our results, Chen *et al.* [70] also found that both e/a and cell volume considerably influence the T_M. As a consequence, the thermal hysteresis width (ΔT) becomes noticeably narrowed with the increase of Cr content in these films. Since the thermal hysteresis arises from the friction associated with phase boundary motion, the decrease of thermal hysteresis indicates less energy was consumed for phase boundary motion and the phase transition would be easier [71].This also can reduce the phase transition response time of the materials working as actuator and sensor. The characteristic phase transition temperatures (M_s, M_f, A_s, A_f, T_C^M, and T_C^A) of all the films, determined from the (M-T) curves, are illustrated in **table 4.5**.

4.2.3.3 Electrical properties

Figure 4.11 shows the resistance versus temperature (R-T) plots of C0-C5 films measured by four-probe method.
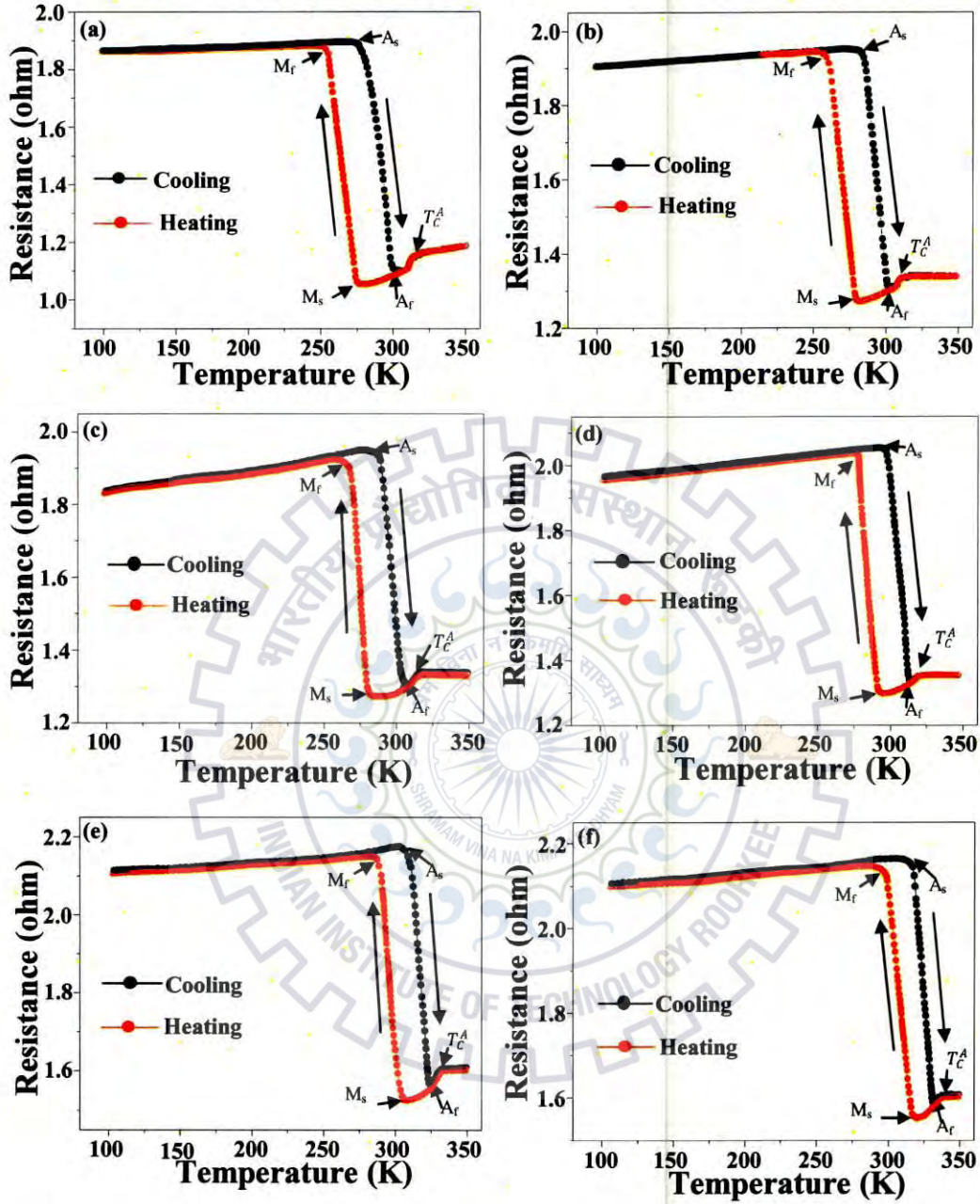
Figure 4.11. Electrical resistance verses temperature (R-T) curves of (a)-$Ni_{50.1}Mn_{34.98}In_{14.92}$, (b)-$Ni_{49.94}Mn_{34.96}In_{14.48}Cr_{0.62}$, (c)-$Ni_{50.4}Mn_{34.96}In_{13.56}Cr_{1.08}$, (d)-$Ni_{50.7}Mn_{34.93}In_{12.28}Cr_{2.2}$, (e)-$Ni_{51}Mn_{34.9}In_{10.9}Cr_{3.2}$ and (f)- $Ni_{51.1}Mn_{34.9}In_{9.5}Cr_{4.5}$ films.

Sample	M-T transition temperatures (K)							R-T transition temperatures (K)						Hardness (GPa)	Elastic modulus (GPa)	H/E	H^3/E^2	δ	ΔM_{sf} (emu/cm³)	ΔS_M (mJ/cm³ K)	RC (mJ/cm³)
	M_s	M_f	A_s	A_f	ΔT	T_C^M	T_C^A	M_s	M_f	A_s	A_f	ΔT	T_C^A								
C0	275	252	276	299	24	218	310	275	256	277	299	23	312	5.5±1.2	146.6±3.4	0.037	0.007	0.533	150	11.2	97.4
C1	278	255	279	300	22	219	311	278	260	282	301	22	313	16.5±1.8	203.8±3.8	0.08	0.108	0.484	---	---	---
C2	282	264	288	304	20	221	312	283	267	288	307	21	315	28.2±2.4	287.5±4.6	0.098	0.261	0.613	81	10.4	64.5
C3	291	276	297	308	18	223	313	293	279	297	312	18	324	22.3±1.1	258.8±4.2	0.086	0.165	0.591	42	9.6	55.6
C4	304	287	309	321	17	227	324	306	289	306	323	17	331	10.4±2.1	184.6±3.5	0.056	0.056	0.562	---	---	---
C5	315	295	316	331	16	230	333	318	299	315	332	16	337	8.2±1.3	178.3±3.7	0.045	0.017	0.541	63	7.0	39.2

Table 4.5. Details of (M-T) & (R-T) transition temperatures and various mechanical properties obtained for pure Ni-Mn-In (C0) and Ni-Mn-In-Cr (C1, C2, C3, C4 and C5) films also magnetization difference (ΔM_{sf}), magnetic entropy change (ΔS_M) and refrigerant capacity (RC) values for C0, C2, C3 and C5, respectively.

M_s and M_f represents the martensitic start and finish temperatures and whereas the corresponding temperatures of the austenitic phase are denoted by A_s and A_f, respectively. From **figure 4.11 (a)**, it is clear that the C0 film exhibits the first order martensitic and reverses martensitic transformations during heating and cooling cycles in the temperatures ranging from 291 to 310 K. In heating cycle, the resistance is comparatively constant until the temperature reaches about 291 K after which it drops suddenly at the A_s transition. With further increase in temperature, the resistance increases linearly until it reaches about 320 K (T_C^A), where the slope of the curve changes due to second-order transition from ferromagnetic austenite to paramagnetic austenite state. Since the martensitic phase has higher resistance as compared to the austenite phase, the value of overall resistance decreases with increasing temperature, showing semiconductor behavior around the transformation temperature [36]. The sudden decrease of electrical resistance with the amount of martensitic transformation could be due to the development of super zone boundary gaps, which in turn adjust the density of electronic states close to the Fermi surface [37]. Similarly, a remarkable resistance change at the martensitic transition temperature has also been found in other representative FSMAs and is attributed by a number of factors, such as drastic changes in crystal and electronic structure, Fermi surface, scattering probability, etc [36]. For C1, C2, C3, C4 and C5, the R-T behavior is relatively similar to that of film C0 except that the phase transition temperatures, during heating and cooling cycles, are shifted towards higher temperatures as shown in **figure 4.11 (b)-(f)**. All the measured phase transition temperatures for C0, C1, C2, C3, C4 and C5 films summarized in **table 4.5**.

4.2.3.4 Magnetocaloric effect

To evaluate the MCE, the isothermal magnetization (M-H) curves were measured around martensitic transformation temperatures (T_M) in a field change up to 2 T as shown in **figure 4.12**. Here we measured the MCE in C0, C2, C3 and C5 films. The measurements were performed by cooling the films from 350 K down to the required temperature and then varying field from 0 to 2 T. Under an applied field H, all films exhibit typical soft ferromagnetic behavior. The isotherms have been calculated in an interval of 3 K, in the increasing temperature mode. In the present study, the MCE (magnetic entropy change ΔS_M) was measured using Maxwell's relation [40] mentioned in **section 3.3.6** by **equations (3.6) & (3.7).**
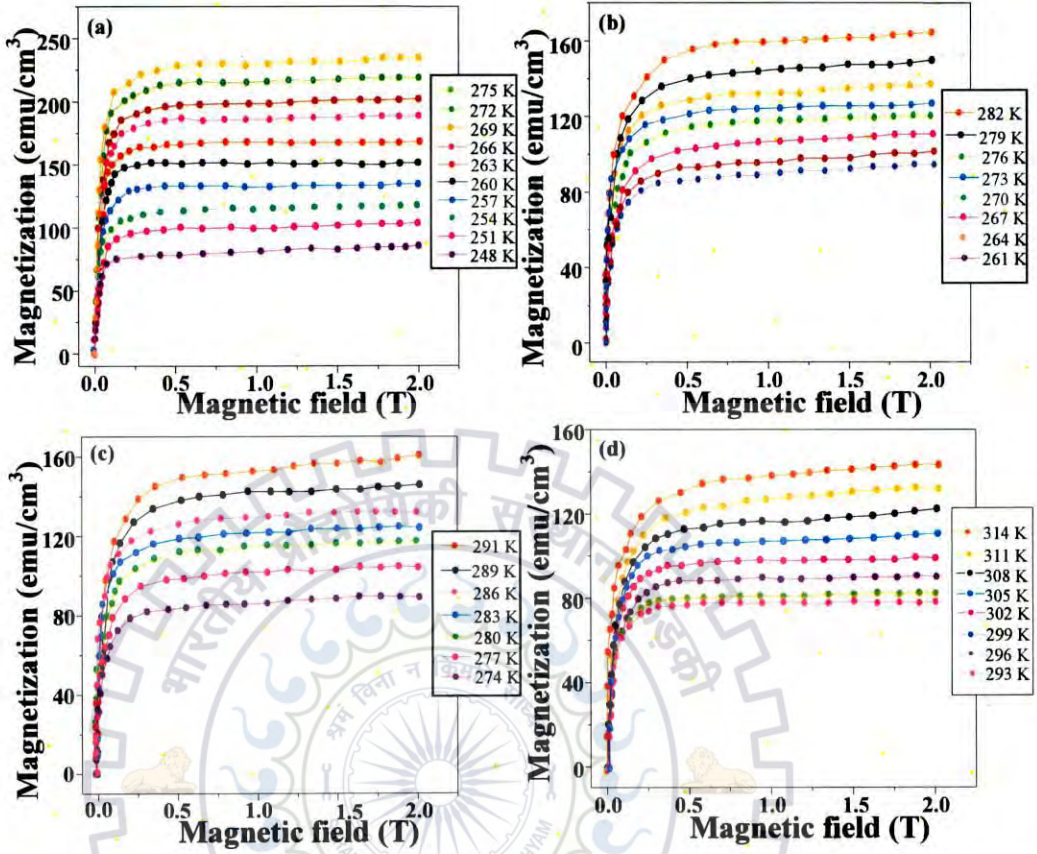
Figure 4.12. Isothermal magnetization (M-H) curves for (a)-$Ni_{50.12}Mn_{34.96}In_{14.92}$ (C0), (b)-$Ni_{50.4}Mn_{34.96}In_{13.56}Cr_{1.08}$ (C2), (c)-$Ni_{50.7}Mn_{34.93}In_{12.28}Cr_{2.2}$ (C3) and (d)-$Ni_{51.1}Mn_{34.9}In_{9.5}Cr_{4.5}$ (C5) films around their martensitic transformation temperatures. The temperature step is 3 K.

The temperature dependent magnetic entropy change (ΔS_M) in all the films is depicted in **figure 4.13**. It can be seen that ΔS_M shows a spike-like behavior as a function of temperature. The ΔS_M is positive for all the films due to the $\frac{\partial M}{\partial T}$ is being positive around the T_M. The peak value of ΔS_M and the width of the ΔS_M both are important characteristic features of the MCE. The decrease in ΔS_M upon Cr addition is observed from **figure 4.13**. The variation of peak ΔS_M value for all the films was found in the applied field of 2 T. The obtained peak ΔS_M value for C0, C2, C3 and C5 films are 11.2, 10.4, 9.6, and 7.0 mJ/cm^3 K, respectively. From **figure 4.13**, it can be seen that the ΔS_M value decreases monotonically with the addition of Cr content. Among these films, the highest value of ΔS_M =11.2 mJ/cm^3 K at 259 K has been obtained for C0 film it could be ascribed to the large change of magnetization (ΔM_{sf}) value as compared to other films (**Table 4.5**). The ΔS_M value of 7.0 mJ/cm^3 K in $Ni_{51.1}Mn_{34.9}In_{9.5}Cr_{4.5}$ is also promising due to fact that it occurs at

(102)

near room temperature (302 K). The possibility of MCE at near room temperature makes this system quite useful for micro-length scale magnetic refrigeration technology.
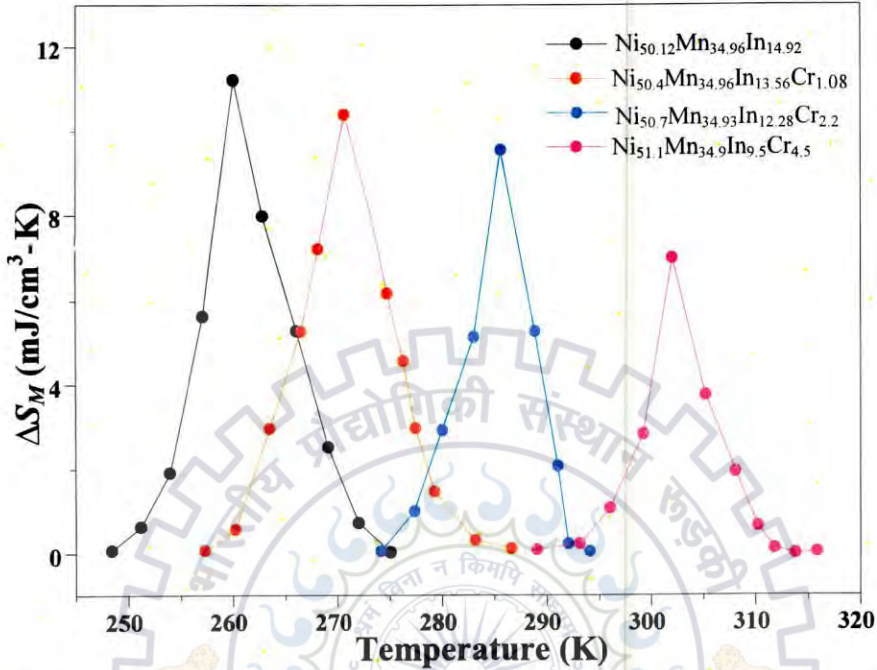
Figure 4.13. Magnetic entropy change ΔS_M as a function of temperature for $Ni_{50.12}Mn_{34.96}In_{14.92}$, $Ni_{50.4}Mn_{34.96}In_{13.56}Cr_{1.08}$, $Ni_{50.7}Mn_{34.93}In_{12.28}Cr_{2.2}$ and $Ni_{51.1}Mn_{34.9}In_{9.5}Cr_{4.5}$ films in field of 2 T.

Another important parameter for magnetocaloric materials is the refrigerant capacity (RC). The RC value can be calculated of the heat transferred from the cold reservoir to the hot reservoir in a refrigeration cycle. It is defined by the **equation (3.8)**. The RC values corresponding to the peak ΔS_M obtained for $Ni_{50.12}Mn_{34.96}In_{14.92}$, $Ni_{50.4}Mn_{34.96}In_{13.56}Cr_{1.08}$, $Ni_{50.7}Mn_{34.93}In_{12.28}Cr_{2.2}$ and $Ni_{51.1}Mn_{34.9}In_{9.5}Cr_{4.5}$ films are found to be 97.4, 55.6, 39.2 mJ/cm^3, respectively for a field change of 2 T. The $Ni_{50.12}Mn_{34.96}In_{14.92}$ film shows the maximum RC value of 97.4 mJ/cm^3 among all the films. This is mainly due to its wide temperature span of ΔS_M. Such a broader temperature span indicates a higher RC obtained in FSMAs [72].

4.2.3.5 Mechanical properties

Figure 4.14 shows the typical load-displacement curves obtained for C0, C1, C2 and C3 films. The nanoindentation curves are used to measure the average hardness (H), elastic modulus (E), the ratio of hardness to elastic modulus (H/E, a measure of the partitioning between energy dissipation by elastic and plastic deformation in the indentation contact), plasticity index (plastic work done/total work done) plasticity index (H/E), resistance to plastic deformation (H^3/E^2) and depth recovery ratio (δ) whose values are reported in **table 4.5**. The hardness and elastic modulus were measured by load–displacement data by the analytic method developed by Oliver and Phar [73]. It was observed that the hardness and elastic modulus both are get influenced by the concentration of Cr content in these films. The higher hardness (28.2±2.4 GPa) and elastic modulus (287.5±4.6 GPa) were obtained in C2 film as compared with other films (**Table 4.5**), and thereby the pure Ni-Mn-In (C0) film showing hardness and elastic modulus are 7.8±1.2 GPa and 175.6±3.4 GPa, respectively. The average hardness and elastic modulus are increased almost linearly with increasing Cr content in the C1, C2 and C3 films (**Table 4.5**). This could be attributed due to the two factors; decrease in the grain size and grain refinement which obey the well-known Hall-Petch relationship [74] given in **section 3.3.4 (Equation 3.4)**. The **equation (3.4)** is valid only when the grain size is approximately greater than the tens of nanometer. Further reduction in grain size brings about a decrease in strength because of grain boundary sliding. The observed decrease in hardness below the critical grain size of 21 nm could be attributed to grain boundary sliding mechanisms. Softening caused by grain boundary sliding is mainly attributed to the large amount of defects in the grain boundaries, which allow fast diffusion of atoms and vacancies under stress [37]. It can be noticed that the yield strength of the material is strongly affected by the grain size. The increase in hardness as a result of the large number of grain boundaries act as a barrier to the dislocation motion. Here, grain boundaries act as pinning points that impede the dislocation propagation. In general, plastic deformation, dislocation movement and grain boundary sliding are prevented to accomplish high hardness and reduction in ductility. However, C3 film having a smaller grain size as compared with other films which indicates a decrease in hardness and greater inclination toward plastic deformation. The other important mechanical property is elastic modulus of the material which is related to stiffness. Generally, high stiffer materials have higher value of elastic modulus. In our case C2 film shown higher value of elastic modulus 287.5±4.6 GPa. Further, the plasticity index (H/E) is
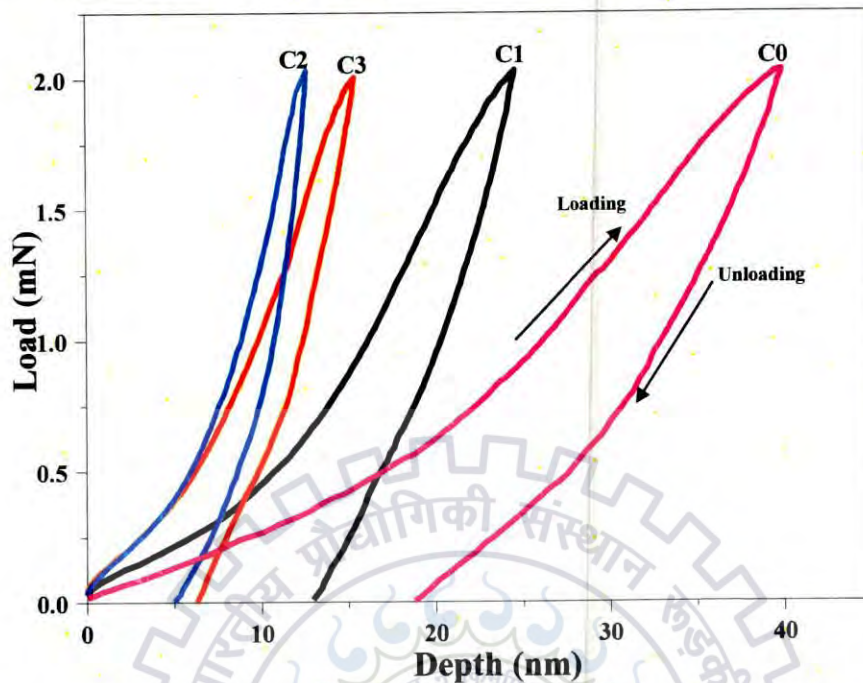
Figure 4.14. Load versus depth curves obtained for $Ni_{50.1}Mn_{34.98}In_{14.92}$ (C0), $Ni_{49.94}Mn_{34.96}In_{14.48}Cr_{0.62}$ (C1), $Ni_{50.4}Mn_{34.96}In_{13.56}Cr_{1.08}$ (C2), $Ni_{50.7}Mn_{34.93}In_{12.28}Cr_{2.2}$ (C3) films.

an essential parameter to discriminate the elastic and elastic–plastic behavior. The higher the H/E ratio indicates the good wear resistance of the film. Lower value of H/E ratio indicated that more fraction of work is consumed in plastic deformation and large plastic strain is expected when contacting a material [75]. The value of H/E ratio was found to be higher in case of C2 (0.098), which showed that less work is consumed in plastic deformation and thereby exhibits better wear resistance. Additionally, the resistance to plastic deformation $H^3/E^2 = 0.261$ was also higher in the C2 film as compared with the other films. In light of above discussion, Ni-Mn-in-Cr films with higher hardness also tend to have higher H^3/E^2. The main advantage of the Ni–Mn–In–Cr thin films with higher toughness (H^3/E^2) is that these films will be more resistant to the formation of cracks as compared with the pure Ni–Mn–In film during dynamic contact loading. The indentation induced super elastic depth recovery ratio (δ) is obtained from the load-displacement curves as **equation (3.5)** [76]. The calculated δ values are illustrated in **table 4.5**. The lower the value of h_{max}, the greater the hardness of the film, whereas the lower the value of h_r, the greater the elasticity of the film. For film C2, the room temperature depth recovery ratio is higher as compared to other Ni-Mn-In-Cr alloy films. For C4 and C5 films, the sharp decrease in the

hardness and elastic modulus could be due to the martensitic phase present at room temperature. The martensitic phase films have distorted crystal structure (nonsymmetrical) so that, nanoindentation tip can easily penetrate into the film as a result decrease in hardness and elastic modulus. In our case, Cr addition in Ni-Mn-In thin films show higher hardness, better wear resistance and high resistance to plastic deformation as compared to pure Ni-Mn-In thin film, therefore, Ni-Mn-In-Cr alloy thin films are potential candidate for MEMS device applications.

4.2.4 Conclusion

In summary, the effect of Cr addition on structure, martensitic transformation, electrical and mechanical properties of Ni-Mn-In alloy thin films was systematically investigated. With the increase of Cr concentration, the Ni-Mn-In-Cr alloy thin films showed a change in the structural transformation from $L2_1$ cubic austenitic phase to orthorhombic martensitic phase at room temperature. Increase in Cr content also leads to a gradual increase in the martensitic transformation temperature (T_M) were observed in these films, thus, due to increasing of e/a ratio and decrease of cell volume. The ΔS_M of 7.0 mJ/cm^3 K at 302 K and refrigerant capacity of 39.2 mJ/cm^3 have been found in $Ni_{51.1}Mn_{34.9}In_{9.5}Cr_{4.5}$ film in an applied field of 2 T. Further, the room temperature nanoindentation measurements revealed a high hardness (28.2±2.4 GPa), elastic modulus (287.5±4.6 GPa), plasticity index (0.098), resistance to plastic deformation (0.261) and depth recovery ratio (0.613) were obtained in $Ni_{50.4}Mn_{34.96}In_{13.56}Cr_{1.08}$ alloy thin film. These findings indicate that the Cr substitution Ni-Mn-In alloy thin films are potential candidates for various multifunctional applications.

4.3 References

[1]   Brück E., "Developments in magnetocaloric refrigeration," *J. Phys. D. Appl. Phys.*, **38**, R381–R391 (2005).

[2]   Phan M. H., Yu S. C., "Review of the magnetocaloric effect in manganite materials," *J. Magn. Magn. Mater.*, **308**, 325 (2007).

[3]   Gscneidner Jr. K.A., Pecharsky V. K., "Magnetocaloric materials," *Annu. Rev. Mater. Sci.*, **30**, 387 (2001).

[5]   Kuz'Min M. D., Tishin A. M., "Magnetocaloric effect part 2: magnetocaloric effect in heavy rare earth metals and their alloys and application to magnetic refrigeration," *Cryogenics*, **33**, 868 (1993).

[6]   Morozkin A. V., Nirmala R., Malik S. K., "Magnetism and magnetocaloric effect in YNi$_4$Si-type RNi$_4$Si (R=Ce, Gd, Tb and Dy) compounds," *J. Magn. Magn. Mater.*, **378**, 221 (2015).

[7]   Hughes I. D., Däne M., Ernst A., Hergert W., Lüders M., Poulter J., Staunton J. B., Svane A., Szotek Z., Temmerman W. M., "Lanthanide contraction and magnetism in the heavy rare earth elements.," *Nature*, **446**, 650 (2007).

[8]   Talik E., Klimczak M., "Giant magnetocaloric effect in Tb$_3$Rh," *J. Alloys Compd.*, vol. **486**, L30 (2009).

[9]   Wada H., Tanabe Y., "Giant magnetocaloric effect of MnAs$_{1-x}$Sb$_x$," *Appl. Phys. Lett.*, **79**, 3302 (2001).

[10] Hu F. X., Shen B. G., Sun J. R., Cheng Z. H., Rao G. H., Zhang X. X., "Influence of negative lattice expansion and metamagnetic transition on magnetic entropy change in the compound LaFe$_{11.4}$Si$_{1.6}$," *Appl. Phys. Lett.*, **78**, 3675 (2001).

[11] Sun N. K., Ma S., Zhang Q., Du J., Zhang Z. D., "Large room-temperature magnetocaloric effects in Fe$_{0.8}$Mn$_{1.5}$As," *Appl. Phys. Lett.*, **91**, 2013 (2007).

[12] Pasquale M., Sasso C. P., Lewis L. H., Giudici L., Lograsso T., Schlagel D., "Magnetostructural transition and magnetocaloric effect in Ni$_{55}$Mn$_{20}$Ga$_{25}$ single crystals," *Phys. Rev. B*, **72**, 094435 (2005).

[13] Stadler S., Khan M., Mitchell J., Ali N., Gomes A. M., Dubenko I., Takeuchi A. Y., Guimarães A. P., "Magnetocaloric properties of Ni$_2$Mn$_{1-x}$Cu$_x$Ga," *Appl. Phys. Lett.*, **88**, 192511 (2006).

[14] Han Z. D., Wang D. H., Zhang C. L., Xuan H. C., Gu B. X., Du Y. W., "Low-field inverse magnetocaloric effect in Ni$_{50-x}$Mn$_{39+x}$Sn$_{11}$ Heusler alloys," *Appl. Phys. Lett.*, **90**, 042507 (2007).

[15]   Du J., Zheng Q., Ren W. J., Feng W. J., Liu X. G., Zhang Z. D., "Magnetocaloric effect and magnetic-field-induced shape recovery effect at room temperature in ferromagnetic Heusler alloy Ni–Mn–Sb," *J. Phys. D. Appl. Phys.*, **40**, 5523 (2007).

[16]   Chatterjee S., Giri S., Majumdar S., De S. K., "Magnetic after-effect in Ni-Mn-Sb Heusler alloy," *J. Magn. Magn. Mater.*, **320**, 617 (2008).

[17]   Sharma V. K., Chattopadhyay M. K., Shaeb K. H. B., Chouhan A., Roy S. B., "Large magnetoresistance in $Ni_{50}Mn_{34}In_{16}$ alloy," *Appl. Phys. Lett.*, **89**, 222509 (2006).

[18]   Khan M., Ali N., Stadler S., "Inverse magnetocaloric effect in ferromagnetic $Ni_{50}Mn_{37+x}Sb_{13-x}$ Heusler alloys," *J. Appl. Phys.*, **101**, 053919 (2007).

[19]   Feng W. J., Du J., Li B., Hu W. J., Z. D. Zhang, Li X. H., Deng Y. F., "Large low-field inverse magnetocaloric effect in $Ni_{50-x}Mn_{38+x}Sb_{12}$ alloys," *J. Phys. D. Appl. Phys.*, **42**, 125003 (2009).

[20]   Nong N. V., Tai L. T., Huy N. T., Trung N. T., Bahl C. R. H., Venkatesh R., Poulsen F. W., Pryds N., "Structural, magnetic and magnetocaloric properties of Heusler alloys $Ni_{50}Mn_{38}Sb_{12}$ with boron addition," *Mater. Sci. Eng. B*, **176**, 1322 (2011).

[22]   Han Z. D., Wang D. H., Zhang C. L., Xuan H. C., Zhang J. R., B. X. Gu, Du Y. W., "The phase transitions, magnetocaloric effect, and magnetoresistance in Co doped Ni-Mn-Sb ferromagnetic shape memory alloys," *J. Appl. Phys.*, **104**, 053906 (2008).

[23]   Nayak A. K., Suresh K. G., Nigam A. K., "Giant inverse magnetocaloric effect near room temperature in Co substituted NiMnSb Heusler alloys," *J. Phys. D: Appl. Phys.*, **42**, 035009 (2010).

[24]   Sahoo R., Nayak A. K., Suresh K. G., Nigam A. K., "Effect of Si and Ga substitutions on the magnetocaloric properties of NiCoMnSb quaternary Heusler alloys," *J. Appl. Phys.*, **109**, 07A921 (2011).

[25]   Zhang Y., Hughes R. A., Britten J. F., Dube P. A., Preston J. S., Botton G. A., Niewczas M., "Magnetocaloric effect in Ni-Mn-Ga thin films under concurrent magnetostructural and Curie transitions," *J. Appl. Phys.*, **110**, 013910 (2011).

[26]   Wang R. L., Yan J. B., Xu L. S., Marchenkov V. V., Chen S. S., Tang S. L., Yang C. P., "Effect of Al doping on the martensitic transition and magnetic entropy change in NiMnSn alloys," *Solid State Commun.*, **151**, 1196 (2011).

[27]   Liu Y., Huang X., "Substrate-induced stress and transformation charecteristics of a deposited Ti-Ni-Cu thin film," *Philos. Mag.*, **84**, 1919 (2004).

[28]   Priolkar K. R., Lobo D. N., Bhobe P. A., Emura S., Nigam A. K., "Role of Ni-Mn hybridization in magnetism of martensitic state of Ni-Mn-In shape memory alloys," **94**, 38006 (2011).

[29] Khan M., Jung J., Stoyko S. S., Mar A., Quetz A., Samanta T., Dubenko I., Ali N., Stadler, Chow K. H., "The role of Ni-Mn hybridization on the martensitic phase transitions in Mn-rich Heusler alloys," *Appl. Phys. Lett.*, **100**, 172403 (2012).

[30] Roy S., Blackburn E., Valvidares S. M., Fitzsimmons M. R., Vogel S. C., Khan M., Dubenko I., Stadler S., Ali N., Sinha S. K., Kortright J. B., "Delocalization and hybridization enhance the magnetocaloric effect in Cu-doped Ni_2MnGa," *Phys. Rev. B*, **79**, 235127 (2009).

[31] Gao B., Shen J., Hu F. X., Wang J., Sun J. R., Shen B. G., "Magnetic properties and magnetic entropy change in Heusler alloys $Ni_{50}Mn_{35-x}Cu_xSn_{15}$," *Appl. Phys. A*, **97**, 443 (2009).

[32] Liu Z. H., Zhang M., Wang W. Q., Wang W. H., Chen J. L., Wu G. H., Meng F. B., Liu H. Y., Liu B. D., Qu J. P., Li Y. X., "Magnetic properties and martensitic transformation in quaternary Heusler alloy of NiMnFeGa," *J. Appl. Phys.*, **92**, 5006 (2002).

[33] Khan M., Dubenko I., Stadler S., Jung J., Stoyko S. S., Mar A., Quetz A., Samanta T., N. Ali, Chow K. H., "Enhancement of ferromagnetism by Cr doping in Ni-Mn-Cr-Sb Heusler alloys," *Appl. Phys. Lett.*, **102**, 112402 (2013).

[34] Khan M., Pathak A. K., Paudel M. R., Dubenko I., Stadler S., Ali N., "Magnetoresistance and field-induced structural transitions in $Ni_{50}Mn_{50-x}Sn_x$ Heusler alloys," *J. Magn. Magn. Mater.*, **320**, L21 (2008).

[35] Wang R. L., Yan J. B., Xu L. S., Marchenkov V. V., Chen S. S., Tang S. L., Yang C. P., "Effect of Al doping on the martensitic transition and magnetic entropy change in NiMnSn alloys," *Solid State Commun.*, **151**, 1196 (2011).

[36] Srivastava S. K., Srivastava V. K., Varga L. K., Khovaylo V. V., Kainuma R., Nagasako M., Chatterjee R., "Systematic study of structural, transport, and magnetic properties of $Ni_{52+x}Mn_{26-x}Al_{22}$ ($1 \leq x \leq 5$) melt-spun ribbons," *J. Appl. Phys.*, **109**, 083915 (2011).

[37] Vishnoi R., Singhal R., Kaur D., "Thickness dependent phase transformation of magnetron-sputtered Ni–Mn–Sn ferromagnetic shape memory alloy thin films," *J. Nanoparticle Res.*, **13**, 3975 (2011).

[38] Zhang B., Zhang X. X., Yu S. Y., Chen J. L., Cao Z. X., Wu G. H., "Giant magnetothermal conductivity in the Ni-Mn-In ferromagnetic shape memory alloys," *Appl. Phys. Lett.*, **91**, 012510 (2007).

[39] Auge A., Teichert N., Meinert M., Reiss G., Hütten A., Yüzüak E., Dincer I., Elerman Y., Ennen I., Schattschneider P., "Thickness dependence of the martensitic transformation, magnetism, and magnetoresistance in epitaxial Ni-Mn-Sn ultrathin films," *Phys. Rev. B*, **85**, 214118 (2012).

[40]   Sharma V. K., Chattopadhyay M. K., Kumar R., Ganguli T., Tiwari P., Roy S. B., "Magnetocaloric effect in Heusler alloys $Ni_{50}Mn_{34}In_{16}$ and $Ni_{50}Mn_{34}Sn_{16}$," *J. Phys. Condens. Matter*, **19**, 496207 (2007).

[41]   Sutou Y., Imano Y., Koeda N., Omori T., Kainuma R., Ishida K., Oikawa K., "Magnetic and martensitic transformations of Ni-Mn-X(X=In, Sn, Sb) ferromagnetic shape memory alloys," *Appl. Phys. Lett.*, **19**, 4358 (2004).

[42]   Wuttig M., Liu L. H., Tsuchiya K., James R. D., "Occurrence of ferromagnetic shape memory alloys (invited)", *J. Appl. Phys.*, **87**, 4707 (2000).

[43]   Ullakko K., Huang J. K., Kantner C., O'Handley R. C., Kokorin V. V., "Large magnetic-field-induced strains in Ni_2MnGa single crystals", *Appl. Phys. Lett.*, **69**, 1966 (1996).

[44]   Mañosa L., Moya X., Planes A., Gutfleisch O., Lyubina J., Barrio M., Tamarit J. L., Aksoy S., Krenke T., Acet M., "Effects of hydrostatic pressure on the magnetism and martensitic transition of Ni-Mn-In magnetic superelastic alloys," *Appl. Phys. Lett.*, **92**, 012515 (2008).

[45]   Zheng H., Wang W., Xue S., Zhai Q., Frenzel J., Luo Z., "Composition-dependent crystal structure and martensitic transformation in Heusler Ni-Mn-Sn alloys," *Acta Mater.*, **61**, 4648 (2013).

[46]   Schastlivtsev V. M., Kaletina Y. V., Fokina E. A., Kazantsev V. A., "Martensitic and magnetic transformations in Ni-Mn-In alloys," *Phys. Met. Metallogr.*, **112**, 64 (2011).

[47]   Chatterjee S., Giri S., Majumdar S., De S. K., "Magnetic after-effect in Ni-Mn-Sb Heusler alloy," *J. Magn. Magn. Mater.*, **320**, 617 (2008).

[48]   Kainuma R., Imano Y., Ito W., Morito H., Sutou Y., Oikawa K., Fujita A., Ishida K., Okamoto S., Kitakami O., Kanomata T., "Metamagnetic shape memory effect in a Heusler-type $Ni_{43}Co_7Mn_{39}Sn_{11}$ polycrystalline alloy," *Appl. Phys. Lett.*, **88**, 192513 (2006).

[49]   Moya X., Manosa L. I., Planes A., Krenke T., Acet M., Wassermann E. F., "Martensitic transition and magnetic properties in Ni–Mn–X alloys", *Mater. Sci. Eng A*, **438–440**, 911 (2006).

[50]   Krenke T., Moya X., Aksoy S., Acet M., Entel P., Mañosa L., Planes A., Elerman Y., Yücel A., Wassermann E. F., "Electronic aspects of the martensitic transition in Ni-Mn based Heusler alloys," *J. Magn. Magn. Mater.*, **310**, 2788 (2007).

[51]   Han Z. D., Wang D. H., Zhang C. L., Xuan H. C., Zhang J. R., Gu B. X., Du Y. W., "Effect of lattice contraction on martensitic transformation and magnetocaloric effect in Ge doped Ni-Mn-Sn alloys," *Mater. Sci. Eng. B*, **157**, 40 (2009).

[52]   Kokorin V.V., Osipenko I.A., Shirina T.V., "Phase transitions in alloys $Ni_2MnGa_xIn_{1-x}$," *Phys. Met. Metallogr.*, **67**, 173 (1989).

[53]   Kanomata T., Nozawa T., Kikuchi D., Nishihara H., Koyama K.,Watanabe K., "Magnetic properties of ferromagnetic shape memory alloys $Ni_{2-x}Cu_xMnGa$", Int. J. Appl. Electrom., **21**, 151 (2005).

[54]   Feng W. J., Zuo L., Li Y. B., Wang Y. D., Gao M., Fang G. L., "Abnormal e/a-dependence of T_M and large inverse magnetocaloric effect in $Ni_{49-x}Cu_xMn_{39}Sb_{12}$ alloys," *Mater. Sci. Eng. B*, **176**, 621 (2011).

[55]   Sharma V. K., Chattopadhyay M. K., Roy S. B., "Studies on the field-induced martensite to austenite phase transition in $Ni_{50}Mn_{34}In_{16}$ alloy", *J. Phys.: Condens. Matter*, **20**, 425210 (2008).

[56]   Krenke T., Duman E., Acet M., Wassermann E. F., Moya X., Mañosa L., Planes A., Suard E., Ouladdiaf B., "Magnetic superelasticity and inverse magnetocaloric effect in Ni-Mn-In," *Phys. Rev. B*, **75**, 104414 (2007).

[57]   Krenke T., Acet M., Wassermann E. F., Moya X., Mañosa L., Planes A., "Ferromagnetism in the austenitic and martensitic states of Ni-Mn-In alloys," *Phys. Rev. B*, **73**, 174413 (2006).

[58]   Sahoo R., Nayak A. K., Suresh K. G., Nigam A. K., "Effect of Si and Ga substitutions on the magnetocaloric properties of NiCoMnSb quaternary Heusler alloys," *J. Appl. Phys.*, **109**, 07A921 (2011).

[59]   Liu Z. H., Aksoy S., Acet M., "Influence of Sb on the magnetic and magnetocaloric properties of ferromagnetic shape memory alloy NiMnIn," *J. Appl. Phys.*, **105**, 033913 2009.

[60]   Khan M., Dubenko I., Stadler S., Jung J., Stoyko S. S., Mar A., Quetz A., Samanta T., N. Ali, Chow K. H., "Enhancement of ferromagnetism by Cr doping in Ni-Mn-Cr-Sb Heusler alloys," *Appl. Phys. Lett.*, **102**, 112402 (2013).

[61]   Krenke T., Moya X., Aksoy S., Acet M., Entel P., Mañosa L., Planes A., Elerman Y., Yücel A., Wassermann E. F., "Electronic aspects of the martensitic transition in Ni-Mn based Heusler alloys," *J. Magn. Magn. Mater.*, **310**, 2788 (2007).

[62]   Webster P. J., Ziebeck K. R. A., Town S. L., Peak M. S., "Magnetic order and phase transformation in Ni_2MnGa," *Philos. Mag. Part B*, **49**, 295 (1984).

[63]   Gao B., Shen J., Hu F. X., Wang J., Sun J. R., Shen B. G., "Magnetic properties and magnetic entropy change in Heusler alloys $Ni_{50}Mn_{35-x}Cu_xSn_{15}$," *Appl. Phys. A*, **97**, 443 (2009).

[64]   Lobo D. N., Priolkar K. R., Emura S., Nigam A. K., "Ferromagnetic interactions and martensitic transformation in Fe doped Ni-Mn-In shape memory alloys," *J. Appl. Phys.*, **116**, 183903 (2014).

[65] Yu S. Y., Yan S. S., Zhao L., Feng L., Chen J. L., Wu G. H., "Intermartensitic transformation and magnetic field effect in NiMnInSb ferromagnetic shape memory alloys," *J. Magn. Magn. Mater.*, **322**, 2541 (2010).

[66] Sánchez-Alarcos V., Recarte V., Pérez-Landazábal J. I., Chapelon J. R., Rodríguez-Velamazán J. A., "Structural and magnetic properties of Cr-doped Ni–Mn–In metamagnetic shape memory alloys," *J. Phys. D. Appl. Phys.*, **39**, 395001 (2011).

[67] Zhao X. G., Tong M., Shih C. W., Li B., Chang W. C., Liu W., Zhang Z. D., "Microstructure, martensitic transitions, magnetocaloric, and exchange bias properties in Fe-doped Ni-Mn-Sn melt-spun ribbons," *J. Appl. Phys.*, **113**, 17A913 2013.

[68] Chernenko V., L'vov V., Zagorodnyuk S., Takagi T., "Ferromagnetism of thermoelastic martensites: Theory and experiment," *Phys. Rev. B*, **67**, 064407 (2003).

[69] Ray M. K., Bagani K., Singh R. K., Majumdar B., Banerjee S., "Effect of Al doping on structural and magnetic properties of $Ni_{50}Mn_{37}Al_xSb_{13-x}$ alloy," *Phys. B Condens. Matter*, **448**, 33 (2014).

[70] Chen X.Q., Yang F.J., Lu X., Qin Z. X., "The way composition affects martensitic transformation temperatures of Ni–Mn–Ga Heusler alloys," *Phys. Status Solidi*, **244**, 1047 (2007).

[71] Wang W. H.,. Chen J. L, Liu Z., Wu G. H., Zhan W. S., "Thermal hysteresis and friction of phase boundary motion in ferromagnetic $Ni_{52}Mn_{23}Ga_{25}$ single crystals," *Phys. Rev. B*, **65**, 012416 (2001).

[72] Xuan H. C., Han P. D., Wang D. H., Du Y. W., "The influence of Ge substitution on the magnetostucture transition and magnetocaloric effect of Mn-Ni-Sn-Ge alloys," *J. Alloys Compd.*, **582**, 369 (2014).

[73] Oliver W. C., Pharr G. M., "Measurement of hardness and elastic modulus by instrumented indentation: Advances in understanding and refinements to methodology," *J. Mater. Res.*, **19**, 3 (2004).

[74] Chokshi A. H., Rosen A., Karch J., Gleiter H., "On the validity of the hall-petch relationship in nanocrystalline materials," *Scr. Metall.*, **23**, 1679 (1989).

[75] Choudhary N., Kharat D. K., Kaur D., "Structural, electrical and mechanical properties of magnetron sputtered NiTi/PZT/TiOx thin film heterostructures," *Surf. Coatings Technol.*, **205**, 3387 (2011).

[76] Ni W., Cheng Y. T., Grummon D. S., "Microscopic superelastic behavior of a nickel-titanium alloy under complex loading conditions," *Appl. Phys. Lett.*, **82**, 2811 (2003).

Chapter 5

Exchange Bias Effect in Ni-Mn-Sb/CrN Heterostructures Synthesized by Magnetron Sputtering

CHAPTER 5

EXCHANGE BIAS EFFECT IN Ni-Mn-Sb/CrN HETEROSTRUCTURES SYNTHESIZED BY MAGNETRON SPUTTERING

5.1 Introduction

After discovery of exchange bias (EB) phenomenon [1] associated with the exchange anisotropy generated at the antiferromagnetic (AFM) and ferromagnetic (FM) interface, extensive research has been performed on the materials possessing exchange bias properties for their potential applications on spin valves, read heads, permanent magnets, sensors, and magnetic recording heads, etc. Usually, exchange bias is observed in small oxide particles, inhomogeneous materials, nanostructures, bilayer and multilayer thin films, and spin glass systems [2-6]. One of several promising materials showing exchange bias behavior that have attracted developing interest in recent years tend to be ferromagnetic shape memory alloys (FSMAs) due to their various mulifunctional properties such as magnetic shape memory effect, superelasticity, magnetoresistace, magnetocaloric effect which are associated with martensitic transformation [7]. The exchange bias behavior has been reported for some of ternary and their quaternary bulk alloys [8-9]. However, there are limited studies on growth of these films. Recently, Ritu *et al.* [10] has investigated the exchange bias effect in magnetron sputtered $Ni_{49.8}Mn_{36.1}Sn_{13.9}$ thin films deposited on Si (100) substrate, which has been ascribed to the existence of FM/AFM exchange interactions this could be due to the coexistence of ferromagnetic and antiferromagnetic phases in the martensitic phase of the films at low temperatures below blocking temperature (T_B). To the best of our knowledge; there is no report on exchange bias behaviour of FM/AFM bilayer thin films based ferromagnetic shape memory alloys.

In the present study, hard, adherent, and corrosion resistant CrN was chosen as antiferromagnetic layer that undergoes a first order phase transition at about 280 K, where the ferromagnetic B1 NaCl crystal structure transforms to the antiferromagnetic orthorhombic structure. Heterostructure thin films of Ni-Mn-Sb (FM)/CrN (AFM) were synthesized on Si (100) substrate using magnetron sputtering and exchange bias has been studied. Furthermore, the influence of AFM thickness in magnetic and mechanical properties of these heterostructures has been investigated.

5.2 Experimental details

Thin films of Ni-Mn-Sb and various Ni-Mn-Sb/CrN heterostructures with different CrN thicknesses (15 nm–80 nm) were grown on Si (100) substrate at a temperature of 823 K using DC magnetron sputtering. High purity (99.99%) $Ni_{50}Mn_{37}Sb_{13}$ and Cr (Chromium) targets of 50.8 mm diameter and 3 mm thickness were used. All the Ni-Mn-Sb films of approximately 140 nm

thickness were prepared in an argon (99.99% pure) atmosphere. CrN films of different thicknesses were prepared in a mixture of argon and nitrogen (50:50) atmosphere. The deposition parameters were summarized in **table 5.1**. Post annealing has not been carried out after the deposition. The films S1, S2, S3, S4, and S5 correspond to $Ni_{50}Mn_{36.8}Sb_{13.2}$ film and $Ni_{50}Mn_{36.8}Sb_{13.2}$/CrN (15 nm– 80 nm) heterostructures. Inset of **figure 5.1** shows the schematic diagram of the deposited films. The thicknesses of the films were measured by surface profilometer. The magnetization measurements were performed using Superconducting Quantum Interference Device (SQUID) magnetometer (MPMS, Quantum Design) in the temperature range of 10 to 300 K and applied magnetic fields up to 4 T. The nanoindentation technique was used to calculate the mechanical properties such as hardness, elastic modulus and along with other properties.

Deposition Process	DC Magnetron sputtering
Target	$Ni_{50}Mn_{37}Sb_{13}$, Cr
Base pressure	$\leq 2\times10^{-6}$ Torr
Gas used	Ar for $Ni_{50}Mn_{37}Sb_{13}$ and Ar+N_2 for Cr
Sputtering pressure	10 mTorr
Deposition time	$Ni_{50}Mn_{37}Sb_{13}$: 4 min, CrN: 2-8 min
Sputtering power	$Ni_{50}Mn_{37}Sb_{13}$:90 W, Cr: 80 W
Substrate	Silicon (100)
Substrate temperature	823 K
Target to Substrate distance	5 cm

Table 5.1. Sputtering parameters for Ni-Mn-Sb and Ni-Mn-Sb/CrN heterostructure thin films.

5.3 Results and discussion

Figure 5.1 shows the X-ray diffraction pattern of $Ni_{50}Mn_{36.8}Sb_{13.2}$ (S1), CrN and $Ni_{50}Mn_{36.8}Sb_{13.2}$/80 nm CrN (S5) thin films. The XRD pattern of $Ni_{50}Mn_{36.8}Sb_{13.2}$ film shows super lattice peak (311) along with dominant fundamental peak (220), which confirms L2$_1$ structure and $Ni_{50}Mn_{36.8}Sb_{13.2}$/80 nm CrN (S5) film shows the (111) reflection of CrN along with (220) and (311) reflections of Ni-Mn-Sb.
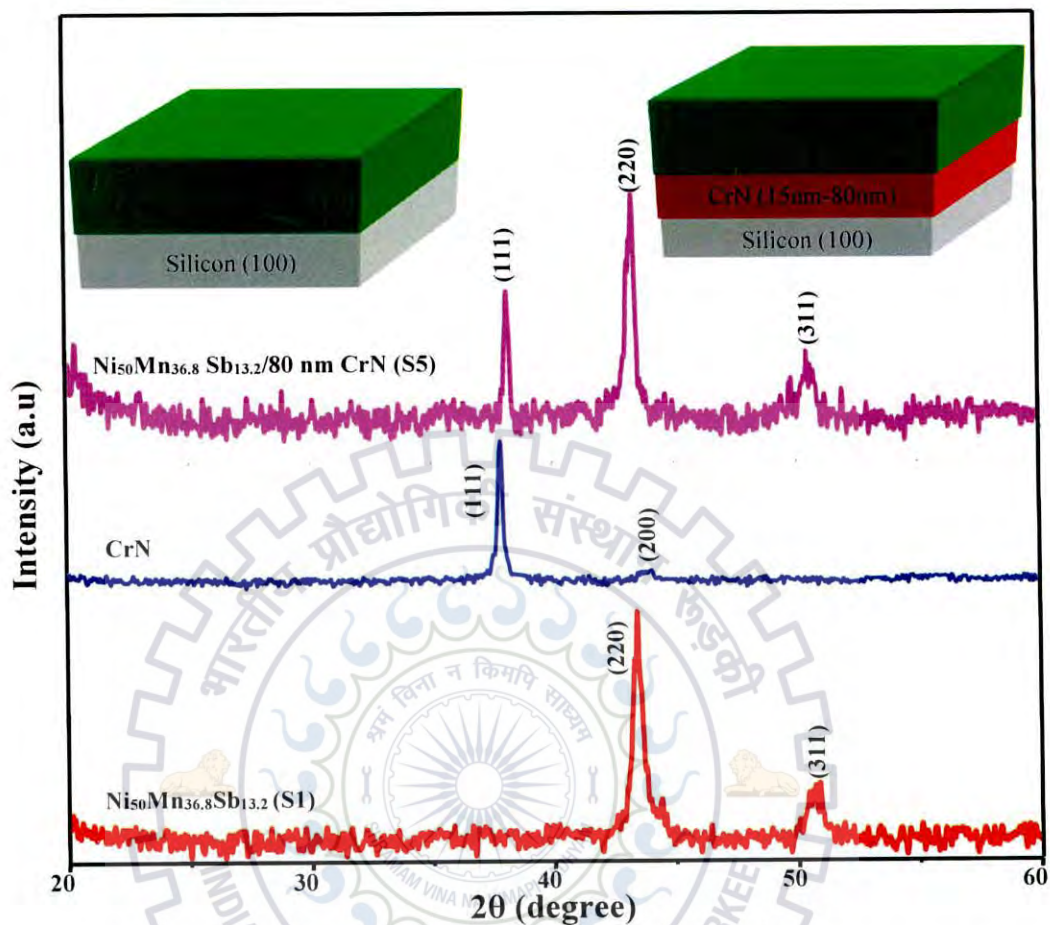
Figure 5.1. XRD pattern of $Ni_{50}Mn_{36.8}Sb_{13.2}$ film, CrN film and $Ni_{50}Mn_{36.8}Sb_{13.2}$/CrN heterostructure thin film (S5) on Si (100).

5.3.1 Exchange bias behavior

In order to investigate the exchange bias (EB) behavior, the field dependence magnetization (M-H) loops were measured at different temperatures by cooling the films in presence of magnetic field from 310 K down to required temperature of interest and then varying the field in the range of 0.01 T to 4 T. The magnetization data for films were corrected to account for the diamagnetic contribution of the Si (100) substrate. **Figures 5.2 (a)–2(c)** shows the FC magnetic hysteresis loops of $Ni_{50}Mn_{36.8}Sb_{13.2}$ (S1) film at three different temperatures of 10 K, 270 K, and 295 K, respectively. For $Ni_{50}Mn_{36.8}Sb_{13.2}$ (S1) film, the exchange bias field (H_{EB}) was found to be 51 Oe at 10 K which was higher than an earlier reported value of 41 Oe in $Ni_{49.8}Mn_{36.1}Sn_{13.9}$ thin films

[10]. The observed exchange bias has been attributed to the fact that the ferromagnetic domains are inserted in an antiferromagnetic matrix as a result ferromagnetic-antiferromagnetic exchange interaction occurs at the interface of phase separation which causes a unidirectional anisotropy. It has been reported in Ni-Mn-X (X = Sb, Sn, and In) alloys, all the Mn atoms on regular Mn sites have a ferromagnetic interaction, whereas additional Mn atoms occupying the X sites are coupled via antiferromagnetic interaction to the surrounding Mn atoms. The distance of Mn-Mn between Mn atoms at regular sites and Mn atoms at X sites decreases under martensitic transformation and this decrease in Mn-Mn distance will also contribute to antiferromagnetic exchange between them [11]. **Figures 5.2 (d)–2(f)** shows the FC magnetic hysteresis loops of $Ni_{50}Mn_{36.8}Sb_{13.2}$/35 nm CrN heterostructure (S3) at 10 K, 270 K, and 295 K, respectively. The maximum value of exchange bias of 148 Oe was observed at 10 K, 38 Oe at 270 K, and 10 Oe at 295 K for sample S3. At 10 K, higher value of exchange bias was observed in S3 is due to the fact that at this temperature the $Ni_{50}Mn_{36.8}Sb_{13.2}$ also contributes to exchange bias. By adding AFM CrN layer to the $Ni_{50}Mn_{36.8}Sb_{13.2}$ film, artificially we are making FM/AFM interface and increasing the anisotropy of AFM layer. Therefore, $Ni_{50}Mn_{36.8}Sb_{13.2}$/CrN heterostructures shows exchange bias even at 270 K which was below the Neel temperature of CrN (270 K). In comparison, $Ni_{50}Mn_{36.8}Sb_{13.2}$ film (S1) does not show any exchange bias at 270 K. The essential parameter in exchange bias phenomenon is how to understand the exchange interaction between the ferromagnetic and antiferromagnetic phases which leads to a unidirectional anisotropy. The experimental results showed that the magnetization hysteresis (M-H) loop shifted from the origin, it indicates two different configuration phases present in the system. At 10 K and 270 K temperatures, the exchange coupling at FM/AFM interface gives rise to preferred orientation of Ni-Mn-Sb spins and unidirectional anisotropy of CrN layer. It is known that the anisotropy of CrN is small, when the magnetic field is reversed and the spins in the FM phase start to rotate, as a result some spins in the AFM phase can be dragged by them.
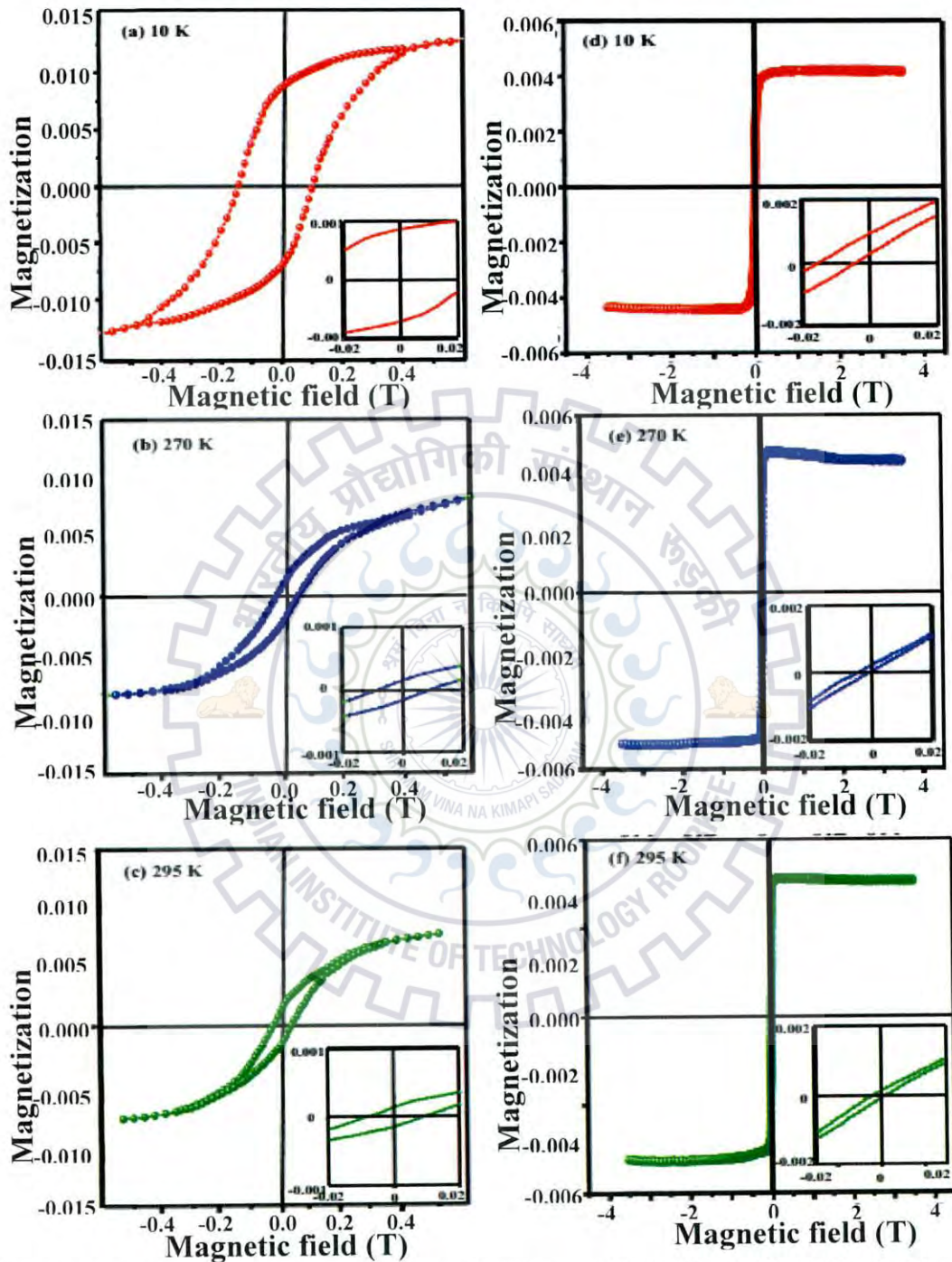
Figure 5.2. M-H loops of $Ni_{50}Mn_{36.8}Sb_{13.2}$ film measured at (a) T = 10 K, (b) T = 270 K, and (c) T = 295 K and Magnetization hysteresis loops of $Ni_{50}Mn_{36.8}Sb_{13.2}$/CrN heterostructure measured at (d) T = 10 K, (e) T = 270 K, and (f) T = 295 K. The inset shows the enlarged view of the low field region of the loops.

(119)

5.3.2 Variation of H_{EB} and H_C with antiferromagnetic layer thickness

The AFM thickness dependence of the exchange bias field H_{EB} and the coercivity H_C at 270 K are shown in **figure 5.3 (a)**. The exchange bias field H_{EB} and coercivity H_C are calculated using **equations (3.6) and (3.7)** as mentioned in **section 3.3.5**. At 270 K, with increasing CrN layer thickness from 15 nm to 80 nm, the exchange bias was found to increase and reach to maximum value of 38 Oe. Thereafter, further increase in AFM thickness does not produce much change in the exchange bias field. This could be due to the fact that with increasing the AFM (CrN layer) thickness, the number of inhomogeneities also increased in the AFM layer which plays a major role in pinning the spin configuration of AFM layer.
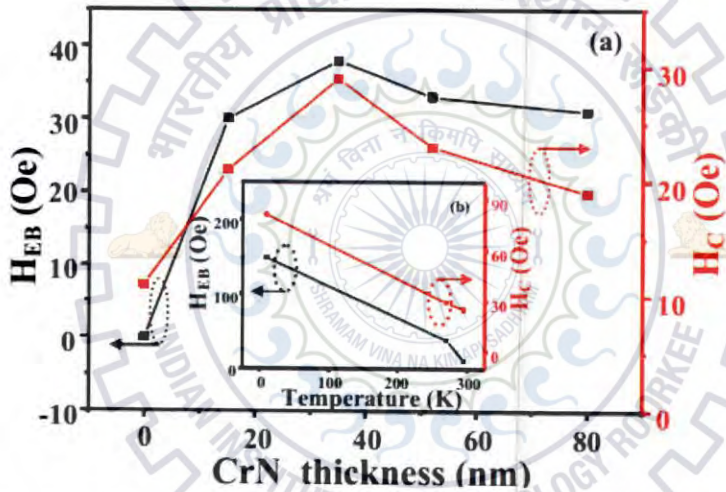
Figure 5.3. (a) Variation of exchange bias field (H_{EB}) and coercivity (H_C) exchange bias (H_{EB}) as a function of CrN thickness (b) Variation of exchange bias (H_{EB}) and coercivity (H_c) as a function of temperature for $Ni_{50}Mn_{36.8}Sb_{13.2}$/CrN heterostructure (S3).

Sample	Temperature (K)					
	10		270		295	
	H_{EB}(Oe)	H_c(Oe)	H_{EB}(Oe)	H_c(Oe)	H_{EB}(Oe)	H_c(Oe)
S1	51	8	0	11	0	90
S2	79	65	30	21	4	17
S3	148	81	38	29	10	25
S4	131	88	33	23	11	18
S5	127	74	31	19	9	12

Table 5.2. Calculated exchange bias (H_{EB}) and coercivity (H_C) of pure NiMnSb film (S1) and $Ni_{50}Mn_{36.8}Sb_{13.2}$/CrN heterostructures (S2, S3, S4, S5) at 10 K, 270 K and 295 K.

Inset of **figure 5.3 (b)** shows the variation of H_{EB} and H_C with temperature. Especially, the H_{EB} decreases from 148 Oe at 10 K to 10 Oe at 295 K. At 295 K, CrN layer is paramagnetic, and H_C is mainly due to the demagnetization of ferromagnetic Ni-Mn-Sb layer which results in small exchange bias. Moreover, after the field cooling, the system below the T_N (= 270 K) of AFM CrN phase, some antiferromagnetic spins may be reoriented to the direction of applied field, which couples with the ferromagnetic spins on the interface. Furthermore, at 10 K, many spins may be frozen in directions with minimum energy; the whole system is frozen in a metastable state. The interaction between FM (Ni-Mn-Sb) and AFM (CrN) phases would become quite strong. It is clear from **figures 5.2 (d)–(f)** that the hysteresis loops are saturated at higher applied magnetic fields (up to 4 T) for these temperatures. One can reach the fully saturated state when the two layers of FM/AFM are aligned ferromagnetically at high magnetic fields. The reduction of H_{EB} with increasing temperature is due to the fact that ferromagnetic interaction start to dominate and the antiferromagnetic anisotropy reduces with increasing temperature. This results in weakening of ferromagnetic-antiferromagnetic interface coupling which is responsible for decrease in exchange bias. The coercive field is of great importance as it defines the operating magnetic field range of active devices. The value of H_C was observed to decrease with increasing temperature which is due to the large antiferromagnetic anisotropy of Ni-Mn-Sb/CrN heterostructure system at higher temperature; as a result, the FM (Ni-Mn-Sb) decouples because it cannot drag more AFM (CrN) spins, consequently H_C is decreased. Also, excess thermal energy reduces the exchange coupling between ferromagnetic and antiferromagnetic layers and leads to low values of coercivity [17-18].

The values of exchange bias field (H_{EB}) and coercivity (H_C) of (NiMnSb/CrN) exchange bias
system are shown in **table 5.2**.

5.3.3 Mechanical properties

The hardness (H), elastic modulus (E), elastic recovery ratio (δ), plasticity index (H/E), and
resistance to plastic deformation (H^3/E^2) of thin films were calculated using indentation load-depth
curves for each sample using Oliver and Pharr method [19]. The indentation induced super elastic
effect can be characterized by the elastic recovery ratio which is obtained from the load-depth
curves. It can be seen that hardness (H) and other mechanical properties of Ni-Mn-Sb thin film are
improved with incorporation of CrN bottom layer. One reason is that the relatively hard CrN layer,
of which the hardness was 21 GPa, weakened the effect of the silicon substrate as the thickness of
the CrN layer increased. The other reason could be the strain induced in the film as a consequence
of lattice mismatch between the substrate and CrN layer, and the mismatch between the CrN layer
and Ni-Mn-Sb layer, respectively. The strain was observed to be positive for film S1 depicting
tensile nature. However, the strain was found to be compressive for films S2, S3, S4, and S5. It is
clear from **table 5.3** that there is a rapid decrease in the strain up to CrN thickness 15 nm and after
it, there is a slight decrease in strain. In the present case, the grain growth of S2-S5 film is believed
to be controlled by lattice misfit and strain imposed by the bottom CrN film which varies with CrN
thickness. In general, a film under compressive strain results in lattice contraction which resists the
penetration of indenter then by decreasing the indentation depth and inhibiting the crack
propagation [20]. The higher value of H/E (0.07) for film S5 is indicative of its better wear
resistance as compared to film S1, which may be due to its higher hardness. The H^3/E^2 parameter
determines resistance of film to plastic deformation and follows the similar trend as shown in **table
5.3**.

Sample	CrN Thickness (nm)	Strain, ε	Total depth, h_{max} (nm)	Residual depth, h_r (nm)	Elastic recovery ratio,δ	Hardness H (GPa)	Elastic modulus E (GPa)	H/E	H^3/E^2
S1	0	0.005	70.93	25.92	0.634	3.8±0.25	81.52±1.05	0.047	0.0085
S2	15	0.0016	65.08	23.61	0.637	5.2±1.8	94.5±0.6	0.054	0.015
S3	35	-0.002	52.19	16.86	0.67	7±0.5	120±1.25	0.058	0.023
S4	52	-0.003	46.57	12.28	0.73	8.7±1.2	142±1.82	0.062	0.033
S5	80	-0.006	38.38	8.13	0.78	12.7±0.38	179.83±1.24	0.07	0.063

Table 5.3. Various mechanical properties of $Ni_{50}Mn_{36.8}Sb_{13.2}$ film (S1) and $Ni_{50}Mn_{36.8}Sb_{13.2}$/CrN heterostructures (S2, S3, S4, S5) of different thicknesses.

5.4 Conclusion

In conclusion, we have investigated the exchange bias in various $Ni_{50}Mn_{36.8}Sb_{13.2}/CrN$ heterostructures with different CrN thicknesses (15 nm–80 nm), grown on Si (100) substrate using magnetron sputtering. The shift in hysteresis loop up to 51 Oe from the origin was observed at 10 K for Ni-Mn-Sb film without CrN layer. On the other hand, a significant shifting of hysteresis loop was observed with antiferromagnetic (AFM) CrN layer in $Ni_{50}Mn_{36.8}Sb_{13.2}/CrN$ heterostructure. The exchange coupled 140 nm $Ni_{50}Mn_{36.8}Sb_{13.2}/35$ nm CrN heterostructure exhibited a relatively large exchange coupling field of 148 Oe at 10 K compared to other films, which may be related to uncompensated and pinned antiferromagnetic spins at ferromagnetic-antiferromagnetic interface and different antiferromagnetic domain structures for different thicknesses of CrN layer. Further nanoindentation measurements revealed the higher values of hardness and elastic modulus of about 12.7 ±0.38 GPa and 179.83 ±1.24 GPa in $Ni_{50}Mn_{36.8}Sb_{13.2}/CrN$ heterostructures making them promising candidate for various multifunctional MEMS devices.

5.5 References

[1]   Meikeljohn W. H., Bean C. P., "New Magnetic Anisotropy," *Phys. Rev.*, **102**, 1413 (1956).

[2]   Berkowitz A. E., Takano K., "Exchange anisotropy-a review," *J. Magn. Magn. Mater.*, **200**, 552 (1999).

[3]   Parker J. S., Wang L., Steiner K. A., Crowell P. A., Leighton C., "Exchange Bias as a Probe of the Incommensurate Spin-Density Wave in Epitaxial Fe/Cr(001)," *Phys. Rev. Lett.*, **97**, 227206 (2006).

[4]   Engebretson D. M., Macedo W. A. A., Schuller I. K., Crowell P. A., Leighton C., "Time domain dynamics of the asymmetric magnetization reversal in exchange biased bilayers," *Phys. Rev. B*, **71**, 184412 (2005).

[5]   Roy S. B., Chattopadhyay M. K., Chaddah P., Nigam A. K., "Sharp magnetization step across the ferromagnetic-to-antiferromagnetic transition in doped $CeFe_2$ alloys," *Phys. Rev. B*, **71**, 174413 (2005).

[6]   Nogués J., Schuller I. K., "Exchange bias," *J. Magn. Magn. Mater.*, **192**, 203 (1999).

[7]   Nayak A. K., Suresh K. G., Nigam A. K., "Giant inverse magnetocaloric effect near room temperature in Co substituted NiMnSb Heusler alloys," *J. Phys. D: Appl. Phys.*, **42**, 035009 (2010).

[8]   Arenholz E., Liu K., Li Z., Schuller I. K., Liu K., "Magnetization reversal of uncompensated Fe moments in exchange biased Ni/FeF_2 bilayers," *Appl. Phys. Lett.*, **88**, 072503 (2011).

[9]   Khan M., Dubenko I., Stadler S., Ali N., "Exchange bias behavior in Ni-Mn-Sb Heusler alloys," *Appl. Phys. Lett.*, **91**, 072510 (2007).

[10]   Vishnoi R., Kaur D., "Exchange bias behaviour in magnetron sputtered $Ni_{49.8}Mn_{36.1}Sn_{13.9}$ ferromagnetic shape memory alloy thin film," *J. Alloys Compd.*, **509**, 2833 (2011).

[11]   Vishnoi R., Kaur D., "Structural and magnetic properties of magnetron sputtered Ni–Mn–Sn ferromagnetic shape memory alloy thin films," *J. Appl. Phys.*, **107**, 103907 (2010).

[12]   Gong W. J., Liu W., Li D., Guo S., Liu X. H., Feng J. N., Li B., Zhao X. G., Zhang Z. D., "Exchange bias effect in $NiO/NiFe_2O_4$ nanocomposites," *J. Appl. Phys.*, **109**, 07D711 (2011).

[13]   Nowak U., Usadel K. D., Beschoten B., Gu G., Keller J., Milte P., "Domain state model for exchange bias. I. Theory," *Phys. Rev. B*, **66**, 014430 (2002).
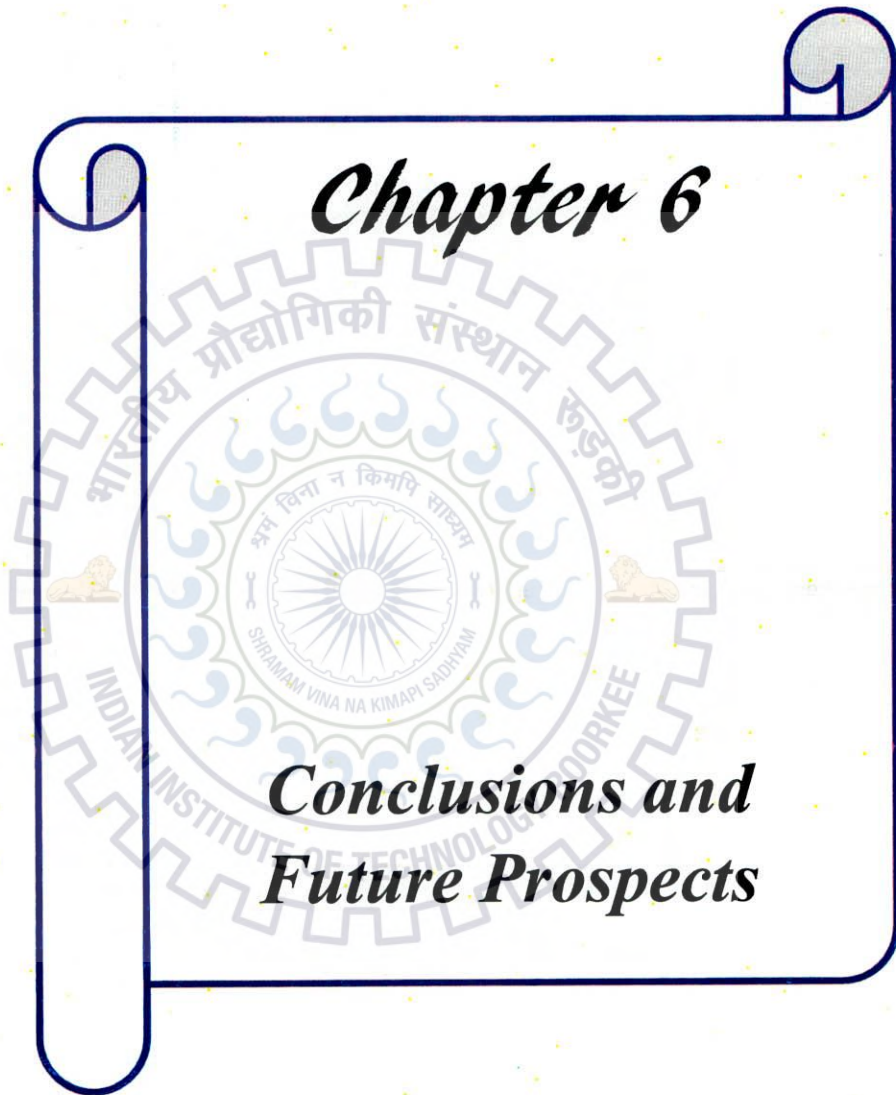
[14]   Oliver W. C., Pharr G. M., " An improved technique for determining hardness and ealstic modulus using load and displacement sensing indentation experiments", *J. Mater. Res.,* 7, 1564 (1992).

[15]   Kaur N., Kaur D., "Grain refinement of NiTi shape memory alloy thin films by W addition," *Mater. Lett.*, **91**, 202 (2013).

Chapter 6

Conclusions and Future Prospects

CHAPTER 6

CONCLUSIONS AND FUTURE PROSPECTS

6.1 Conclusions

6.1.1 Growth and characterization of magnetron sputtered nanostructured Ni-Mn-In ferromagnetic shape memory alloy thin films

6.1.2 Martensitic phase transformations and magnetocaloric effect in Al co-sputtered Ni-Mn-Sb alloy thin films

6.1.3 Ni-Mn-In-Cr ferromagnetic shape memory alloy thin films

6.1.4 Exchange bias effect and mechanical properties in Ni-Mn-Sb/CrN heterostructures synthesized by magnetron sputtering

6.2 Future Prospects
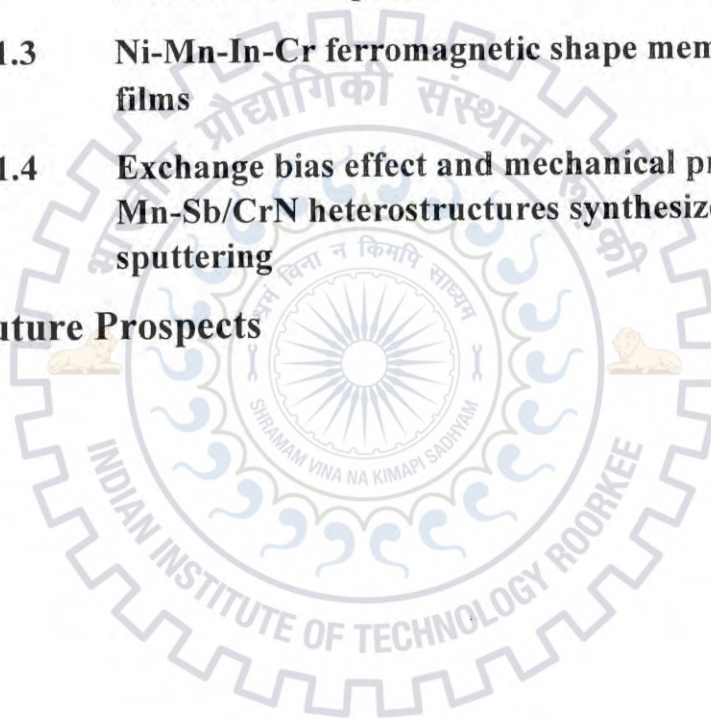
6.1 Conclusions

The main aim of the present study was to fabricate the good quality of Ni-Mn-In and Ni-Mn-Sb ferromagnetic shape memory alloy thin films and also Ni-Mn-Sb/CrN heterostructures on silicon substrate using DC magnetron sputtering technique in order to

(i)   Investigate the structural, phase transformation, magnetic, mechanical and magnetocaloric properties of FSMA thin films.

(ii)   Study the growth and characterization of Ni-Mn-Sb-Al and Ni-Mn-In-Cr thin films.

(iii)   Study the exchange bias behavior in Ni-Mn-Sb/CrN heterostructures. A brief summary and conclusions based on the results obtained are given below:

6.1.1 Growth and characterization of magnetron sputtered nanostructured Ni-Mn-In ferromagnetic shape memory alloy thin films

In the present study, the influence of film thickness on structural, magnetic, electrical and mechanical properties of nanostructured Ni-Mn-In thin films was studied. The film thickness was varied from ~ 90 nm to 655 nm. XRD analyses revealed that the films exhibit austenitic phase with $L2_1$ structure at room temperature. The grain size and crystallization extent increased with corresponding increase in film thickness. The temperature dependent magnetization and electrical measurements demonstrated the absence of phase transformation in the films with less than 90nm, which could be due to small grain size of these films. For thickness greater than 153 nm, the films show first order martensitic phase transition with thermal hysteresis width, which increases with further increase in film thickness. The field dependent magnetization curves also show the increase in saturation magnetization (S_M). The value of refrigerant capacity (RC) which is an important figure of merit has been found to be 155.04 mJ/cm^3. Maximum exchange bias of 0.0096 T and large magnetic entropy change ΔS_M=15.2 mJ/cm^3 K (field 2 T) at martensitic transformation was obtained for film thickness of 655 nm which makes them useful for microelectromechanical system (MEMS) applications. Further, nanoindentation studies revealed the higher values of hardness of 7.2 GPa and elastic modulus of 190 GPa for the film thickness of 153 nm. These findings indicate that the Ni-Mn-In thin films are useful for various multifunctional properties.

6.1.2 Martensitic phase transformation and magnetocaloric effect in Al co-sputtered Ni-Mn-Sb alloy thin films

Effect of Aluminium (Al) content on the martensitic phase transformation and magnetocaloric properties in Ni-Mn-Sb ferromagnetic shape memory alloy (FSMA) thin films was investigated. Increase in Al content leads to a gradual increase in the martensitic transition temperature was observed in these samples. A maximum magnetic entropy change of $\Delta S_M = 23$ mJ/cm^3 K at 300 K for a magnetic field change of 2 T was observed in the Ni$_{49.8}$Mn$_{32.97}$Sb$_{12.8}$Al$_{4.43}$ alloy thin film. On the other hand, the refrigerant capacity (RC) reached to 64.4 mJ/cm^3 at 2 T for this film. The increase in MCE is attributed to the large magneto-structural coupling, which causes a large magnetization difference and large value of $\partial M/\partial T$ upon Al concentration. Such a large MCE developed in the Ni–Mn–Sb–Al alloy thin films make them potential candidate for the micro length scale magnetic refrigeration.

6.1.3 Ni-Mn-In-Cr ferromagnetic shape memory alloy thin films

The present study explored the influence of Cr addition on the structural, magnetic and mechanical and magnetocaloric properties of magnetron sputtered Ni-Mn-In ferromagnetic shape memory alloy thin films. X-ray diffraction studies revealed that Ni-Mn-In-Cr thin films possessed purely austenitic cubic L2$_1$ structure at lower content of Cr, whereas at higher Cr content, the films exhibited martensitic structure at room temperature. The temperature-dependent magnetization (M-T) and resistance (R-T) results confirmed the monotonous increase in martensitic transformation temperatures (T_M) with the addition of Cr content (0 - 4.5 at %). Further, the addition of Cr content significantly enhanced the hardness (28.2±2.4 GPa) and resistance to plastic deformation H^3/E^2 (0.261) in Ni$_{50.4}$Mn$_{34.96}$In$_{13.56}$Cr$_{1.08}$ film as compared with pure Ni-Mn-In film, which could be due to reduction in grain size, and has been explained in terms of the grain boundary strengthening mechanism. From the study of isothermal magnetization (M-H) curves, the magnetocaloric effect (MCE) around the martensitic transformation has been investigated. The magnetic entropy change ΔS_M of 7.0 mJ/cm^3 K was observed in Ni$_{51.1}$Mn$_{34.9}$In$_{9.5}$Cr$_{4.5}$ film at 302 K in an applied field of 2 T. Finally, the refrigerant capacity (RC) was also calculated for all the films in an applied field of 2 T.

6.1.4 Exchange bias effect in Ni-Mn-Sb/CrN heterostructures synthesized by magnetron sputtering

The present study reveals the deposition of $Ni_{50}Mn_{36.8}Sb_{13.2}$/CrN heterostructures on Si (100) substrate to improve the exchange bias and mechanical properties of Ni-Mn-Sb ferromagnetic shape memory alloy thin films. The antiferromagnetic CrN thickness was varied from 15 nm to 80 nm. The shift in hysteresis loop up to 51 Oe from the origin was observed at 10 K when pure Ni-Mn-Sb film was cooled under a magnetic field of 0.1 T. The observed exchange bias has been attributed to the coexistence of antiferromagnetic (AFM) and ferromagnetic (FM) exchange interactions in the martensitic phase of the film. On the other hand, a significant shifting of hysteresis loop was observed with AFM CrN layer in $Ni_{50}Mn_{36.8}Sb_{13.2}$/CrN heterostructure. The exchange coupled 140 nm $Ni_{50}Mn_{36.8}Sb_{13.2}$/35nmCrN heterostructure exhibited a relatively large exchange coupling field of 138 Oe at 10 K compared to other films, which could be due to uncompensated and pinned AFM spins at FM-AFM interface and different AFM domain structure for different thicknesses of CrN layer. Further nanoindentation measurements revealed the higher values of hardness and elastic modulus of about 12.7 ± 1.25 GPa and 179 ± 0.12 GPa in $Ni_{50}Mn_{36.8}Sb_{13.2}$/CrN heterostructures making them promising candidate for various multifunctional MEMS devices.

6.2 Future prospects

There are certain unsolved issues and also new ideas related to these nanocrystalline films, on which one can extend the study in future with the following points:

(i) Growth of epitaxial films of Ni-Mn-In and Ni-Mn-Sb FSMAs by appropriate selection of substrate and optimization of deposition parameters can be investigated.

(ii) Further the devices like magnetic sensors and micro actuators can be fabricated using epitaxial FSMA thin films.

(iii) Artificial multiferroics can be fabricated using combination of FSMAs and $BiFeO_3$ or $BaTiO_3$ and their applications can be further enhanced.

(iv) The mechanical properties of FSMA films can be improved using hard transition metal nitride coatings to enable them for MEMS applications.